Helsinki University of Technology Radio Laboratory Publications
Teknillisen korkeakoulun Radiolaboratorion julkaisuja
Espoo, June, 2002 REPORT S 254

# RECTANGULAR DIELECTRIC WAVEGUIDE AND ITS OPTIMAL TRANSITION TO A METAL WAVEGUIDE

Thesis for the degree of Doctor of Science in Technology

**Sergey Dudorov**

TEKNILLINEN KORKEAKOULU
TEKNISKA HÖGSKOLAN
HELSINKI UNIVERSITY OF TECHNOLOGY
TECHNISCHE UNIVERSITÄT HELSINKI
UNIVERSITE DE TECHNOLOGIE D'HELSINKI

Helsinki University of Technology Radio Laboratory Publications

Helsinki University of Technology Radio Laboratory Publications
Teknillisen korkeakoulun Radiolaboratorion julkaisuja
Espoo, June, 2002 REPORT S 254

# RECTANGULAR DIELECTRIC WAVEGUIDE AND ITS OPTIMAL TRANSITION TO A METAL WAVEGUIDE

**Sergey Dudorov**

Dissertation for the degree of Doctor of Science in Technology to be presented with due permission for public examination and debate in Auditorium S4 at Helsinki University of Technology (Espoo, Finland) on the 3rd of June 2002 at 12 o'clock noon.

Helsinki University of Technology
Department of Electrical and Communications Engineering
Radio Laboratory

Teknillinen korkeakoulu
Sähkö- ja tietoliikennetekniikan osasto
Radiolaboratorio

Distribution:
Helsinki University of Technology
Radio Laboratory
P.O.Box 3000
FIN-02015 HUT
Tel.  +358-9-451 2252
Fax. +358-9-451 2152

ISBN 951-22- 5972-9
ISSN 1456-3835

Otamedia Oy
Espoo 2002

# Preface

This work was carried out in MilliLab, Helsinki University of Technology, Radio Laboratory.

I would like to say thanks to my supervisor, Professor Antti Räisänen for his careful examination and comments of texts. I did not expect so many mistakes. Additional thanks are due to checking even Russian references.

I am especially thankful to Dr. Dmitri Lioubtchenko for his help. Without him this work would not have been done.

Also thanks to Prof. Sergey Tretyakov for his help and especially for introducing me to the averaging method. I very much like the idea to take care of only tangential field components and only at the interfaces.

Finally, I would also like to say thanks to the whole staff of the Radio Laboratory for providing a pleasant working atmosphere.

Espoo, April 2002

Sergey Dudorov

# Abstract

The purpose of this work was to study the rectangular dielectric waveguide and its transitions to metal waveguide at millimeter wavelengths. The thesis reviews different dielectric waveguiding structures, their analysis methods and their transitions to the metal waveguide. In this thesis work the analysis methods and transitions are further developed. The main results of this work are:

1. It was shown that, after modifications, the Marcatili and Goell methods can be applied for calculating propagation constants of rectangular dielectric waveguide made of uniaxial anisotropic material with the optical axis oriented along the dielectric waveguide.
2. Several tapering shapes were studied. It was shown that symmetrical **E**-tapering gives lower insertion losses and smaller reflections compared with the **H**-tapering.
3. Different cross-sections and geometry of tapering were studied using Agilent HFSS program. The most appropriate dimensions were found.
4. In the case of unsymmetrical tapering it was shown that better results are achieved when the axes of metal and dielectric waveguides do not coincide but differ by half of the tapering angle.
5. Low insertion loss and small reflections were obtained with sapphire waveguide section. For a 100 mm sapphire waveguide section lower losses were obtained than for a 100 mm standard metal waveguide section.
6. Characteristics of a dielectric rod antenna were measured.

# Contents

## List of symbols

| | |
|---|---|
| $a$, $b$ | Dimensions of a dielectric waveguide |
| $C$ | See page 38 |
| $d$ | Thickness |
| $E_{pq}^{x}$, $E_{pq}^{y}$ | Propagating modes in a rectangular dielectric waveguide |
| $E$ | Electric field |
| $E^{LA}$, and other | Submatrixes (see p. 39). |
| $f$ | "Averaging" function |
| $G$ | Green's function |
| $H$ | Magnetic field |
| $h$ | Transversal propagation constants inside of the dielectric waveguide in Goell's method |
| $h_{\mathrm{E}}$, $h_{\mathrm{M}}$ | "Electric" and "magnetic" propagation constants in Goell's method |
| $J_E$, $J_M$ | "Electric" and "magnetic" Bessel function of first kind |
| $\boldsymbol{J}$ with indices | See p. 38 |
| $K$ | Modified Bessel function of second kind |
| $\boldsymbol{K}$ | See p. 38 |
| $k_{\mathrm{x}}$, $k_{\mathrm{y}}$, $k_{\mathrm{z}}$ | Propagation constants in directions $x$, $y$, $z$ inside the dielectric |
| $k_0$ | Wave number in vacuum |
| $l$ | Length of tapering section |
| $n$ | Refractive index |
| $p$ | Transversal propagation constants outside of the dielectric waveguide in Goell's method |
| $P$, $P_{\mathrm{a}}$ | Total propagating power, power absorbed per unit length |
| $r$ | Distance |
| $R$ | See p. 38 |
| $S$ | See p. 38 |
| $S_{21}$, $S_{11}$ | Transmission and reflection coefficients |
| $T$ | See p. 38 |
| $\tan\delta$ | Loss tangent |
| $w$ | Width |
| $x$, $y$ | Rectangular coordinates |
| $Z_0$ | Impedance of vacuum |
| $\alpha$ | Propagation loss per unit length in a dielectric waveguide |
| $\alpha_0$ | Propagation loss per unit length in an infinite media filled with the same dielectric |
| $\beta$ | Propagation constant |
| $\beta_x$, $\beta_y$ | Transversal propagation constants |

| | |
|---|---|
| $\varepsilon_{eff}$ | Effective dielectric constant |
| $\varepsilon_r$ | Relative permittivity |
| $\varepsilon_0$ | Permittivity of vacuum |
| $\varepsilon_{\parallel}$ | "Parallel" permittivity |
| $\varepsilon_{\perp}$ | "Perpendicular" permittivity |
| $\mu$ | Permeability |
| $\eta$ | Propagation constants in directions $y$ outside the dielectric |
| $\theta$ | Angle in polar coordinates in Goell's method |
| $\theta_c$ | Critical angle (see p. 36) |
| $\xi$ | Propagation constants in directions $x$ outside the dielectric |
| $\Pi$ | Some function |
| $\varphi$ | A phase angle in Goell's method |
| $\phi$ | Some function |
| $\Phi$ | Some function |

## List of abbreviations

| | |
|---|---|
| DRW | Dielectric Rod Waveguide |
| HFSS | High Frequency Structure Simulator |
| MMIC | Monolithic Microwave Integrated Circuits |

## Errata

In [P1] the second author's name should read Parkhomenko.

## List of publications

[P1] V.V. Meriakri, M.P. Parkhomenko, S.N. Dudorov, "Millimeter wave dielectric strip waveguides made of ferrites, and devices based on these waveguides", *Proceedings of the XXVIII Moscow International Conference on Antenna Theory and Technology*, 22-24 September, 1998, Moscow, pp. 493-495.

[P2] D. Lioubtchenko, S. Dudorov, J. Mallat, J. Tuovinen, A.V. Räisänen, "Low Loss Sapphire Waveguides for 75-110 GHz Frequency Range", *IEEE Microwave and Wireless Components Letters*, vol. 11, no. 6, 2001, pp. 252-254.

[P3] S. N. Dudorov, D. V. Lioubtchenko, A.V. Räisänen, "Modification of Marcatili's method for the calculation of anisotropic rectangular dielectric waveguides", *IEEE Trans. on Microwave Theory and Techniques*, vol. 50, no. 6, 2002.

[P4] S.N. Dudorov, D.V. Lioubtchenko, J.A. Mallat, A.V. Räisänen, "Modified Goell method for the calculation of uniaxial anisotropic rectangular dielectric waveguides", *Microwave and Optical Technology Letters*, vol. 32, no. 5, 2002, pp. 373-376.

[P5] D.V.Lioubchenko, S.N. Dudorov, A.V. Räisänen. "Development of rectangular open dielectric waveguide sections for the frequency range of 75-110 GHz", *31st European Microwave Conference*, London 2001, pp. 201-204.

[P6] S. Dudorov, D. Lioubtchenko, J. Mallat, J. Tuovinen, A.V. Räisänen, "Low loss dielectric waveguides at 75-110 GHz frequency range", *Abstracts of the URSI XXV National Convention on Radio Science*, Helsinki, Finland, September 2000, pp. 40-41.

[P7] S. Dudorov, D. Lioubtchenko, J. Mallat, A.V. Räisänen, "Sapphire dielectric waveguide antenna", *URSI XXVI National Convention on Radio Science*, Tampere, Finland, October 2001, pp. 127-128.

Publications [P2]-[P7] are supervised by Antti V. Räisänen. D. Lioubtchenko assisted in measurements and helped to choose the material of the dielectric waveguides and to obtain samples. Author was responsible for all the measurements, simulations and theoretical calculations. [P1] was supervised by V.V. Meriakri, author was taking part in measurements. In publications [P2] and [P6] J. Tuovinen was a co-supervisor. In publications [P2], [P4], [P6] and [P7] J. Mallat was a co-supervisor.

# 1. Introduction

## 1.1. General

Dielectric materials are increasingly used at frequencies above 100 GHz. There are dielectric waveguides, directional couplers, phase shifters, multistate reflectometers, etc., which are based on them. Dielectric rod waveguides (DRW) have lower losses, wider tolerances and lower cost in comparison with the standard metal waveguides. DRW being an open transmission line allows affecting its characteristics with light, magnetic field and other means. Therefore controllable devices like attenuators, multiplexers and phase shifters, etc. can be designed based on DRWs. These devices have been intensively investigated, see e.g. [1, 2, P1]. Particularly in [3] there is a review about different types of DRWs and other transmission lines. In comparison with the standard metal waveguides DRWs have much broader operating frequency bandwidths in which only two fundamental modes propagate. Moreover, an isolated DRW has no cut-off frequency for two fundamental modes differing by the x and y polarization. The frequency band allowing only these two fundamental modes could be even wider if a graded index guide similar to the optical fiber was used in the millimeter wave frequency band [3]. It has been shown that by varying the thickness or height of DRW in the transversal direction one can achieve the desired effective refraction index profile and obtain single mode operation even if the cross dimensions of such a DRW are several wavelengths [3]. Also, at frequencies beyond 300 GHz the use of standard metal waveguides becomes difficult, i.e. only multimode regime is applicable, because the dimensions and losses of a single mode waveguide become unacceptable at these frequencies. So the use of DRWs becomes important for mm- and submm-wave devices.

## 1.2. Scope and contents of this thesis

The purpose of this work is investigation of rectangular dielectric waveguides made of materials of high permittivity such as semi-insulating semiconductors and sapphire, and also investigation of transitions from a dielectric waveguide to a metal one and to design a simple and effective transition structure.

The dielectric waveguide section is supposed to be used in a mm-wave power standard as an isolation section. Therefore the desired results are: construction of a simple dielectric waveguide section with low insertion loss and small reflections, and capability to design and analyze it accurately.

In the second chapter of this work a review of dielectric waveguiding structures and transitions to the metal waveguide is presented. In the third chapter, a review of existing numerical and approximation methods for dielectric waveguiding structures is presented. In the fourth chapter two simple and effective methods for calculating anisotropic dielectric waveguides are developed and verified experimentally. They are based on the methods by Marcatili and Goell developed originally for isotropic dielectric waveguides. Some attention is paid to the influence of anisotropy to the dispersion characteristics.

In chapters 5 and 6 simulation and experimental results, respectively, are described. In this work rectangular dielectric waveguides made of materials of high relative permittivity (above 10) are investigated. The main attention is paid to the transition from a metal waveguide to a dielectric one. Experimental measurements have been carried out with HP 8510$^{TM}$ network analyzer. Agilent High frequency simulator HFSS$^{TM}$ simulations with finite element method have also been carried out in order to find the optimal dimensions of the dielectric waveguide and its matching section. Displacements of the dielectric waveguide relative to the metal ones are also studied in simulations and experiments.

# 2. Dielectric waveguides (literature review)

## 2.1. Dielectric waveguides

The main types of dielectric waveguides are shown in Fig. 2.1. A review of different transmission lines and devices based on them can be found, for example, in [2]. The use of dielectric waveguide gives a possibility to decrease the cost of devices for the millimeter wave region. Based on dielectric waveguide, different devices can be designed, such as attenuators, phase shifters and antennas with a tunable radiation pattern. Mirror dielectric waveguide (Fig.2.1b) differs from the basic open dielectric waveguide only by having a ground plane. In addition to its low cost, simplicity in construction and low attenuation, it has a relatively wide operating bandwidth of the single mode operation. Metallization makes it suitable for MMIC (microwave monolithic integrated circuit) devices, like receiving modules for the mm-wave region. In [4] a boron-nitride waveguide with losses of the order of $10^{-3}$ per wavelength at frequency 94 GHz is reported.

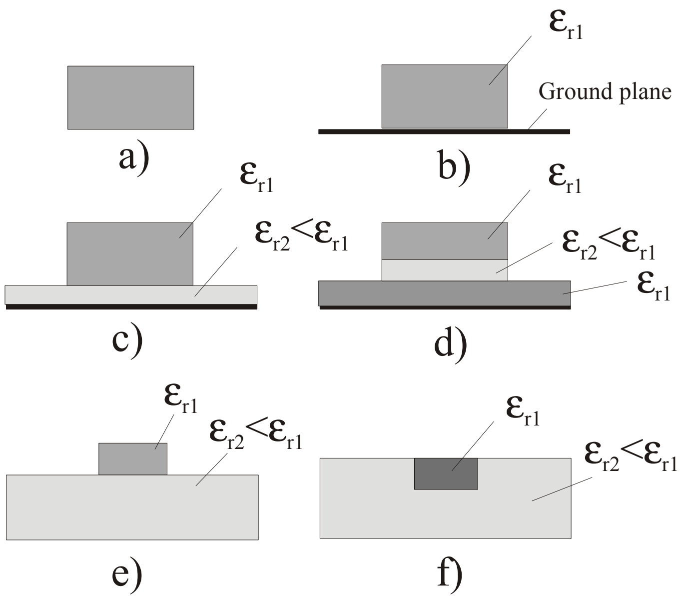

**Figure 2.1.** Main types of dielectric waveguide

**a**) dielectric waveguide, b) mirror dielectric waveguide, c) isolated mirror dielectric waveguide, d) layered ribbon dielectric waveguide, e),f) other types.

Isolated dielectric mirror waveguide differs from the previous waveguide by an additional dielectric layer with a permittivity smaller than the permittivity of the strip (Fig.2.1c). It is shown that if the surrounding medium has a smaller dielectric permittivity than that of the dielectric strip, power will mainly propagate within the core. Therefore, if a layer is added with a smaller permittivity between the strip and the ground plate, one can decrease the metal losses by more than 50% [4]. This becomes rather important at frequencies above 100 GHz.

In general, there is an opinion that at millimeter and submillimeter wavelengths the less of metal present the better, as metal introduces extra losses compared with the dielectric ones [5].

As the dielectric material may be any semi-insulating semiconductor, different semiconductor devices can be designed directly in the waveguide by means of ion implantation and multilayer epitaxy.

As the semiconductor and ferrite materials have rather high dielectric permittivity, the sizes of the waveguides can be made very small without loss of waveguiding properties. A phase shifter made of ferrite with $\varepsilon_r$=13.8 for the frequency range 53-78 GHz has transversal dimensions 0.8 mm × 1.4 mm which are less than half of the wavelength [6]. At higher frequencies these dimensions will be certainly smaller, as they scale in wavelength.

Dielectric waveguides on dielectric substrates are the basis of so-called integral optics [7,8]. Mainly, the integral optics is used in optical integrated circuits, where the dimensions of the waveguides allow applying thin-film technology. However, there are also mm-wave and submm-wave applications.

The field distribution in a dielectric waveguide is shown schematically in Fig. 2.2. In such a waveguide different modes $E^x_{pq}$ and $E^y_{pq}$ can propagate. The indices of modes show how many extremes the field distribution has along each axis. The upper index $^y$ shows that the largest component of the electrical field is in the y-direction. Thus, in Fig. 2.2 the field distribution of mode $E^y_{12}$ is shown. In Fig. 2.3 dispersion characteristics and attenuation factor vs. the wave number in vacuum are shown.

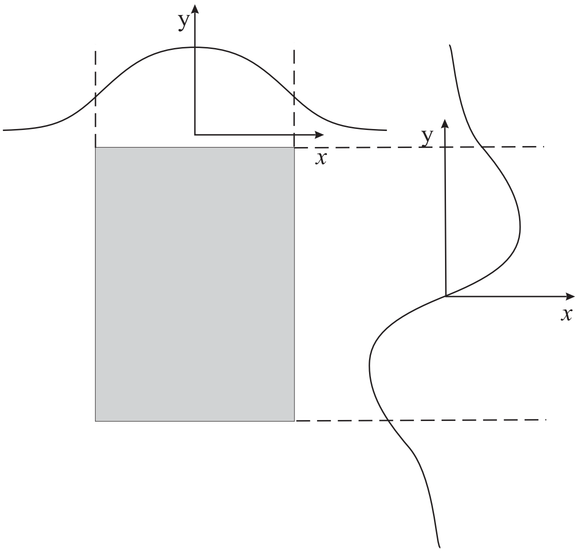

**Figure 2.2.** Field distribution $H_x$ of the dielectric waveguide in case of propagating mode $E^y_{12}$.

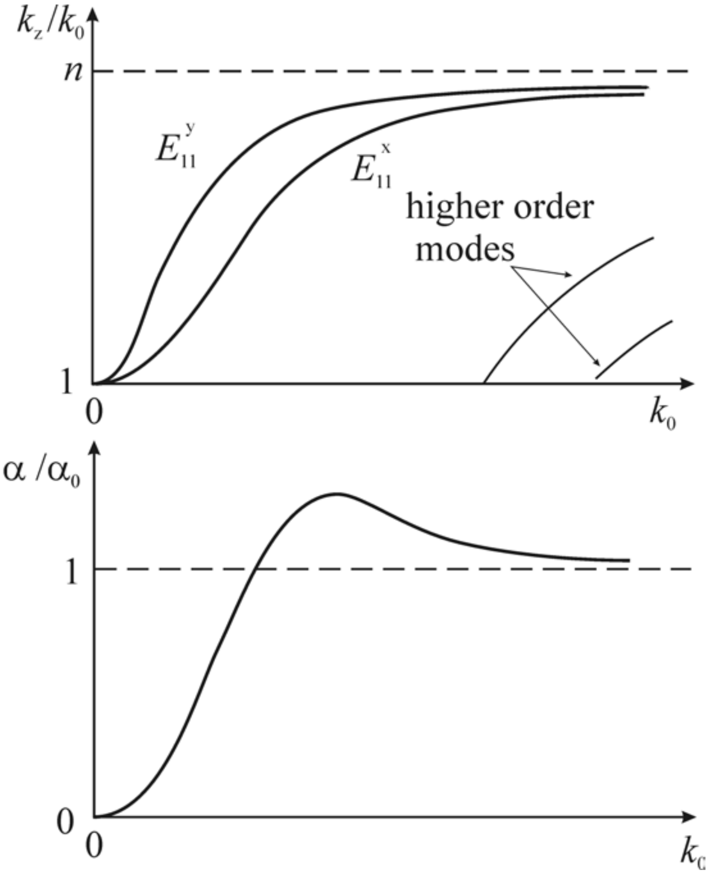

**Figure 2.3.** Schematic dispersion characteristic and dependence of the loss factor $\frac{\alpha}{\alpha_0}$ vs. frequency in a dielectric waveguide. $k_0$ is the wave number in vacuum, $\alpha_0 = \frac{1}{2} kn \tan\delta$ is the attenuation constant of infinite medium filled with the same dielectric, *n* is the refractive index of the DRW.

It was shown by different authors that the lowest modes $E_{11}^{x}$ and $E_{11}^{y}$ do not have any cut-off frequency in contrast to the higher order modes [9,10]. Therefore, in principle, lower losses can be obtained by simply reducing the size. The smaller is the size, the smaller fraction of power propagates within the dielectric core. However, in that case the electromagnetic wave will experience radiation due to even very small discontinuities.

If we look again at Fig. 2.3 we can see that at a very high frequency the properties of such waveguides approach the properties of the infinite medium filled with the same dielectric. The second observation is that after some frequency the loss parameter $\frac{\alpha}{\alpha_0}$ becomes larger than unity and then asymptotically decreases to one [11].

## 2.2. Transitions from standard metal waveguide to dielectric rod waveguide

Excitation of DRW is somewhat problematic, because in DRW the propagating field is partially outside the rod as shown in Fig. 2.2. Previously, DRWs were made of such materials as polyethylene and teflon, which have a low dielectric constant. Therefore the dimensions of such waveguides coincided with the cross section of the standard metal waveguide. In order to decrease losses in the transitions, the authors usually designed a tapering section followed by a small horn, see e.g. [12] (Fig. 2.4), so that a contact between metal and DRW was not avoided, but was rather desired due to mechanical reasons.

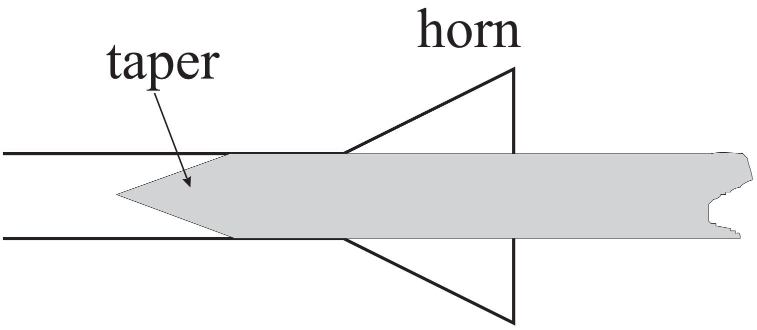

**Figure 2.4.** Transition from metal to dielectric waveguide with the same cross section.

In the case of DRW made of, for example, a semiconductor or a dielectric with a high permittivity, the dimensions for a single-mode operation become smaller. Therefore, different constructions for DRW mode launchers are used [5, 13-14], see Figs. 2.5 and 2.6.

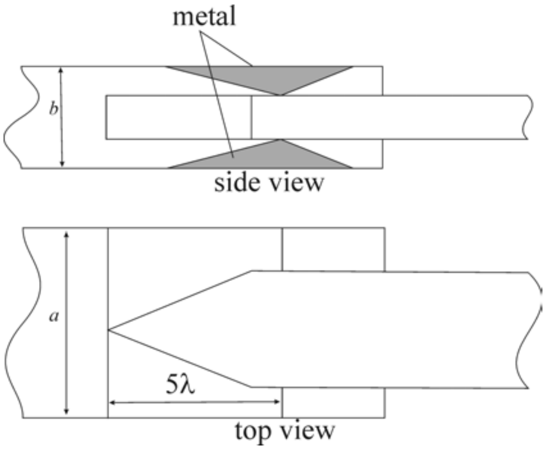

**Figure 2.5.** Transition from metal to silicon waveguide [12].

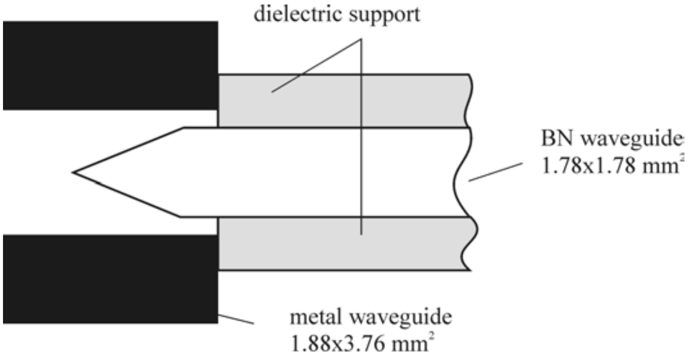

**Figure 2.6.** Transition from metal to boron nitride waveguide [5].

All such constructions consist of the following parts: a transition from the standard metal waveguide to the waveguide filled with dielectric, followed by a transition to the dielectric waveguide itself. In the structure presented in Fig. 2.6 [1,5,14] there is no horn neither a contact between the metal waveguide and DRW.

Surprisingly low transition loss is found for a mode launcher for phase shifters [1], where no horn is used. The dielectric waveguide as the main part of this phase shifter is simply a rectangular ferrite rod tapered at the ends and placed on a substrate. The area of the cross section of this rod in the optimal configuration is smaller than a quarter of that of the standard waveguide (1.3x2.6 mm$^2$ vs. 7.2x3.6mm$^2$).

## 2.3. Low loss dielectric materials for DRW

If a dielectric material has loss tangent of about $10^{-4}$ and a relative permittivity of 10-15, losses can be expected to be in the order of 5 dB/m at 150 GHz while 10-12 dB/m is typical for the standard metal waveguide at this frequency. The properties of some dielectric materials which appear to be appropriate for DRWs are summarized in Table 2.1. There are some differences in data taken from different sources [15-28], because all the parameters depend on the material growth conditions, the method of its doping, etc.

Also wide band gap semiconductors AlN and GaN are now popular and are being investigated by many scientists [20-25]. These materials can have a very high resistivity and perhaps a very low loss tangent. However, there are no experimental data for monocrystal samples of these materials because of difficulties in growing them.

The most important parameters are the loss tangent measured at frequencies 120-170 GHz and the thermal conductivity. Looking at Si in [1], it is possible to calculate that its resistivity $10^4\Omega\cdot\mathrm{cm}$ corresponds to $\tan\delta\approx 0.07\cdot 10^{-3}$ compared with $0.08\cdot 10^{-3}$ measured in [1]. In comparison, it can be seen that in spite of that GaAs has a higher DC resistivity than Si, its loss tangent is higher than that of Si [1]. This means that high DC resistivity does not necessarily predict low losses at millimeter wavelengths. In [15] the properties of different dielectric materials can be found including GaAs and Si with DC resistivity ≈8000 Ω·cm. This resistivity of the silicon sample does not differ much from the resistivity of 11000 Ω·cm for the silicon sample in [16], but the values of the loss tangents are very different. Other materials reviewed in [15] have either low permittivity or high loss tangent and are not suitable for use in dielectric waveguide. However, Si may have a very low loss tangent. Si doped with boron with the loss tangent $4 \cdot 10^{-5}$ described in [16] can be appropriate for our purpose. Also in [17] the possibility of silicon having the loss tangent as low as $3 \pm 2 \cdot 10^{-6}$ at 145 GHz is discussed. Moreover an interesting effect was described in [17] that the dielectric loss behavior of silicon does not degrade after electron or neutron irradiation but is even improving. Another way to improve the dielectric properties of silicon is traditional, that is to compensate the conductivity by doping of acceptors. In [17] gold was used as an acceptor and also the effect of electron and neutron irradiation was investigated. The loss tangent for all the samples is shown graphically, and it drops nearly inversely proportional to the frequency. Therefore, one can expect that the dielectric properties of such silicon will be even more attractive at frequencies above 145 GHz. Thus, one can conclude that materials with a relatively high dielectric constant and a low loss tangent exist.

## 2.4. Conclusions

According to the author's opinion, there are three types of transitions from a standard metal waveguide to DRW (Fig. 2.7), which are most promising for open DRWs with relatively high dielectric permittivity ($\varepsilon_r = 9\text{-}12$). It will be interesting to investigate these types in more detail both experimentally and theoretically including high frequency field simulations.

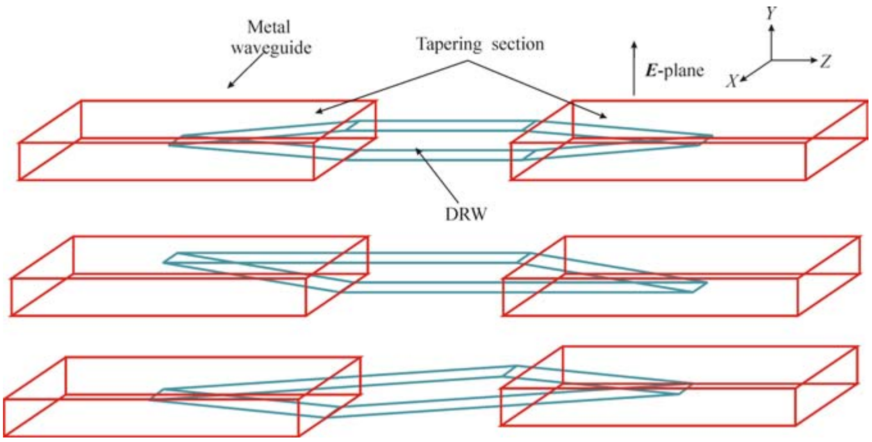

**Figure 2.7.** The most interesting transitions from standard metal waveguide to DRW.

**Table 2.1. Dielectric properties of materials (140 GHz)**

| Materials | **Si** | **Diamond** | **GaAs** | **BN** | **InP** | **GaN** | | **AlN** | **Ferrite** | **Sapphire** |
|---|---|---|---|---|---|---|---|---|---|---|
| Crystal structure | Diamond | Diamond | Zinc blende | Zinc blende | Zinc blende | Wurtzite | Zinc blende | Wurtzite | | Wurtzite |
| Lattice constants, Å | 5.43072 | 3.5597 | 5.65315 | 3.615 | 5.8688 | a=3.19<br>c=5.19 | 4.2-5.9 | a=3.111<br>c=4.978 | | |
| Relative Permittivity | 11.6-11.8 | 5.6644 | 10.9-13.03 | 3.1791 | 14 | 12.2 | | 7.7-9.5 | 13.32 (NiZn)<br>15.6 (Li)<br>15.05 (FeY) | 9.39 and 11.56 |
| Thermal conductivity, W/(cm·K) | 1.44 | 20 | 0.46 | 2 | 0.93 | 1.2-1.3<br>1.7-(th) | | 0.91-1.9<br>>3.0 (th) | | 0.47 |
| $\tan\delta, \times 10^{-4}$ | 0.03 | 0.06 | 3-14 (100-400 GHz) | 8-15 | | | | 4.5 (92.9 GHz) | 1.24-7.5 | 1.1-1.4 |
| DC resistivity, Ω·cm | >11 000 | | $>10^7$ | | | $>10^6$ | | $10^{11}$-$10^{14}$ | | |

(th) denotes theoretical value

# 3. Mathematical methods for rectangular dielectric waveguide structures

## 3.1. Introduction

The problem of calculating the propagation characteristics of a circular dielectric waveguide can be solved rigorously relatively easily by using Bessel functions. However, in the case of rectangular dielectric rod waveguide (DRW) the problem becomes rather complicated especially when the ratios of the permittivities of the core and the "cladding" regions are high. The reasons for those complications are described e.g. in [29]. The main reason for slow convergence of any numerical method is the presence of sharp corners of DRW. For example, if we consider the $x$-component of the field in a rectangular dielectric waveguide, this component at $x=a/2$ must be continuous for $|y|>b/2$ and discontinuous for $|y|<b/2$ (Fig. 3.1), as the permittivity is discontinuous here.

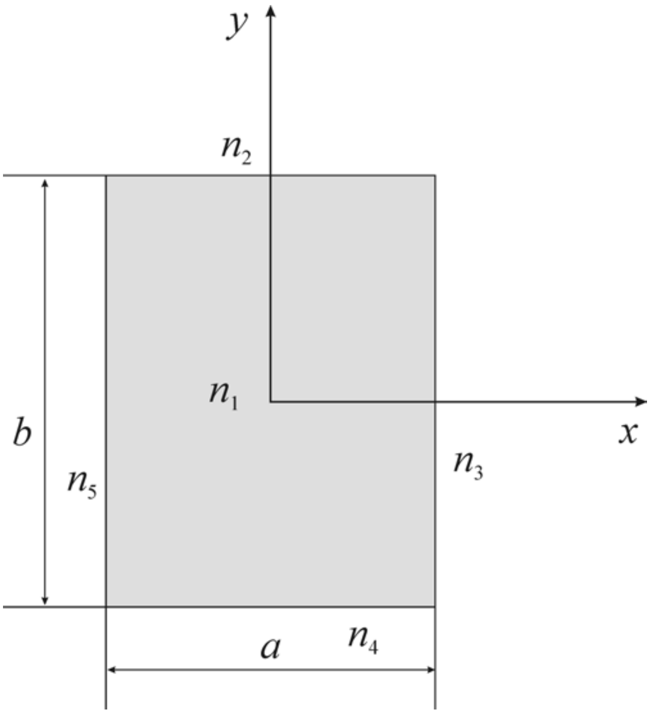

**Figure 3.1**. Cross-section of a rectangular DRW.

A series expansion of such field distribution suffers from the so-called "Gibbs" phenomenon. Also the transverse electric field components diverge at the corner roughly by power from 0 to -1/3 of $r$, where $r$ is the distance from the corner. The field behavior near the corner was a subject of investigation for over 30 years, that for itself says something about difficulty of the problem [29]. For example, it was shown that it is impossible to expand such a field distribution in increasing powers of $r$ times a function of the angle [30].

A good exposition of numerical methods for calculating general millimeter wave structures can be found e.g. in [31]. Many methods from there can be applied to the problem of rectangular DRW structures and particularly to open rectangular DRWs.

### 3.2. Finite difference method

In the simplest case this method can be explained for a two-dimensional problem with the Laplacian operator as follows: we divide the region of interest by a mesh (for example a rectangular grid with a small enough spacing *h*); then for each intersection point we make a Taylor expansion and express the quantities of the scalar potential for the adjacent points, add these relations and combine them with the differential equation to be solved. In that way we get a discretized version of the differential equation and write it for each point. Thus we get a matrix equation that can be solved. The main disadvantage of that method is that the matrices obtained are usually very large and much computer resources are consumed.

A realization of the finite difference method can be found e.g. in [32]. One variation of the finite difference method is the finite difference time domain method (FDTD), where Maxwell's equations in time domain are discretized. The finite difference method is very flexible in the sense that it allows to analyze arbitrary refractive index profiles and even anisotropic DRWs [33].

### 3.3. Finite element method

The method of finite elements is somewhat similar to the previous one (finite differences). The first step in this method is to divide the region of interest by a number of triangles (elements) (see e.g. [34,35]). A so-called shape function for each element is introduced as a polynomial:

$$\Phi(x,y) = \sum_{n=1}^{M} a_n(x,y)\phi_n, \tag{3.1}$$

which is a sum of the basis functions with weight coefficients depending on the coordinates (see e.g. [35]). Then the shape function can be expressed in terms of the nodal values of the field components. The further action depends on the particular formulation of the problem. It is impossible to describe briefly all the variants of the finite elements method. More details can be found in [31,34,35]. A comparison of different formulations is made in [36]. The general feature of this method is that a matrix equation has to be solved as the last step (an eigenvalue problem).

### 3.4. Variational methods

One realization of this method can be found e.g. in [37] for the simplest case of a dielectric slab waveguide. One must start with the Helmholtz equation

$$\frac{d^2\phi(x)}{dx^2}+\left[\varepsilon_r(x)k_0^2-\beta^2\right]\phi(x)=0, \tag{3.2}$$

multiply it by $\phi(x)$ and integrate it from minus infinity to plus infinity. After some transformations the following relation can be obtained for the propagation constant $\beta$:

$$\beta^2=\frac{\int\limits_{-\infty}^{+\infty}\phi(x)\frac{d^2\phi(x)}{dx^2}dx+k_0^2\int\limits_{-\infty}^{+\infty}\varepsilon_r(x)\phi^2(x)dx}{\int\limits_{-\infty}^{+\infty}\phi^2(x)dx}. \tag{3.3}$$

This is the so-called variational or stationary expression for the propagation constant. If we know the true field distribution, we can calculate the exact value of the propagation constant. Moreover, if we substitute some reasonable estimate of the field distribution, it can be shown, that the error in the estimate of $\beta$ will be relatively small.

The variational expression can be different depending on how it is derived. For example, in [38] the variational expression is given as

$$\begin{aligned}\iiint\Bigg[&\left(k_z^2-\varepsilon_r k_0^2\right)\left(\left|E_x\right|^2+\left|E_y\right|^2\right)+\left|\frac{\partial E_z}{\partial x}\right|^2+\left|\frac{\partial E_z}{\partial y}\right|^2+\left|\frac{\partial E_y}{\partial x}-\frac{\partial E_x}{\partial y}\right|^2-\\&-\varepsilon_r k_0^2\left|E_z\right|^2-jk_z\left(E_z^*\frac{\partial E_z}{\partial x}-E_x\frac{\partial E_z^*}{\partial x}+E_y^*\frac{\partial E_z}{\partial y}-E_y\frac{\partial E_z^*}{\partial y}\right)\Bigg]dA=0\end{aligned} \tag{3.4}$$

Then the field distribution is approximated with Marcatili's method, which is described below.

More information can be found in [31]. Variational methods are used also in the finite element method [31,34], and can also be used in the mode matching method [39]. A method of calculation of a lossy DRW is proposed in [40], and calculation of a lossy anisotropic waveguide in [41].

### 3.5. Integral equation method

For example, in the case of a waveguide consisting of homogeneous regions, the propagation characteristics can be found in terms of the transverse magnetic fields [42,43]. For each homogeneous section one can write:

$$\frac{1}{2}H(\mathbf{r}) = \int_C H(\mathbf{r}')\frac{\partial G(\mathbf{r},\mathbf{r}')}{\partial \mathbf{n}}d\mathbf{r}' - \oint_C G(\mathbf{r},\mathbf{r}')\frac{\partial H(\mathbf{r},\mathbf{r}')}{\partial \mathbf{n}}d\mathbf{r}', \tag{3.5}$$

where $H$ denotes $H_x$ or $H_y$, and $G$ is the two-dimensional Green's function. The first integral in the right-hand side of the equation denotes the Couchy principal value integral. This equation can be then solved numerically. Another integral equation method is proposed in [44].

### 3.6. Mode matching

In this method the field is presented as a sum of harmonics. For example, in [45] the problem of two coupled image DRWs can be reduced to that shown in Fig. 3.2.

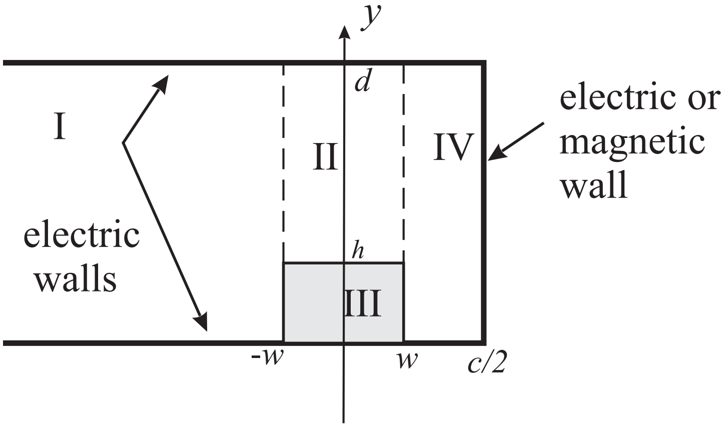

**Figure 3.2.** Cross-section calculated in [45].

The potential functions are represented as follows:

Region I

$$\Pi_1^y = \sum_{\nu=0}^{n} E_\nu \exp\left(\beta_{x\nu}^{(1)}(x+w)\right)\cos\left(\beta_{y\nu}^{(1)}y\right) \tag{3.6}$$

$$\Lambda_1^y = \sum_{\mu=0}^{n} F_\mu \exp\left(\tilde{\beta}_{x\mu}^{(1)}(x+w)\right)\cos\left(\tilde{\beta}_{y\mu}^{(1)}y\right) \tag{3.7}$$

Region II

$$\Pi_2^y = \sum_{\nu=1}^{m}\left\{A_\nu \sin\left(\beta_{x\nu}^{(2)}x\right) + A_\nu^{'} \cos\left(\beta_{x\nu}^{(2)}x\right)\right\}\cos\left(\beta_{y\nu}^{(2)}\left(y-d\right)\right) \tag{3.8}$$

$$\Lambda_2^y = \sum_{\mu=1}^{n}\left\{B_\mu \cos\left(\tilde{\beta}_{x\mu}^{(2)}x\right) + B_\nu^{'} \sin\left(\tilde{\beta}_{x\nu}^{(2)}x\right)\right\}\sin\left(\tilde{\beta}_{y\mu}^{(2)}\left(y-d\right)\right), \tag{3.9}$$

and so on. In other words, sinusoidal or exponential dependence is according to the situation (region number). Then we can write the boundary conditions for the tangential components of the fields to obtain the proper system of equations. A similar approach was used in [46, 53].

### 3.7. Method of lines

In this method the discretization is made only in two of the three dimensions or in one of the two of them. For the remaining dimension, an analytical solution has to be found. More details can be found e.g. in [31]. Many publications can be found on application of the method of lines to the isotropic dielectric waveguide problem, e.g. [47,48].

### 3.8. Iterative eigenfunction expansion method

The basics of the iterative eigenfunction method can be explained as follows [49,50]. Let us assume that we have an eigenvalue problem: $\mathbf{T}u - \lambda u = 0$, where **T** is an operator that can be presented as the difference between a self-adjoint operator **L** with the known set of eigenvalues ($\Lambda_\mathrm{i}$), eigenfunctions ($f_\mathrm{f}$) and a perturbation operator **F**, i.e. $\mathbf{T} = \mathbf{L} - \mathbf{F}$. The iteration loop is then organized as [49]:

A) Initial approximation of $u_0$, $\lambda_0$.

B) Expansion of the $k^{\text{-th}}$ approximation into series of the eigenfunctions of **L:**

$$\tilde{u}^{(k)} = \sum_i c_i^{(k)} f_i \text{, where } c_i^{(k)} = \frac{\left\langle \mathbf{F}u^{(k-1)}, f_i \right\rangle}{\Lambda_i - \lambda^{(k-1)}}. \tag{3.10}$$

C) Normalization:

$$u^{(k)} = \sum_i d_i^{(k)} f_i \text{, where } d_i^{(k)} = \frac{c_i^{(k)}}{\sqrt{\sum_i \left|c_i^{(k)}\right|^2}}. \tag{3.11}$$

D) Determination of the $k^{\text{-th}}$ approximation of the eigenvalue λ:

$$\lambda^{(k)} = \sum_i \Lambda_i \left|d_i^{(k)}\right|^2 - \sum_i d_i^{*(k)} \left\langle \mathbf{F}u^{(k)}, f_i \right\rangle. \tag{3.12}$$

Steps B, C, D can be repeated until the desired accuracy is reached. Authors in [49] report that their method is faster and takes less memory compared with the matrix oriented methods above.

### 3.9. Fourier decomposition

This method was first proposed in [51]. The start is at the Helmholtz eigenvalue problem:

$$\left(\frac{\partial^2}{\partial x^2}+\frac{\partial^2}{\partial y^2}+k^2n^2(x,y)-\beta^2\right)E(x,y)=0, \tag{3.13}$$

where the region of interest is limited by a box with the dimensions $L_x$ and $L_y$. The field distribution is expanded in sinusoidal basic functions:

$$\phi_i(x,y)=\frac{2}{\sqrt{L_xL_y}}\sin\left(\frac{m\pi x}{L_x}\right)\sin\left(\frac{n\pi y}{L_y}\right). \tag{3.14}$$

Expanding the field in these functions, substituting them in the Helmholtz equation, multiplying by $\phi_i$ and integrating over the entire region we get the following matrix equation:

$$\mathbf{A}v=\beta^2v, \tag{3.15}$$

where $v$ is the coefficient vector of the field expansion, and the matrix elements $A_{ij}$ are:

$$A_{ij}=-\left(\frac{m^2\pi^2}{L_x^2}+\frac{n^2\pi^2}{L_y^2}\right)\delta_{ij}+k^2\left\langle\phi_i(x,y)n^2(x,y)\phi_j(x,y)\right\rangle. \tag{3.16}$$

Thus, we get an eigenvalue problem that can be solved numerically. However, to obtain a good accuracy especially for waveguides made of materials with high permittivity, we have to take a large number of harmonics, which takes a lot of computing resources. The matrix, however, can be reduced by the Lanczos reduction scheme [52]. Another improvement can be found in [53], where the infinite cross section is transformed to a box with dimensions 1x1 using the following transformation functions:

$$x=a_x\tan\left[\pi\left(u-\frac{1}{2}\right)\right] \tag{3.17}$$

$$y = a_y \tan\left[\pi\left(v - \frac{1}{2}\right)\right], \tag{3.18}$$

where parameters $a_x$ and $a_y$ are arbitrary, however convergence depends on them. The Helmholtz equation is then properly transformed and then again expansion in sinusoidal functions is applied. The following steps are similar to those in [51,52], but the elements of the matrix obtained are different.

### 3.10. Circular harmonic method (point matching, Goell's method)

Instead of expanding the field distribution in sinusoidal functions, Goell [10] proposed to use the following: he expanded the longitudinal components of the electric and magnetic field as:

$$E_{z1} = \sum_{n=0}^{\infty} a_n J_n(hr)\sin(n\theta + \varphi_n)\exp\left[i(k_z z - \omega t)\right] \tag{3.19}$$

$$H_{z1} = \sum_{n=0}^{\infty} b_n J_n(hr)\sin(n\theta + \psi_n)\exp\left[i(k_z z - \omega t)\right] \tag{3.20}$$

inside the core of the dielectric waveguide and outside:

$$E_{z0} = \sum_{n=0}^{\infty} c_n K_n(pr)\sin(n\theta + \varphi_n)\exp\left[i(k_z z - \omega t)\right] \tag{3.21}$$

$$H_{z0} = \sum_{n=0}^{\infty} d_n K_n(pr)\sin(n\theta + \psi_n)\exp\left[i(k_z z - \omega t)\right] \tag{3.22}$$

Here $h = \left(k_1^2 - k_z^2\right)^{\frac{1}{2}}, p = \left(k_z^2 - k_0^2\right)^{\frac{1}{2}}$, $J$ and $K$ are the Bessel functions and the modified Bessel functions, respectively.

The sums are truncated at some number of modes $N$. Then the tangential field components are expressed and "tailored" at several points on the boundary. Symmetry simplifies the analysis [10] because one can consider only the first quadrant ($0 < \theta < \frac{\pi}{2}$) and select only odd or even numbers $n$ corresponding to the harmonics. For example for the odd harmonic case Goell chose matching points like $\theta_m = \left(m - \frac{1}{2}\right)\frac{\pi}{2N}$ with respect to the angle $\theta = 0$, where $N$ is the number of harmonics, and $\theta$ is the angle in the polar coordinates. As a result of this "tailoring" a system of equations is obtained, for which the determinant of its matrix should be equal to zero, otherwise no non-zero solution can exist.

This method is rather fast, converges rather well and is considered classical. A more rigorous solution without the limitation of matching only at the particular points is proposed in [54]. The same expansion of the longitudinal field components is used except that instead of sine (cosine) functions complex exponents are taken. Then the strict boundary conditions are written in terms of the longitudinal field components and their derivatives both in the tangential and normal directions. As a result, an infinite system of equations are obtained and the determinant of the matrix was equalized to zero. The solution there was much more complicated but more rigorous.

Some other numerical methods are also described in [55].

### 3.11. Approximation methods

The first numerical results were obtained by Schlösser [9] and Goell [10]. However, these methods are rather complicated, therefore approximate methods are also of interest.

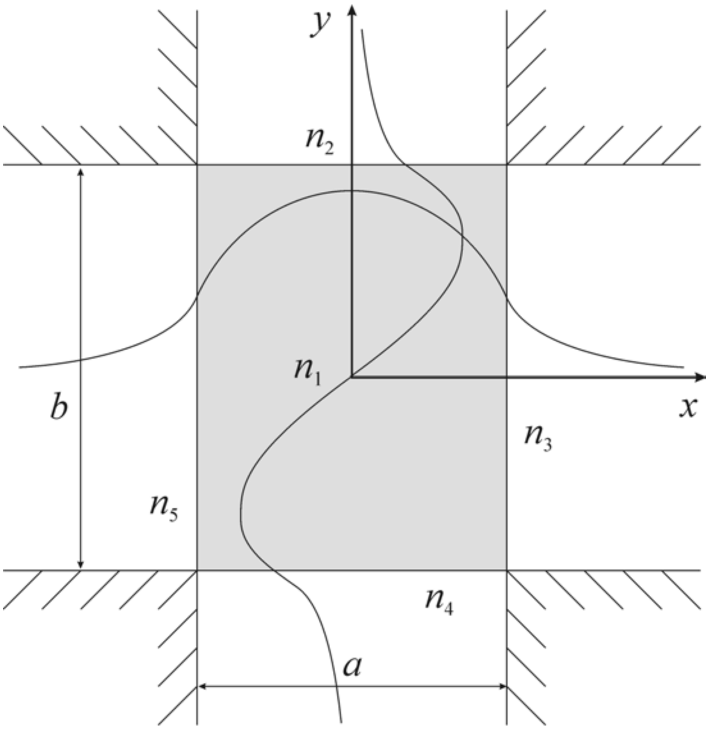

**Figure 3.3.** The geometry of the dielectric waveguide in Marcatili's method and the distributions of some field components.

The first approximation method was proposed by Marcatili [56]. It consists of the following assumptions: the field distributions of the strongest components are sinusoidal (cosinusoidal) within dielectric and decaying exponentially outside the dielectric medium, as shown in Fig. 3.3. Moreover, it is assumed that the dominant components are the transversal ones (but not all of them). Although this method was proposed for waveguides made of dielectrics with a small permittivity, for high enough frequencies it gives a good result also for dielectric waveguides even made of such materials as silicon, gallium arsenide or ferrite, which have relative permittivity between 10 and 14 [57]. The basic assumption is that one can neglect the fields in shaded regions (Fig. 3.3). The equations are obtained by matching the *z*-components, taking one component, say $H_y$=0, and then matching the dominant transversal components.

The propagation constant in the simplest case of a dielectric rod waveguide can be calculated according to this method using the following formulas:

$$k_z = \sqrt{\varepsilon_1 k_0^2 - k_x^2 - k_y^2}\,, \tag{3.23}$$

where $\varepsilon_1$ is the relative permittivity of the rod, $k_0$ is the wave number in vacuum. $k_x$ and $k_y$ one finds from transcendental equations for $E_{pq}^y$ modes:

$$k_x a = p\pi - 2\arctan\frac{k_x}{\xi}\,, \tag{3.24}$$

$$k_y b = q\pi - 2\arctan\frac{k_y}{\varepsilon_1 \eta}\,, \tag{3.25}$$

where $\xi = \sqrt{k_0^2(\varepsilon_1 - 1) - k_x^2}$ , $\eta = \sqrt{k_0^2(\varepsilon_1 - 1) - k_y^2}$ , $a$ and $b$ are the width and height of the waveguide, respectively. In the case of $E_{pq}^x$ mode indices $x$ and $y$ in these equations interchange. However at lower frequencies this assumption does not work and the dispersion characteristics do not agree well with the experiment.

Knox and Toulios [57] recognized that equations (3.24) and (3.25) correspond to the equations for two dielectric slab waveguides, vertical and horizontal, with corresponding thicknesses. For the dielectric rod waveguide these equations were modified introducing effective dielectric constant by

$$\varepsilon_{eff} = \varepsilon_1 k_0^2 - k_x^2 = k_{zslab}^2\,, \tag{3.26}$$

that can be substituted in (3.25) instead of $\varepsilon_1$. Here $k_x$ is calculated from (3.24).
Then one can substitute $\varepsilon_{eff}$ in equation (3.25) and find the propagation constant as

$$k_z = \sqrt{\varepsilon_{eff} k_0^2 - k_y^2}\,. \tag{3.27}$$

This method is interesting because it predicts that the lower modes of the rod dielectric waveguide do not experience cutoff at lower frequencies. This method can be applied also for more general waveguide structures.

The two methods above are the main approximation methods. There are different modifications of them. Marcatili's method was modified e.g. in [58] and [P3]. The main difference is that no field component is assumed to be zero. As in Marcatili's method the longitudinal components $H_z$ and $E_z$ are introduced with sinusoidal end exponential distribution, then the other field components are expressed through them. The equations are obtained by matching components $E_y$ and $E_x$ , then $H_y$ and $H_x$, and excluding in both cases the ratio between amplitudes of $H_z$ and $E_z$.

The effective dielectric constant method was modified by Marcatili and Hardy in [59]. Instead of substituting the original rectangular DRW with two dielectric slabs, two circular waveguides are used. One of them is circularly symmetric with some radial refractive index distribution while the other one has variation only in angular direction.

Interesting modification is described in [37]. An iterative technique can be applied, if the value $k_y$ from (3.25) is again substituted to find the effective dielectric constant and then from (3.24) find another value of $k_x$. This process can be repeated iteratively and has rather good convergence.

As to calculation of the attenuation constant, numerical methods giving electrical field distribution can be used by applying the formula:

$$\alpha = \frac{1}{2} \frac{P_a}{P}, \tag{3.28}$$

where $P_a$ is the power absorbed per unit length by the dielectric due to its losses, and $P$ is the propagating power.

Another approach is proposed in [57] and reviewed in [55]. This method proposes to solve equations (3.24) and (3.25) assuming that all the propagation constants $k_x, k_y, k_z, \xi, \eta$ are complex because the dielectric permittivity of the material of the rod $\varepsilon_1 = \varepsilon_r (1 - j \tan \delta)$ becomes complex. There are almost no experimental reports about dependence of the attenuation loss of the dielectric waveguide on the frequency separately from the excitation loss, only theoretical predictions are available in the literature. Another problem is that in most of the articles the authors considered dielectric waveguides made of materials with a relatively small dielectric constant (less than 3).

## 3.12. Conclusions

The main known methods for calculation of rectangular DRW structures have been reviewed. Unfortunately, the lack of experimental data does not allow to conclude which method is the most suitable. Usually authors give the calculated results for DRWs made of materials with a low relative permittivity (around 2.5) because DRW structures were mainly required for optical communication systems.

Nowadays dielectric materials with a high permittivity ($\varepsilon_r$ around 10) become of more interest for millimeter wave applications. However, existing methods require a lot of computational resources for their calculations. Moreover, different methods still give different results at frequencies near the cut-off because of different convergence of different methods.

Therefore both experimental and theoretical investigations are needed for DRW structures with high permittivity. From our point of view two methods deserve more attention: Marcatili's method because of its simplicity and Goell's method because of its efficiency.

Unfortunately, there are no publications on calculating anisotropic DRWs using the methods above with experimental verification, therefore this is one of the subjects of this thesis.

# 4. Methods of calculating anisotropic rectangular dielectric waveguides

## 4.1. Introduction

The uniaxial anisotropic DRW is nowadays of increasing interest. A simple theoretical approximation and/or numerical model for calculation of the propagation constant is required besides of complicated but powerful and accurate ones (see e.g. [33]). The most popular approximation method for a rectangular DRW is the well-known Marcatili's method [56] while the numerical one is the point-matching Goell's method [10]. However, these methods were developed for the case of isotropic materials. In this chapter simple approximation and numerical methods for the case of a rectangular DRW oriented along the optical axis were developed [P3, P4].

## 4.2. Extension of Marcatili's method

The case of the main interest is when the optical axis of the material coincides with the axis of DRW in order to avoid excitation of an orthogonal mode and/or rotation of the polarization plane. The $E_{11}^{y}$ fundamental mode of the rectangular DRW with cross section $a \times b$ has been chosen, and using its symmetry one can formulate the problem as shown in Fig. 4.1.

It was said in [57] that Marcatili's method for a rectangular DRW with cross section $a \times b$ consists of solving two dielectric slabs: a horizontal slab with thickness $b$ and a vertical slab with thickness $a$ for the same polarization. In this work we will derive, using the averaging method [60], the dispersion equation for a rectangular uniaxial anisotropic DRW in the most interesting case when the optical axis coincides with the $z$ axis of the DRW. This method allows to derive the dispersion equations without guessing the field distribution.

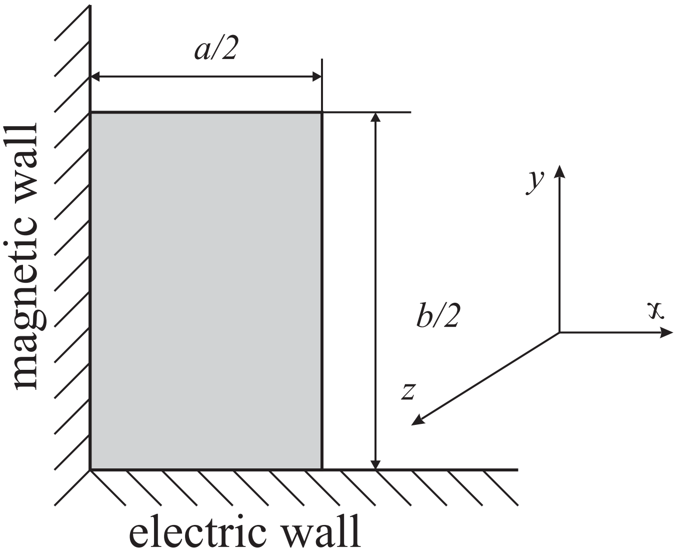

**Figure 4.1.** Cross-section of the waveguide problem.

One can show that there is no longitudinal component $E_z$, only $H_z$ in the case of the vertical dielectric slab for $E_1^y$ mode, owing to $\frac{\partial}{\partial y}=0$ and $H_y$=0 [55]. Thus only $E_y$ component is present, therefore the corresponding equation in Marcatili's method does not need to be changed.

Let us solve the dielectric slab problem shown in Fig. 4.2, when the dielectric permittivity is determined by matrix:

$$\varepsilon=\begin{vmatrix}\varepsilon_{\perp} & 0 & 0\\ 0 & \varepsilon_{\perp} & 0\\ 0 & 0 & \varepsilon_{\|}\end{vmatrix}, \tag{4.1}$$

where $\varepsilon_{\perp}=\varepsilon_{r\perp}\varepsilon_0$ denotes the permittivity in the direction normal to the optical axis, and $\varepsilon_{\|}=\varepsilon_{r\|}\varepsilon_0$ denotes that in the direction parallel to the optical axis.

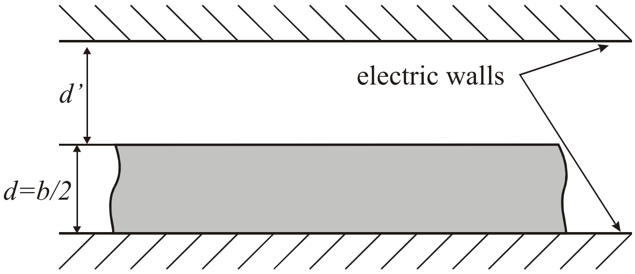

**Figure 4.2.** Anisotropic dielectric slab waveguide problem.

The main equations derived from [60] are:

$$\frac{\mathbf{n}\times\mathbf{E}_{t+}-\mathbf{n}\times\mathbf{E}_{t-}}{d}=-j\omega\mu\hat{\mathbf{H}}_t-\frac{1}{j\omega\varepsilon_{\perp}}\nabla_t\times\nabla_t\times\hat{\mathbf{H}}_t \tag{4.2}$$

$$\frac{\mathbf{n}\times\mathbf{H}_{t+}-\mathbf{n}\times\mathbf{H}_{t-}}{d}=-j\omega\varepsilon_{\|}\hat{\mathbf{E}}_t-\frac{1}{j\omega\mu}\nabla_t\times\nabla_t\times\hat{\mathbf{E}}_t \tag{4.3}$$

where $\hat{\mathbf{E}}_t=\left(\mathbf{E}_{t+}+\mathbf{E}_{t-}\right)f\left(\beta_y d\right)$, $\hat{\mathbf{H}}_t=\left(\mathbf{H}_{t+}+\mathbf{H}_{t-}\right)f\left(\beta_y d\right)$, $f\left(\beta_y d\right)=\frac{\tan\left(\frac{\beta_y d}{2}\right)}{\beta_y d}$.

The transversal propagation constant $\beta_y$ will be determined later. Subscript indexes *t*+ and *t*- denote the tangential components of the corresponding vector on upper and lower side of the slab, respectively. In our case $\mathbf{E}_{t-} = 0$ because of the presence of an electric wall.

The Helmholtz equations in uniaxial anisotropic medium for *E*z and *H*z components are [61]:

$$\begin{gathered}\nabla^2 E_z - \left(1 - \frac{\varepsilon_{r\|}}{\varepsilon_{r\perp}}\right)\frac{\partial^2 E_z}{\partial z^2} + \varepsilon_{r\|} k_0^2 E_z = 0 \\ \nabla^2 H_z + \varepsilon_{r\perp} k_0^2 H_z = 0.\end{gathered} \tag{4.4}$$

Substituting $E_z = E_z(x,y)e^{-jk_z z}$ and $\frac{\partial}{\partial x} = 0$ one obtains:

$$\frac{\partial^2 E_z}{\partial y^2} + \left(k_0^2 \varepsilon_{r\|} - \frac{\varepsilon_{r\|}}{\varepsilon_{r\perp}} k_z^2\right) E_z = 0\,. \tag{4.5}$$

Therefore for $\beta_y$:

$$\beta_y^2 = k_0^2 \varepsilon_{r\|} - \frac{\varepsilon_{r\|}}{\varepsilon_{r\perp}} k_z^2 = \frac{\varepsilon_{r\|}}{\varepsilon_{r\perp}}\left(k_0^2 \varepsilon_{r\perp} - k_z^2\right). \tag{4.6}$$

Substituting into Eq. (4.2) $\nabla_t = -jk_z \mathbf{z}$ and rewriting these equations for *x*- and *z*- components separately one obtains:

*x-components*

$$\begin{aligned}\frac{E_{z+}}{d} &= -j\omega\mu\left(H_{x+} + H_{x-}\right) f\left(\beta_y d\right) + \frac{-1}{j\omega\varepsilon_\perp} k_z^2 \left(H_{x+} + H_{x-}\right) f\left(\beta_y d\right) = \\ &= \frac{\omega^2 \mu\varepsilon_\perp - k_z^2}{j\omega\varepsilon_\perp}\left(H_{x+} + H_{x-}\right) f\left(\beta_y d\right) = \frac{\beta_y^2}{j\omega\varepsilon_\|}\left(H_{x+} + H_{x-}\right) f\left(\beta_y d\right)\end{aligned} \tag{4.7}$$

$$\begin{aligned}\frac{H_{z+} - H_{z-}}{d} &= j\omega\varepsilon_\perp E_{x+} f\left(\beta_y d\right) - \frac{-1}{j\omega\mu} k_z^2 E_{x+} f\left(\beta_y d\right) = \\ &= \frac{-\omega^2 \varepsilon_\perp \mu + k_z^2}{j\omega\mu} E_{x+} f\left(\beta_y d\right)\end{aligned} \tag{4.8}$$

*z-components*

$$-\frac{E_{x+}}{d} = -j\omega\mu\left(H_{z+} + H_{z-}\right) f\left(\beta_y d\right) \tag{4.9}$$

$$-\frac{H_{x+} - H_{x-}}{d} = j\omega\varepsilon_{\parallel} E_{z+} f\left(\beta_y d\right). \tag{4.10}$$

One can notice that in Eqs. (4.7) and (4.10) only $H_x$ and $E_z$ are present while in Eqs. (4.8) and (4.9) we can find only $H_z$ and $E_x$ components. Let us choose equations corresponding to $E_1^y$ polarization, i.e. $E_x$ and $H_z$ equal to zero (Eqs. (4.7) and (4.10)).

Excluding $H_{x-}$ one obtains:

$$2H_{x+} = j\omega\varepsilon_{\parallel} E_{z+}\left[\frac{1}{d}\frac{1}{\beta_y^2}\frac{1}{f\left(\beta_y d\right)} - df\left(\beta_y d\right)\right] = j\omega\varepsilon_{\parallel} E_{z+}\frac{2}{\beta_y}\frac{1}{\tan\left(\beta_y d\right)} \tag{4.11}$$

For the air layer in Fig. 4.2 we can write similarly:

$$2H_{x+} = -j\omega\varepsilon_0 E_{z+}\frac{2}{\beta_y'}\frac{1}{\tan\left(\beta_y' d'\right)}, \tag{4.12}$$

where $\beta_y'^2 = k_0^2 - k_z^2$.

When $d'$ tends to infinity Eq. (4.12) becomes [60]:

$$H_{x+} = j\omega\varepsilon_0 E_{z+}\frac{j}{\beta_y'}. \tag{4.13}$$

Combining these two equations we get:

$$\frac{\varepsilon_{r\parallel}}{\beta_y}\frac{1}{\tan\left(\beta_y d\right)} = \frac{j}{\beta_y'}. \tag{4.14}$$

Introducing $k_y = \beta_y$, $k_{y2} = \frac{\beta_y'}{j}$, $b = 2d$ and using relation $\frac{1}{\tan(x)} = \tan\left(\frac{\pi}{2} - x\right)$, an equation similar to "Marcatili's equation" [55,56] can be obtained:

$$k_y b = \pi + 2\pi n - 2\arctan\left(\frac{1}{\varepsilon_{r\parallel}}\frac{k_y}{k_{y2}}\right), \tag{4.15}$$

where $n$ =0,1,2,3 …, $k_y = \sqrt{\frac{\varepsilon_{\parallel}}{\varepsilon_{\perp}}\left(k_0^2\varepsilon_{r\perp} - k_z^2\right)}$, $k_{y2} = \sqrt{k_z^2 - k_0^2}$. $n = 0$ corresponds to the $E_1^y$ fundamental mode. To get the rest of the possible modes ($E_z$ is even with respect to $y$ = 0 plane) one can put the slab onto a magnetic wall. The second "Marcatili's equation" is [56]:

$$k_x a = \pi q - 2\arctan\left(\frac{k_x}{k_{x3}}\right), \tag{4.16}$$

where $k_{x3} = \sqrt{k_0^2(\varepsilon_{r\perp} - 1) - k_x^2}$, $q$ =1,2,3 … .

Thus the solution procedure can be as follows. Using Eq. (4.15) one can find $k_z$, then solve Eq. (4.16) for $k_x$, and eventually correct $k_z$ with:

$$k_{z\text{final}}^2 = \sqrt{k_z^2 - k_x^2}\ . \tag{4.17}$$

Experiments were carried out in order to verify the calculated numerical results. Sapphire was chosen as the material for DRW because it is a typical example of a uniaxial anisotropic dielectric. *S*-parameter measurements of a sapphire DRW were carried out with VNA HP 8510 using the direct connection of the input and output as a reference. The monocrystalline Sapphire DRW oriented along the optical axis with dimensions: cross section of 1.0 × 0.5 mm$^2$, total length of 112 mm and tapering section length of 6 mm (Fig. 4.3), was used for the vector measurements [62].

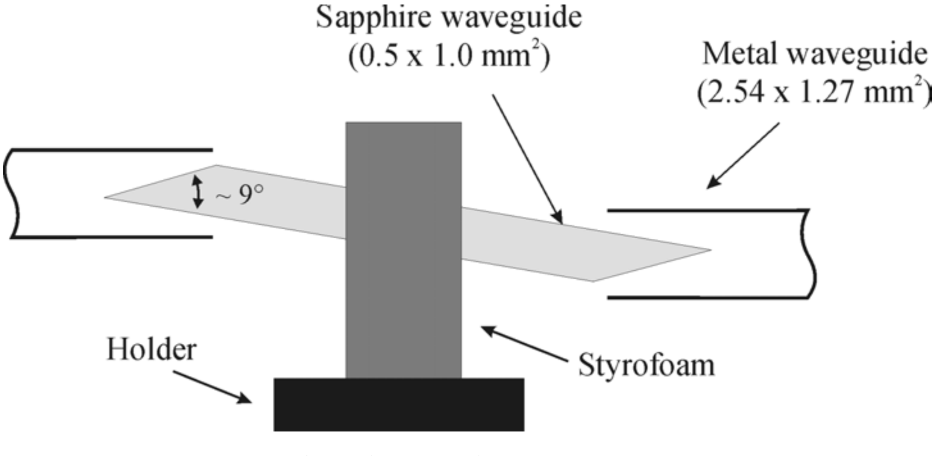

**Figure 4.3.** Schematic setup of DRW vector measurements.

The numerical results are summarized in Fig. 4.4. Eqs. (4.15)-(4.17) were used to obtain the propagation constant for uniaxial anisotropic waveguides for four combinations of $\varepsilon_{r\perp}$ and $\varepsilon_{r\parallel}$: 11.56

and 11.56; 11.56 and 9.39; 9.39 and 11.56 (which corresponds to Sapphire [26]); 9.39 and 9.39, respectively.

The wavelength was measured directly at the frequency of 75 GHz by using a movable discontinuity (a metal rectangular "ring") in order to obtain a reference point. The phase values were corrected ($-2\pi n$ correction) to obtain continuous dependence of phase vs. frequency. Assuming a constant dielectric waveguide length $L$ we can write: $\Delta k = \frac{\Delta\phi}{L}$, where $\Delta\phi$ is the phase shift change when the frequency changes by a small step to the next point, and $\Delta k$ is a change in the propagation constant in the dielectric waveguide. After obtaining the wavelength at one point by using the phase data, one can calculate the propagation constants at other frequencies (Fig. 4.4, curve 3). For comparison the normalized propagation constant measurements were repeated at 80, 85, 90 and 94 GHz; the results are shown in Fig. 4.4 [P3].

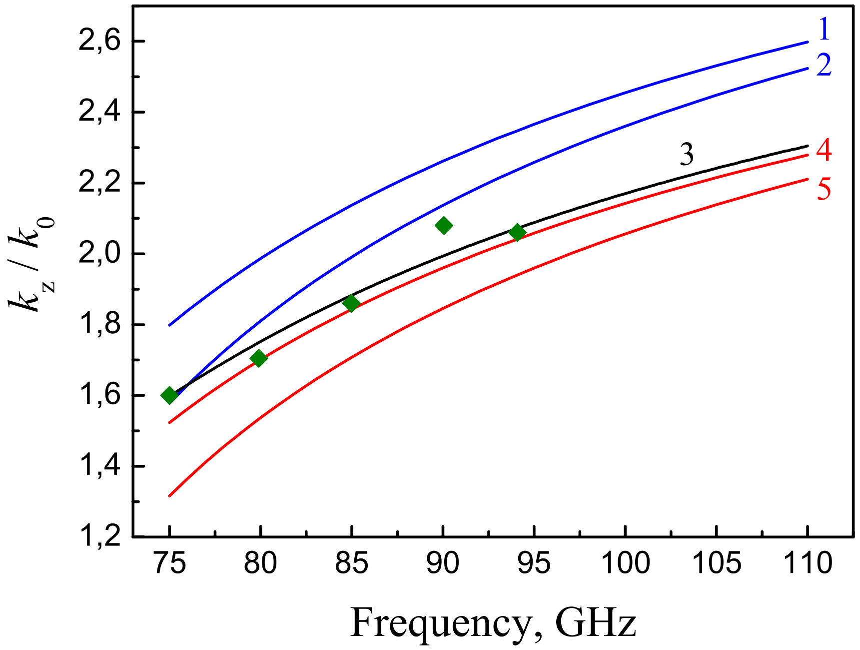

**Figure 4.4.** $\frac{k_z}{k_0}$ of DRW made of uniaxial anisotropic materials with cross dimensions of 1.0 x 0.5 mm$^2$. Marcatili's method. Curves 1,2,4 and 5 calculated using the modified Marcatili's method.

(1) $\varepsilon_{r\perp}$=11.56, $\varepsilon_{r\parallel}$=11.56; (2) $\varepsilon_{r\perp}$=11.56, $\varepsilon_{r\parallel}$=9.39; (3) curve calculated using experimental phase measurement results and measured $k_z$ at 75GHz; (4) $\varepsilon_{r\perp}$=9.39, $\varepsilon_{r\parallel}$=11.56; (5) $\varepsilon_{r\perp}$=9.39, $\varepsilon_{r\parallel}$=9.39; ♦ – directly measured experimental points.

One can see in Fig. 4.4 (curves 3 and 4) that the modified Marcatili's method for the sapphire DRW show good agreement with the experimental data. The fact that the theoretical curve lies below the experimental one can be explained by the approximative nature of the Marcatili's method.

Comparing curves 1 with 2 and 4 with 5 one can see that the anisotropy changes the propagation characteristic considerably. Dispersion is stronger, as for curve 2, when $\varepsilon_{||}$ is smaller than $\varepsilon_{\perp}$, or weaker, when $\varepsilon_{||}$ is larger than $\varepsilon_{\perp}$, as for curve 4. The latter could be explained as follows. When the frequency is very high, there is almost no longitudinal electric field component, and the propagation constant is mainly determined by $\varepsilon_{\perp}$. When the frequency drops, the longitudinal component of the electric field becomes larger; therefore the effect of larger $\varepsilon_{||}$ becomes stronger and thus $\frac{k_z}{k_0}$ increases. Similarly one can explain why the dispersion seen in curve 2 is stronger.

However, Marcatili's method does not give a good accuracy at lower frequencies. For better accuracy many powerful numerical methods have been developed such as the finite element or the finite difference methods that were described in the previous chapter. The main disadvantage of these methods is that they are so-called matrix-oriented methods, which are computing resources consuming. Many authors compare their calculating results with the classical Goell's method [10]. This method is rather effective, fast and can be relatively easily implemented in MatLab™ using its matrix routines. We will modify it to calculate also uniaxial anisotropic DRWs.

### 4.3. Modification of Goell's method for anisotropic DRWs

The $E_{11}^{y}$ fundamental mode of the waveguide has been chosen, and using its symmetry, one can formulate the problem as shown in Fig. 4.5.

The case when the optical axis of the dielectric material coincides with the axis of the DRW is of interest. Therefore let us introduce again the permittivity matrix as:

$$\varepsilon_1 = \begin{vmatrix} \varepsilon_{\perp} & 0 & 0 \\ 0 & \varepsilon_{\perp} & 0 \\ 0 & 0 & \varepsilon_{||} \end{vmatrix}, \tag{4.18}$$

where the axis $z$ is directed along the waveguide.

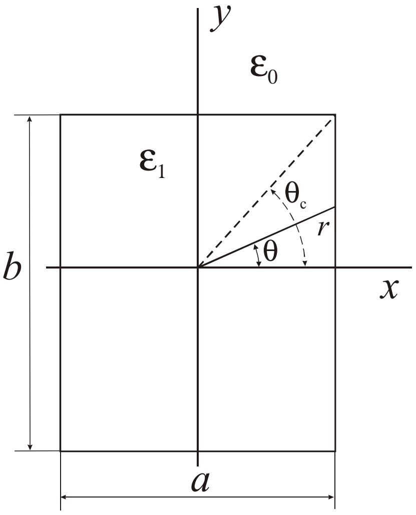

**Figure 4.5.** Dimensions of the dielectric waveguide and the coordinate system [10].

Similarly to [10] we assume that the longitudinal components of the electric and magnetic fields are distributed as:

$$E_{z1} = \sum_{n=0}^{\infty} a_n J_n\left(h_E r\right)\sin\left(n\theta + \varphi_n\right)\exp\left[i\left(k_z z - \omega t\right)\right] \tag{4.19}$$

$$H_{z1} = \sum_{n=0}^{\infty} b_n J_n\left(h_M r\right)\sin\left(n\theta + \psi_n\right)\exp\left[i\left(k_z z - \omega t\right)\right] \tag{4.20}$$

inside the core and

$$E_{z0} = \sum_{n=0}^{\infty} c_n K_n\left(pr\right)\sin\left(n\theta + \varphi_n\right)\exp\left[i\left(k_z z - \omega t\right)\right] \tag{4.21}$$

$$H_{z0} = \sum_{n=0}^{\infty} d_n K_n\left(pr\right)\sin\left(n\theta + \psi_n\right)\exp\left[i\left(k_z z - \omega t\right)\right], \tag{4.22}$$

where $k_z$ is the propagation constant, $J_n$ and $K_n$ are $n^{\text{th}}$ order Bessel and modified Bessel of second kind functions respectively, $\varphi_n$ and $\psi_n$ are some arbitrary phase constants, and $p^2 = k_z^2 - k_0^2$.

The main difference of these equations from [10] is in the transversal propagation constants $h_E$ and $h_M$, which are [61]:

$$h_M^2 = k_0^2\varepsilon_\perp - k_z^2 \tag{4.23}$$

$$h_E^2 = k_0^2\varepsilon_\parallel - \frac{\varepsilon_\parallel}{\varepsilon_\perp}k_z^2 = h_M^2\frac{\varepsilon_\parallel}{\varepsilon_\perp}. \tag{4.24}$$

We will calculate the symmetric $E_{11}^{y}$ fundamental mode. Therefore, using the symmetry, we write: $\varphi_n = 0$, $\psi_n = \frac{\pi}{2}$ (see [10]) and consider $\theta$ lying only between 0 and $\frac{\pi}{2}$.

It can be shown using [61] that the equations for the transverse components of the fields have not to be changed:

$$E_r = \frac{ik_z}{k^2 - k_z^2}\left[\frac{\partial E_z}{\partial r} + \left(\frac{\mu_0\omega}{k_z r}\right)\frac{\partial H_z}{\partial \theta}\right] \tag{4.25}$$

$$E_\theta = \frac{ik_z}{k^2 - k_z^2}\left[\frac{1}{r}\frac{\partial E_z}{\partial \theta} + \left(\frac{\mu_0\omega}{k_z}\right)\frac{\partial H_z}{\partial r}\right] \tag{4.26}$$

$$H_r = \frac{ik_z}{k^2 - k_z^2}\left[-\left(\frac{k^2}{\mu_0\omega k_z r}\right)\frac{\partial E_z}{\partial \theta} + \frac{\partial H_z}{\partial r}\right] \tag{4.27}$$

$$H_\theta = \frac{ik_z}{k^2 - k_z^2}\left[-\left(\frac{k^2}{\mu_0\omega k_z}\right)\frac{\partial E_z}{\partial r} + \frac{1}{r}\frac{\partial H_z}{\partial \theta}\right]. \tag{4.28}$$

The tangential components of the electric field are similarly given by

$$E_t = E_r \sin(\theta) + E_\theta \cos(\theta), \text{ if } \theta < \theta_c \tag{4.29}$$

$$E_t = -E_r \cos(\theta) + E_\theta \sin(\theta), \tag{4.30}$$

where $\theta_c$ is explained in Fig. 4.5.

The next step is to match the longitudinal field components. The matching points have been chosen to be

$$\theta_m = \frac{\left(m - \frac{1}{2}\right)\pi}{2N}, \tag{4.31}$$

$m$=1,2,…$N$ is the number of the point for the fields to be matched at, where $N$ is the number of harmonics. Moreover, we choose only odd $n$ in equations (4.19-4.22). After matching, a similar matrix can be obtained like in [10], but with the components changed:

$$e_{mn}^{LA} = J_E S \tag{4.32}$$

$$e_{mn}^{LC} = KS \tag{4.33}$$

$$h_{mn}^{LB} = J_M C \tag{4.34}$$

$$h_{mn}^{LD} = KC \tag{4.35}$$

$$e_{mn}^{TA} = k_z \left[ \mathbf{J}^{'}_E SR + \mathbf{J}_E CT \right] \tag{4.36}$$

$$e_{mn}^{TB} = k_0 z_0 \left[ \mathbf{J}_M SR + \mathbf{J}^{'}_M CT \right] \tag{4.37}$$

$$e_{mn}^{TC} = k_z \left[ \mathbf{K}^{'} SR + \mathbf{K} CT \right] \tag{4.38}$$

$$e_{mn}^{TD} = -k_z Z_0 \left[ \mathbf{K} SR + \mathbf{K}^{'} CT \right] \tag{4.39}$$

$$h_{mn}^{TA} = \varepsilon_{\perp} k_0 \left[ \mathbf{J}_E CR - \mathbf{J}^{'}_E ST \right] / Z_0 \tag{4.40}$$

$$h_{mn}^{TB} = -k_z \left[ \mathbf{J}^{'}_M CR - \mathbf{J}_M ST \right] \tag{4.41}$$

$$h_{mn}^{TC} = -k_0 \left[ \mathbf{K} CR - \mathbf{K}^{'} ST \right] / Z_0 \tag{4.42}$$

$$h_{mn}^{TD} = k_z \left[ \mathbf{K}^{'} CR - \mathbf{K} ST \right], \tag{4.43}$$

i.e., used Bessel functions are separated to “electric” (*E* subscript) and “magnetic” (*M* subscript) kinds, and:

$$Z_0 = \sqrt{\frac{\mu_0}{\varepsilon_0}} \tag{4.44}$$

$$S = \sin\left( (2n-1)\,\theta_m + \varphi \right) \tag{4.45}$$

$$C = \cos\left( (2n-1)\,\theta_m + \varphi \right) \tag{4.46}$$

$$\varphi = 0$$

$$J_E = J_{2n-1}\left(h_E r_m\right),\ J_M = J_{2n-1}\left(h_M r_m\right),\ K = K_{2n-1}\left(p r_m\right) \tag{4.47}$$

$$\mathbf{J}_E = \frac{(2n-1)\,J_{2n-1}\left(h_E r_m\right)}{h_M^2 r_m} \quad (4.48), \qquad \mathbf{J}_M = \frac{(2n-1)\,J_{2n-1}\left(h_M r_m\right)}{h_M^2 r_m} \quad (4.49)$$

$$\mathbf{J}^{'}_E = \frac{J^{'}_{2n-1}\left(h_E r_m\right)}{h_E} \frac{\varepsilon_{\parallel}}{\varepsilon_{\perp}} \quad (4.50), \qquad \mathbf{J}^{'}_M = \frac{J^{'}_{2n-1}\left(h_M r_m\right)}{h_M} \quad (4.51)$$

$$R = \begin{cases} \sin\theta_m, \theta < \theta_c \\ -\cos\theta_m, \theta > \theta_c \end{cases} \quad (4.52), \qquad T = \begin{cases} \cos\theta_m, \theta < \theta_c \\ \sin\theta_m, \theta > \theta_c \end{cases} \quad (4.53)$$

$$r_m = \begin{cases} \dfrac{a}{2\cos\theta_m}, \theta < \theta_c \\ \dfrac{b}{2\sin\theta_m}, \theta > \theta_c \end{cases} \quad (4.54), \qquad \theta_m = \frac{m-\frac{1}{2}}{2N}\pi \quad (4.55), \qquad \theta_c = \arctan\frac{b}{a}. \ (4.56)$$

Finally, the following matrix leads to the determinant which has to be equalized to zero:

$$\begin{vmatrix} E^{LA} & 0 & -E^{LC} & 0 \\ 0 & H^{LB} & 0 & -H^{LD} \\ E^{TA} & E^{TB} & -E^{TC} & -E^{TD} \\ H^{TA} & H^{TB} & -H^{TC} & -H^{TD} \end{vmatrix} = 0. \qquad (4.57)$$

In Fig. 4.6 the calculated results are presented. The difference from Fig. 4.4 is that the theoretical results are now computed using the modified Goell's method [P4].

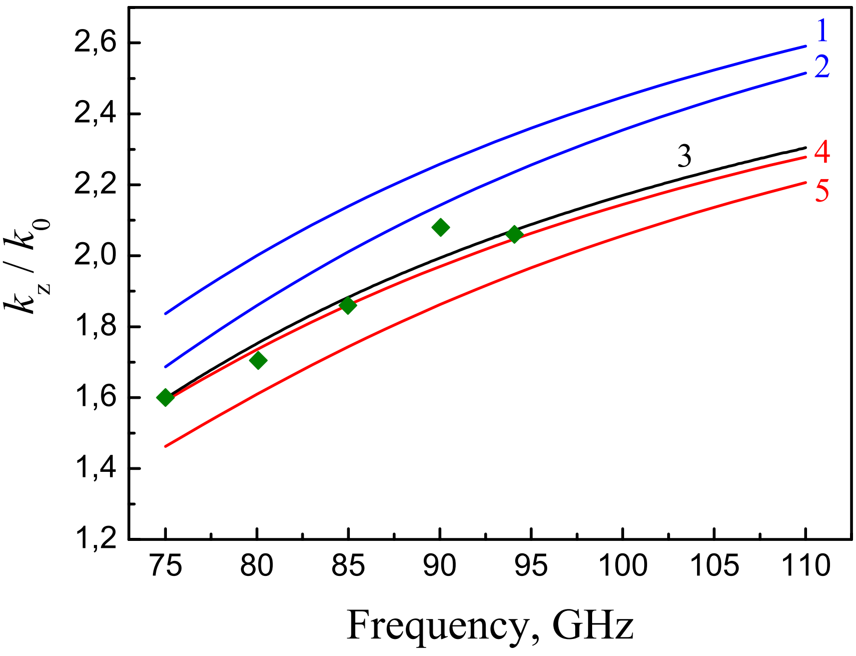

**Figure 4.6.** $\dfrac{k_z}{k_0}$ of DRWs made of uniaxial anisotropic materials with cross dimensions of 1.0 x 0.5 mm$^2$. Curves 1,2,4 and 5 are calculated using the modified Goell's method.

(1) $\varepsilon_{r\perp}$=11.56, $\varepsilon_{r\|}$=11.56; (2) $\varepsilon_{r\perp}$=11.56, $\varepsilon_{r\|}$=9.39; (3) curve calculated using experimental phase measurement results and measured $k_z$ at 75GHz; (4) $\varepsilon_{r\perp}$=9.39, $\varepsilon_{r\|}$=11.56; (5) $\varepsilon_{r\perp}$=9.39, $\varepsilon_{r\|}$=9.39; ♦ – directly measured experimental points.

One can see in Fig. 4.6 (curves 3 and 4) that the modified Goell's method applied for the sapphire DRW gives good agreement with the experimental data, better than the previous Marcatili's method.

## 4.4. Is it possible to have a negative slope of the $\frac{k_z}{k_0}$ characteristic?

It was mentioned above that larger "longitudinal permittivity" could decrease the dispersion. The question here is whether it can happen so that the effective refractive index decreases when the frequency increases? To answer this question let us consider a uniaxial dielectric slab with the thickness *d*. Let us rewrite Eq. (4.15):

$$\frac{\varepsilon_{r\parallel}}{\beta_y}\frac{1}{\tan\left(\beta_y d\right)}=\frac{j}{\beta_y^{'}} \tag{4.58}$$

$$\tan\left(k_y d\right)=\varepsilon_{r\parallel}\frac{k_{y2}}{k_y}\text{, where } 2d=b \tag{4.59}$$

$$k_y=\sqrt{\varepsilon_{r\parallel}k_0^2-\frac{\varepsilon_{r\parallel}}{\varepsilon_{r\perp}}k_z^2} \tag{4.60}$$

$$k_{y2}=\sqrt{k_z^2-k_0^2} \tag{4.61}$$

$$k_y^{'}=\frac{\varepsilon_{r\parallel}k_0-\frac{\varepsilon_{r\parallel}}{\varepsilon_{r\perp}}k_z k_z^{'}}{k_y} \tag{4.62}$$

$$k_{y2}^{'}=\frac{k_z k_z^{'}-k_0}{k_{y2}} \tag{4.63}$$

Differentiating (4.59) with respect to $k_0$ and using equation $\tan^{'}\left(x\right)=1+\tan^2\left(x\right)$ one can write:

$$\left(1+\varepsilon_{r\parallel}^2\frac{k_{y2}^2}{k_y^2}\right)k_y^{'}d=\varepsilon_{r\parallel}\frac{k_{y2}^{'}k_y-k_y^{'}k_{y2}}{k_y^2}\text{, or} \tag{4.65}$$

$$k_y^{'}\left[\left(k_y^2+\varepsilon_{r\parallel}^2k_{y2}^2\right)d+\varepsilon_{r\parallel}k_{y2}\right]=k_{y2}^{'}\varepsilon_{r\parallel}k_y\,. \tag{4.66}$$

Introducing $\xi=\left(k_y^2+\varepsilon_{r\parallel}^2k_0^2\right)d+\varepsilon_{r\parallel}k_{y2}$ and substituting (4.62) and (4.63) for the derivatives one can obtain:

$$\xi\frac{\varepsilon_{r\parallel}k_0-\frac{\varepsilon_{r\parallel}}{\varepsilon_{r\perp}}k_zk_z^{'}}{k_y}=\varepsilon_{r\parallel}\frac{k_zk_z^{'}-k_0}{k_{y2}}k_y\,, \tag{4.66}$$

which can be rearranged as

$$k_0\left(\xi\frac{1}{k_y}+\frac{k_y}{k_{y2}}\right)=k_zk_z^{'}\left(\frac{k_y}{k_{y2}}+\xi\frac{1}{\varepsilon_{r\perp}k_y}\right), \tag{4.67}$$

then

$$k_0\left(\xi k_{y2}+k_y^2\right)=k_zk_z^{'}\left(\varepsilon_{r\perp}k_y^2+\xi k_{y2}\right)\frac{1}{\varepsilon_{r\perp}}\,, \tag{4.68}$$

$$k_0=k_zk_z^{'}\frac{1}{\varepsilon_{r\perp}}\frac{\varepsilon_{r\perp}k_y^2+\xi k_{y2}}{k_y^2+\xi k_{y2}}\,. \tag{4.69}$$

As

$$\xi k_{y2}=\left(k_y^2+\varepsilon_{r\parallel}^2k_0^2\right)d\cdot k_{y2}+\varepsilon_{r\parallel}k_{y2}^2\,, \tag{4.70}$$

therefore

$$k_0<k_zk_z^{'}\frac{1}{\varepsilon_{r\perp}}\frac{\varepsilon_{r\perp}k_y^2+\varepsilon_{r\parallel}k_{y2}^2}{k_y^2+\varepsilon_{r\parallel}k_{y2}^2}=k_z^{'}\frac{1}{\varepsilon_{r\perp}}\frac{k_0^2\left(\varepsilon_{r\perp}-1\right)}{k_z\left(1-\frac{1}{\varepsilon_{r\perp}}\right)}=k_z^{'}\frac{k_0^2}{k_z} \tag{4.71}$$

and $k_z^{'}k_0>k_z$.

Thus,

$$\left(\frac{k_z}{k_0}\right)^{\prime}=\frac{k_z^{\prime}k_0-k_z}{k_0^2}>0\,. \tag{4.72}$$

Moreover, this derivative equals zero only at zero and infinite frequencies.

## 4.5. Expressing the critical frequencies for higher modes

We can define the critical frequency as the frequency at which the propagation constant becomes equal to that in the environment, i.e. $k_z=k_0$. In the case of a rectangular DRW there is no analytical expression for the critical frequency for higher modes. However, in case of a dielectric slab, which is much simpler, it is possible to derive such an expression.

Let us rewrite eq. (4.16) for y-polarization and (4.17) for x-polarization:

$$k_y b = \pi p - 2\arctan\left(\frac{1}{\varepsilon_{r\|}}\frac{k_y}{k_{y2}}\right), \tag{4.73}$$

$$k_y^2 = \frac{\varepsilon_{r\|}}{\varepsilon_{r\perp}}\left(k_0^2\varepsilon_{r\perp} - k_z^2\right), \tag{4.74}$$

$$k_{y2}^2 = k_0^2 - k_z^2; \tag{4.75}$$

$$k_x a = \pi q - 2\arctan\left(\frac{k_x}{k_{x3}}\right), \tag{4.76}$$

$$k_x^2 = k_0^2\varepsilon_{r\perp} - k_z^2, \tag{4.77}$$

$$k_{x3}^2 = k_0^2 - k_z^2. \tag{4.78}$$

When $k_z = k_0$, instead of arctan() in both (4.15) and (4.16) we can write $\frac{\pi}{2}$, therefore

$$k_y b = \pi(p-1) \tag{4.79}$$

$$k_x a = \pi(q-1). \tag{4.80}$$

Using that $k_z^2 = k_0^2 = k_0^2\varepsilon_{r\perp} - k_y^2\frac{\varepsilon_{r\perp}}{\varepsilon_{r\|}}$ for *y*-polarization and $k_z^2 = k_0^2 = k_0^2\varepsilon_{r\perp} - k_x^2$ for x-polarization we can find the critical wave number $k_0$:

$$k_{0\text{cr}}^2\left(\varepsilon_{r\perp} - 1\right) = \left[\frac{\pi}{b}(p-1)\right]^2\frac{\varepsilon_{r\perp}}{\varepsilon_{r\|}} \tag{4.81}$$

and

$$k_{0\text{cr}}^2\left(\varepsilon_{r\perp} - 1\right) = \left[\frac{\pi}{a}(q-1)\right]^2 \tag{4.82}$$

respectively. One can see that the two fundamental modes ($p = 1$ or $q = 1$) both have zero cut-off frequency.

### 4.6. Comparison of Marcatili's and Goell's methods for anisotropic DRWs

In Fig. 4.7 a comparison of calculated results are shown for both Marcatili's and Goells's methods. A wider frequency range has been considered. A rectangular sapphire DRW with 1.0 x 0.5 mm$^2$ cross-section was again taken as a sample. Experimental data are also shown. Here red lines present the results given by Marcatili's method while the blue lines correspond to Goell's method. One can see that for both fundamental modes, namely $E_{11}^{y}$ and $E_{11}^{x}$, both methods give results close to each other. However, Marcatili's method "predicts" a cut-off for $E_{11}^{x}$ mode at approximately 90 GHz, which is not true.

Looking at the experimental results one can see that Goell's method gives more accurate results, but the much simpler Marcatili's method works quite well when the effective refractive index $\frac{k_z}{k_0}$ is larger than 1.6. Also, Goell's method becomes rather problematic near cut-off frequencies.

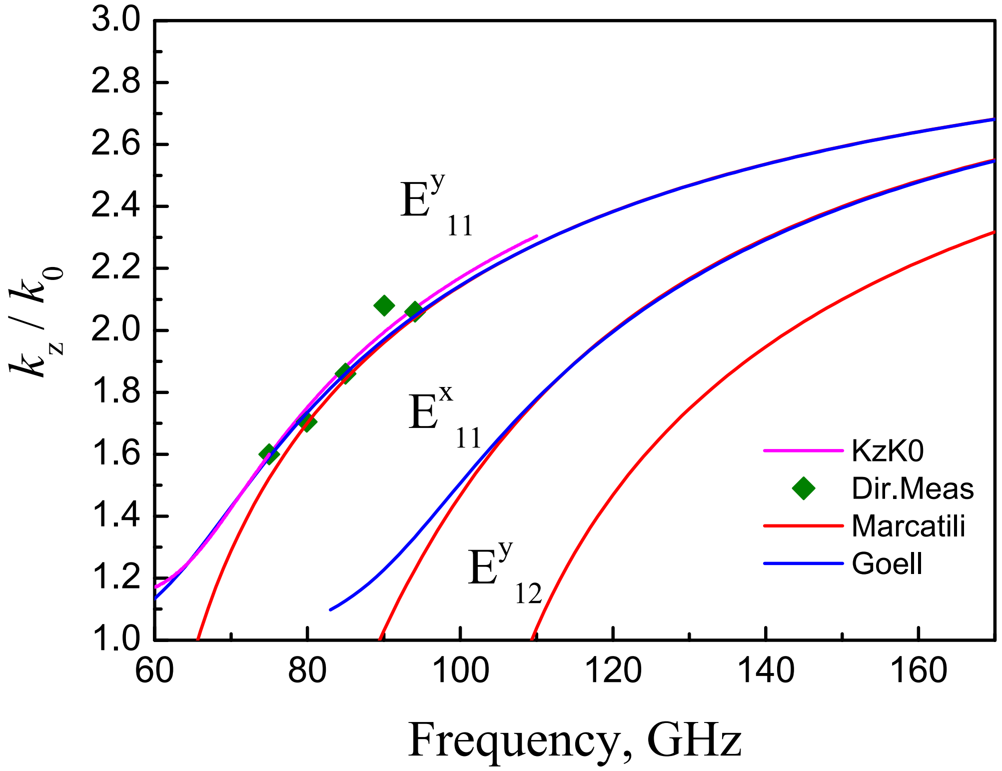

**Figure 4.7.** Comparison of $\frac{k_z}{k_0}$ calculated by Marcatili's and Goell's methods and experimental results [P4].

As to higher modes, the first of them is the $E_{12}^{y}$ mode, which is also calculated. One can see that in W-band (75-110 GHz) this mode can also exist and corrupt transmission characteristics of the DRW section. Therefore it would be useful to move it to higher frequencies while keeping the good properties of the transitions.

## 4.7. Calculation of the propagation loss

It was shown above that at high enough frequencies "Marcatili's" method works quite well in spite of its simplicity. Therefore it is attractive to calculate also the attenuation loss using this method. It turnes out that it is possible to calculate them at least for a dielectric slab waveguide.

For the rectangular cross section, let us, like in calculating the propagation characteristics, consider two dielectric slabs, horizontal and vertical ones, with corresponding thicknesses. Equations (4.15) and (4.16) can be solved also assuming that both the permittivities and $k_z$ are complex and introduce functions $F_x\left(k_z,\varepsilon_{r\perp}\right)$ and $F_y\left(k_z,\varepsilon_{r\perp},\varepsilon_{r\|}\right)$ from (4.16) and (4.15) as:

$$F_x\left(k_z,\varepsilon_{r\perp}\right)=k_x a-\pi+2\arctan\left(\frac{k_x}{k_{x3}}\right)=0\,, \tag{4.83}$$

$$F_y\left(k_z,\varepsilon_{r\perp},\varepsilon_{r\|}\right)=k_y b-\pi+2\arctan\left(\frac{1}{\varepsilon_{r\|}}\frac{k_y}{k_{y2}}\right)=0\,. \tag{4.84}$$

For the case of a very low loss tangent, as is usually the case, we can write:

$$\frac{\partial F_x}{\partial k_z}\Delta k_{z,x}+\frac{\partial F_x}{\partial \varepsilon_{r\perp}}\Delta\varepsilon_{r\perp}=0\,, \tag{4.85}$$

$$\frac{\partial F_y}{\partial k_z}\Delta k_{z,y}+\frac{\partial F_y}{\partial \varepsilon_{r\perp}}\Delta\varepsilon_{r\perp}+\frac{\partial F_y}{\partial \varepsilon_{r\|}}\Delta\varepsilon_{r\|}=0\,, \tag{4.86}$$

where $\Delta\varepsilon_{r\perp}=-j\varepsilon_{r\perp}\tan\delta_\perp$, $\Delta\varepsilon_{r\|}=-j\varepsilon_{r\|}\tan\delta_\|$, $\tan\delta_\perp$ and $\tan\delta_\|$ are the "transversal" and "longitudinal" loss tangents, respectively. The derivatives have to be taken at pure "real" solution points, found preliminarily.

Dividing both $\Delta k_{z,x}$ and $\Delta k_{z,y}$, found from (4.85) and (4.86), by the loss constant in an infinite media filled with the same dielectric, i.e. by $\alpha_0=\frac{1}{2}k_0\sqrt{\varepsilon_{r\perp}}\tan\delta_\perp$, we can find the loss factors

$\left(\frac{\alpha_x}{\alpha_0}\right)=\frac{\Delta k_{z,x}}{\alpha_0}$ and $\left(\frac{\alpha_y}{\alpha_0}\right)=\frac{\Delta k_{z,y}}{\alpha_0}$, and as the last step, multiply them:

$$\left(\frac{\alpha}{\alpha_0}\right)=\left(\frac{\alpha_x}{\alpha_0}\right)\cdot\left(\frac{\alpha_y}{\alpha_0}\right) \tag{4.87}$$

to get the final result.

# 5. HFSS simulation of different ways of DRW excitation

## 5.1. Introduction

There are three types of DRW tapering sections usually used for electromagnetic wave excitation in DRW: symmetrical (a), pyramidal (b), and nonsymmetrical (c) tapering (Fig. 5.1). In [62] a tapering section nonsymmetrical relative to the optical axis of a sapphire DRW was successfully employed. In this work these types of tapering sections were simulated by Agilent HFSS$^{TM}$ (high frequency structure simulator). We investigate them to find the most suitable of them from viewpoint of simplicity and transmission characteristics of the DRW section with such transitions [P5].

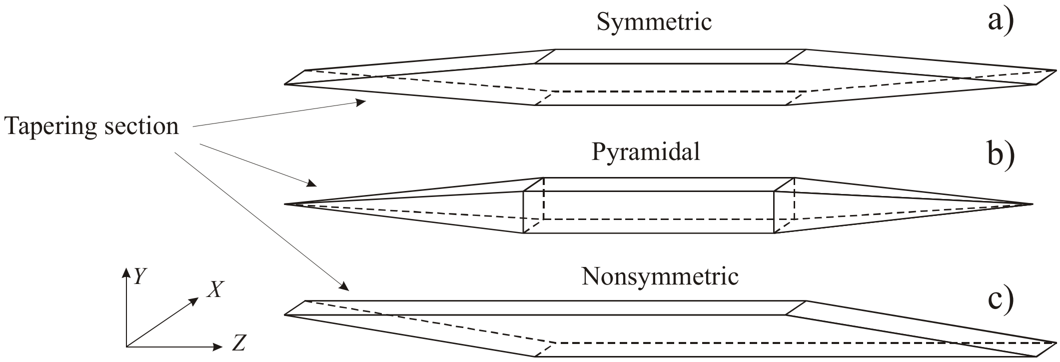

**Figure 5.1.** Three types of tapering sections: a) symmetrical; b) pyramidal and c) nonsymmetrical.

## 5.2. Simulations setup

Two polarizations can propagate in DRWs, which results in a possibility to transform from one polarization to another. One way to decrease this effect is to design the waveguide so that different polarizations have different propagation constants. Therefore the rectangular cross section was chosen rather than square. Ratio of $a : b = 2:1$ seems to be suitable [14]. The other problem is that if we increase the horizontal and/or vertical dimension of the dielectric waveguide, we can have multimode propagation, which is not desirable.

The field in the vertical (**E**) direction in the metal waveguide is concentrated stronger than in the horizontal (**H**) direction. It is well known that, in order to have a good matching, we should have the field distribution in the dielectric waveguide as close as possible to that in the metal waveguide. In DRW the larger the dimension of the dielectric waveguide is, the stronger the field is concentrated in that direction. Moreover, the $\mathbf{E}_{11}^{y}$ mode has a larger propagation constant (i.e. stronger field concentration) than that of the $\mathbf{E}_{11}^{x}$ mode. Therefore the vertical dimension of the dielectric waveguide is chosen to be larger and the wider wall to be perpendicular to that of the metal waveguide.

The rectangular cross section for the frequency range of 75-110 GHz was chosen according to recomendations in [14] ($k_0b$ = 1.7 - 1.9, $a/b$ = 0.5).

Finite Element Method (FEM) with HFSS$^{TM}$ was used to simulate *S*-parameters of the different ways of excitations of rectangular DRW with high permittivity and a low loss tangent. The types of tapers, simulated with HFSS, are shown in Fig. 5.2. Standard WR10 (2.54x1.27 mm$^2$) metal waveguides were used for the input and output. The frequency range was 75-110 GHz (W band). The material used in simulation was isotropic and had the refractive index $n$ = 3.

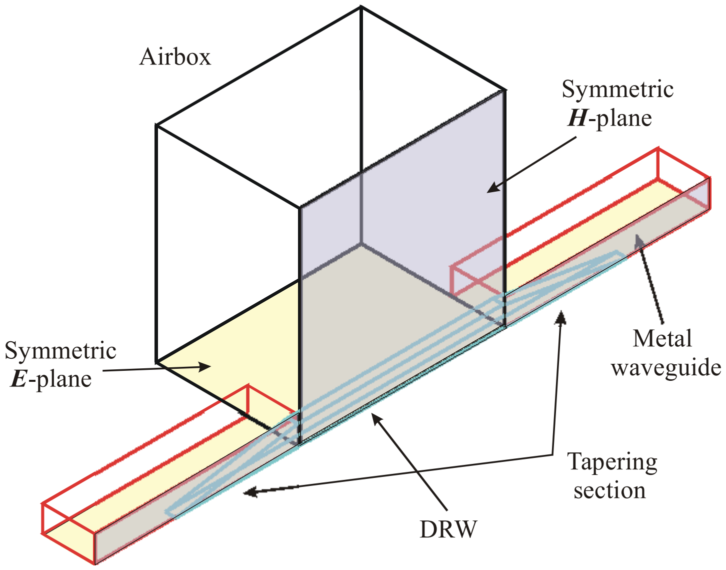

**Figure 5.2.** HFSS simulation structure.

### 5.3 Simulation of different tapering sections and cross-sections

5.3.1 Simulation of tapering in **H** and **E** planes

Tapers in **E** and **H** plane both symmetrical and nonsymmetrical were simulated (Fig. 5.3) in order to understand which type of the tapers (Fig. 5.1) is the most preferable from the viewpoint of transmission characteristics. One can see in Fig. 5.3 that there is no significant difference between symmetrical and nonsymmetrical taperings in **H**- planes, and that there is a small difference in transmission characteristics between the taperings in **H**- and **E**- planes. However, the reflections for H-tapering are higher. Also one can see that the transmission coefficient at the lower end of the frequency range is rather low, possibly because the field in the dielectric waveguide spreads out too much.

To improve the $S_{21}$ parameter we can increase a little the cross section dimensions of DRW, to 0.55 × 1.1 mm$^2$ (Fig. 5.4). The difference in transmission for **E**- and **H**- tapering characteristics becomes more significant. Therefore tapering section in **E**-plane is more preferable, and further only **E**-plane tapering section will be simulated.

### 5.3.2 Simulation of the cross section of DRW

DRWs with the same symmetrical 6 mm tapering but with cross sections of 0.9 × 0.45 mm$^2$, 0.95 × 0.475 mm$^2$, 1.0 × 0.5 mm$^2$, 1.05 × 0.525 mm$^2$, 1.1 × 0.55 mm$^2$, 1.15 × 0.575 mm$^2$ and 1.2 × 0.6 mm$^2$ were simulated (Fig. 5.5). One can see that increasing the cross section improves the characteristics at the lower frequency end, but too much increasing results in undesirable dips in $S_{21}$ characteristic, possibly due to excitation of a higher order mode. Moreover, the central frequency of the dip goes to a lower frequency with increasing the cross section. The cross sections of 1.0 × 0.5 mm$^2$, 1.05 × 0.525 mm$^2$ and 1.1 × 0.55 mm$^2$ produce the most suitable $S_{21}$ and $S_{11}$ characteristics and further only 1.0 × 0.5 mm$^2$ and 1.1 × 0.55 mm$^2$ cross-sections will be investigated.

### 5.3.3. The pyramidal tapering of DRW

The pyramidal type of tapering with different edge width of the tip *d* was simulated in HFSS (Fig. 5.6). One can see in Fig. 5.6 that there is no significant difference between the pyramidal type and the symmetrical type of tapering but technologically the symmetric tapering is easier, especially if DRW is made of a fragile material.

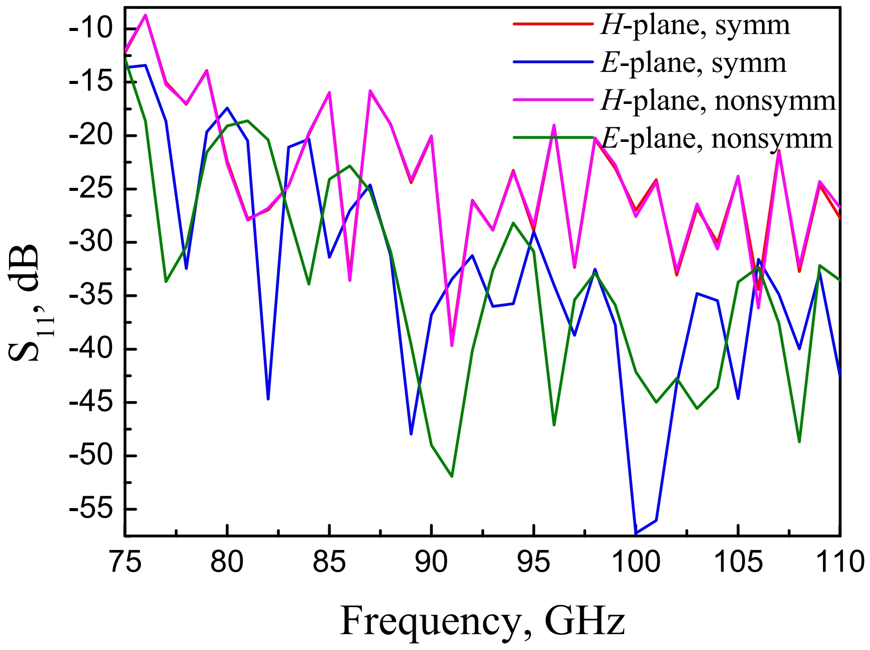

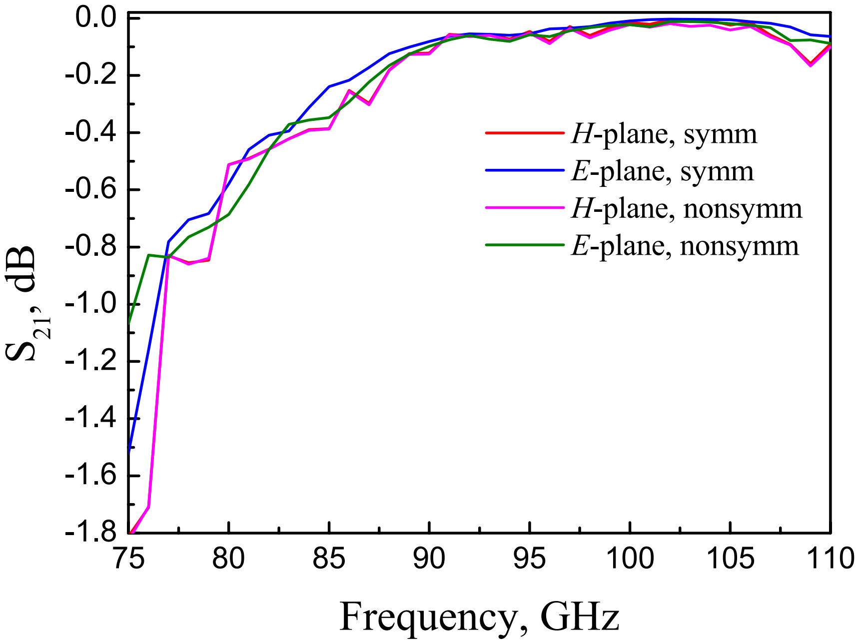

**Figure 5.3.** Simulations of symmetrical tapering in H and E planes for DRW with dimensions $1.0 \times 0.5$ mm$^2$.

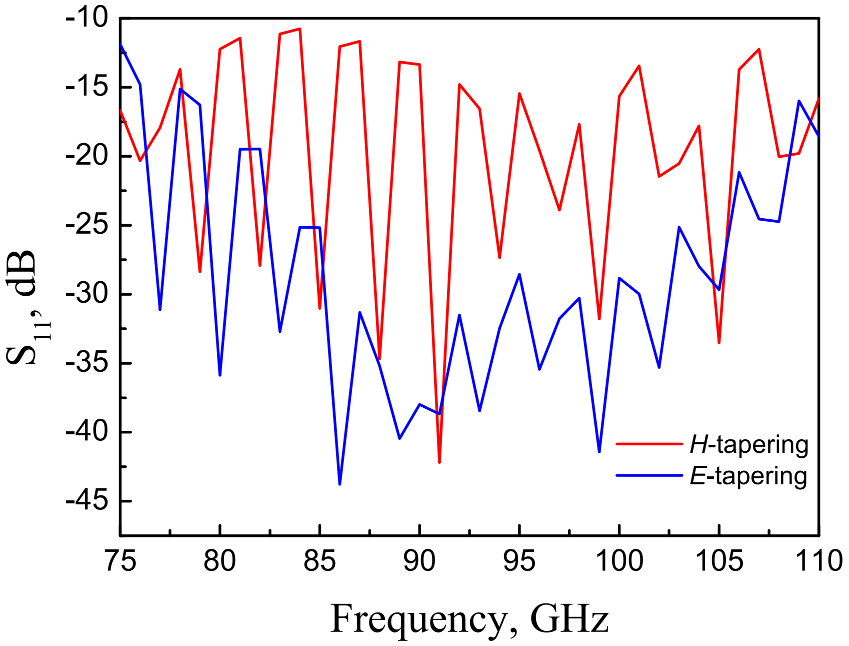

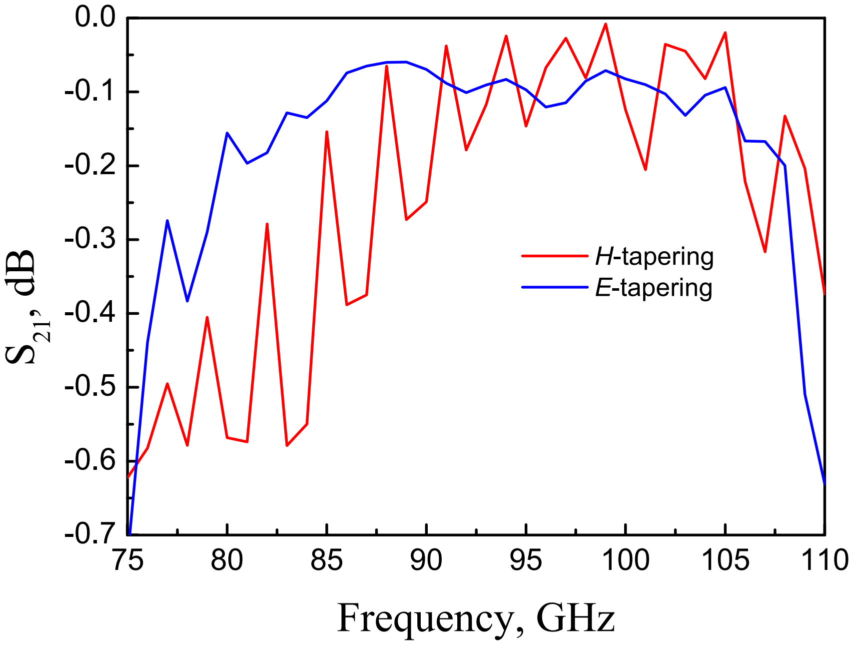

**Figure 5.4.** Simulations of symmetrical tapering in H and E planes for DRW with dimensions 1.1 × 0.55 mm$^2$.

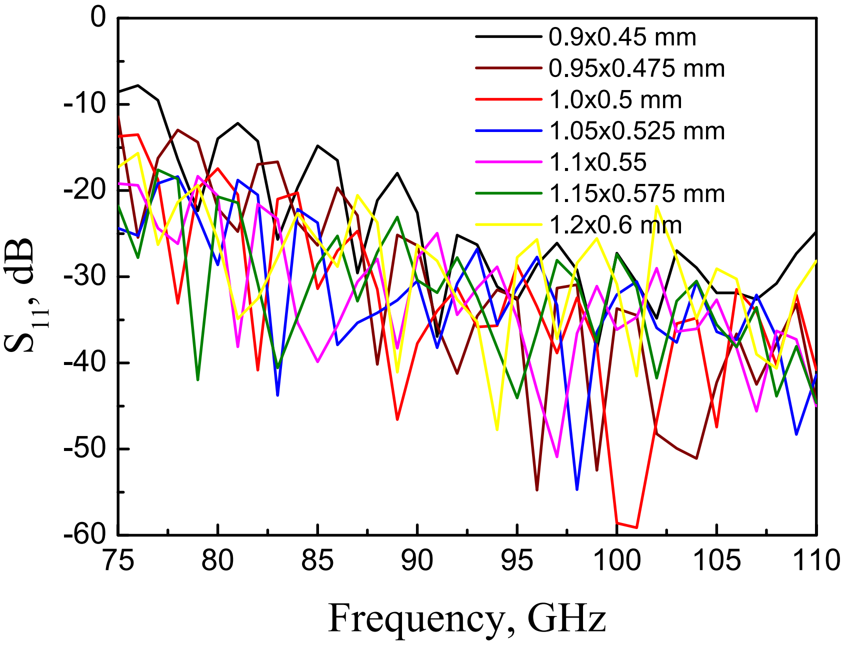

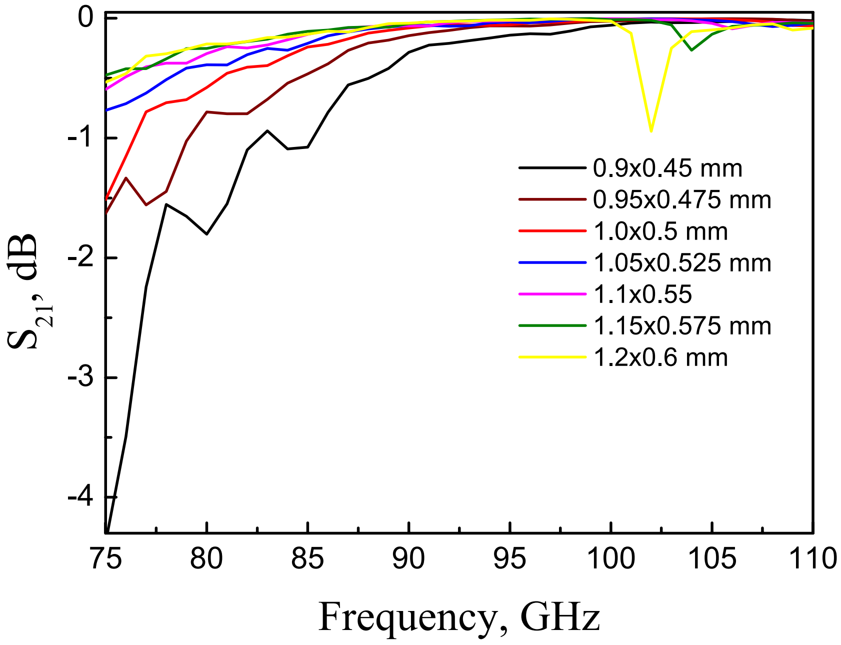

**Figure 5.5.** Simulations of different DRW cross-sections with 6 mm symmetrical tapering.

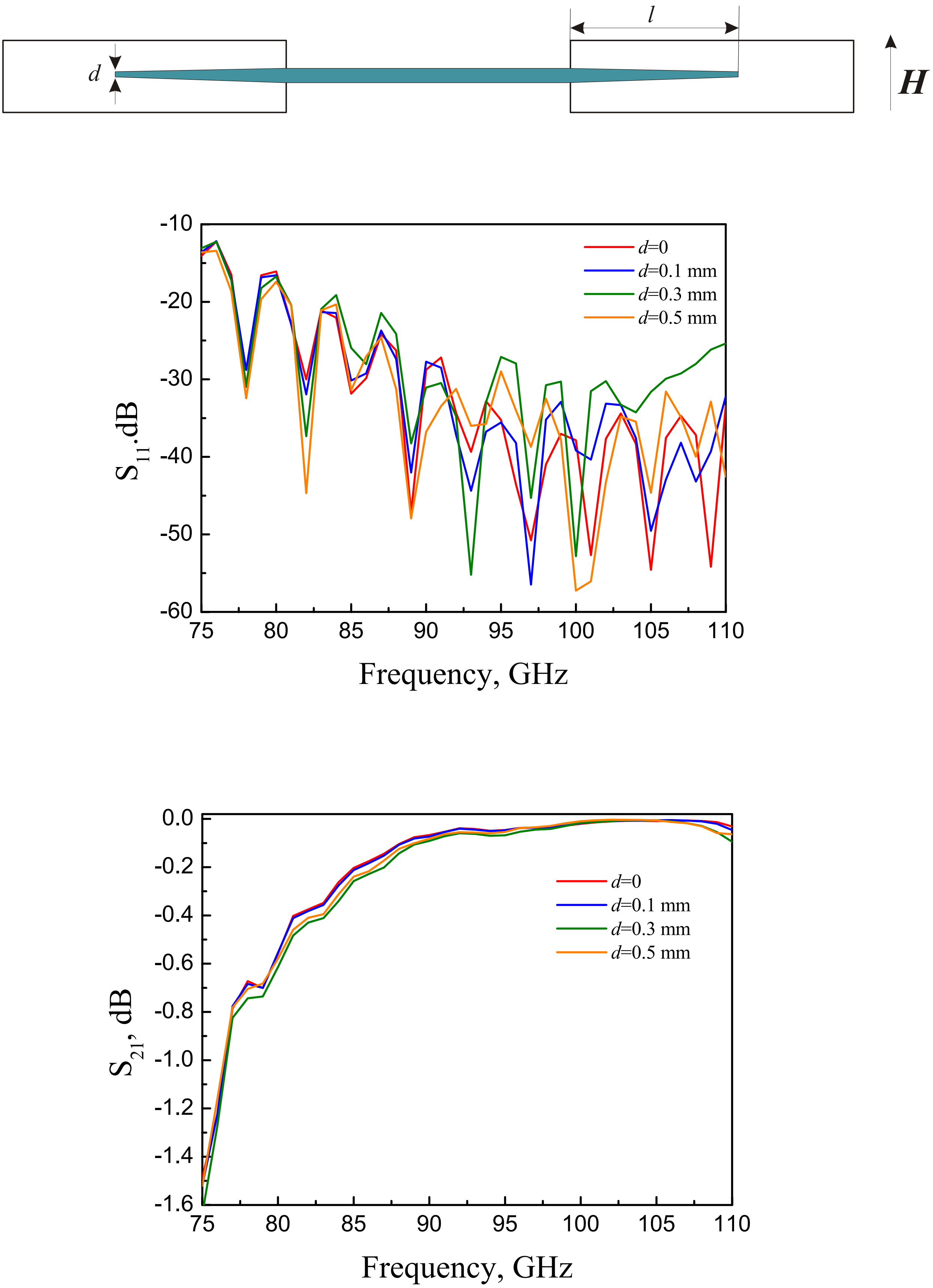

**Figure 5.6.** Simulation results of two-plane type of tapering for DRW with $1.0 \times 0.5$ mm$^2$ cross section. $d = 0$ corresponds to the pyramidal tapering, $d = 0.5$ mm – to the **E**-tapering ($l = 6$ mm).

### 5.3.4. Symmetrical tapering of DRW

The results of simulations of DRWs with dimensions 1.0x0.5 $\text{mm}^2$ and 1.1x0.55 $\text{mm}^2$, symmetrical **E**- tapering but different tapering lengths of 1-8 mm, simulated in HFSS, are shown in Fig. 5.7 and 5.8. One can see, that the tapering length less than 2 mm has a relatively high reflection and higher transition losses but 2 mm tapering is already acceptable. It even gives a better transmission coefficient at lower frequencies with the maximum approximately at 88 GHz. Increasing the tapering length only slightly improves transmission at higher frequencies and at large lengths this improvement is very small. Moreover, at 8 mm an undesirable dip appears. Technically a long tapering section is more difficult if the material is fragile, and it turns out to be unnecessary.

### 5.3.5. Nonsymmetrical tapering of DRW

Two types of nonsymmetrical excitation were simulated: 1) when the axis of the DRW is parallel to the axis of the metal waveguide, and 2) when this axis makes an angle of about 4.5° (the angle of tapering is about 9°) (Fig. 5.9). It seems that in the second case the transmission coefficient is better than in the first case because in the latter, the mode launcher (edge of the tapering) is too close to the metal wall. It can be explained. When the dielectric wedge is symmetrical, the field excited is distributed symmetrically and the wave transforms to the symmetrical $\mathbf{E}_{11}^{y}$ mode with approximately the same distribution. In the case of nonsymmetrical tapering a nonsymmetrical mode is excited in the wedge, that is, much more different field distribution and thus the transformation becomes more difficult.

The effect of different nonsymmetrical tapering lengths of 1 - 8 mm is shown in Fig. 5.10.

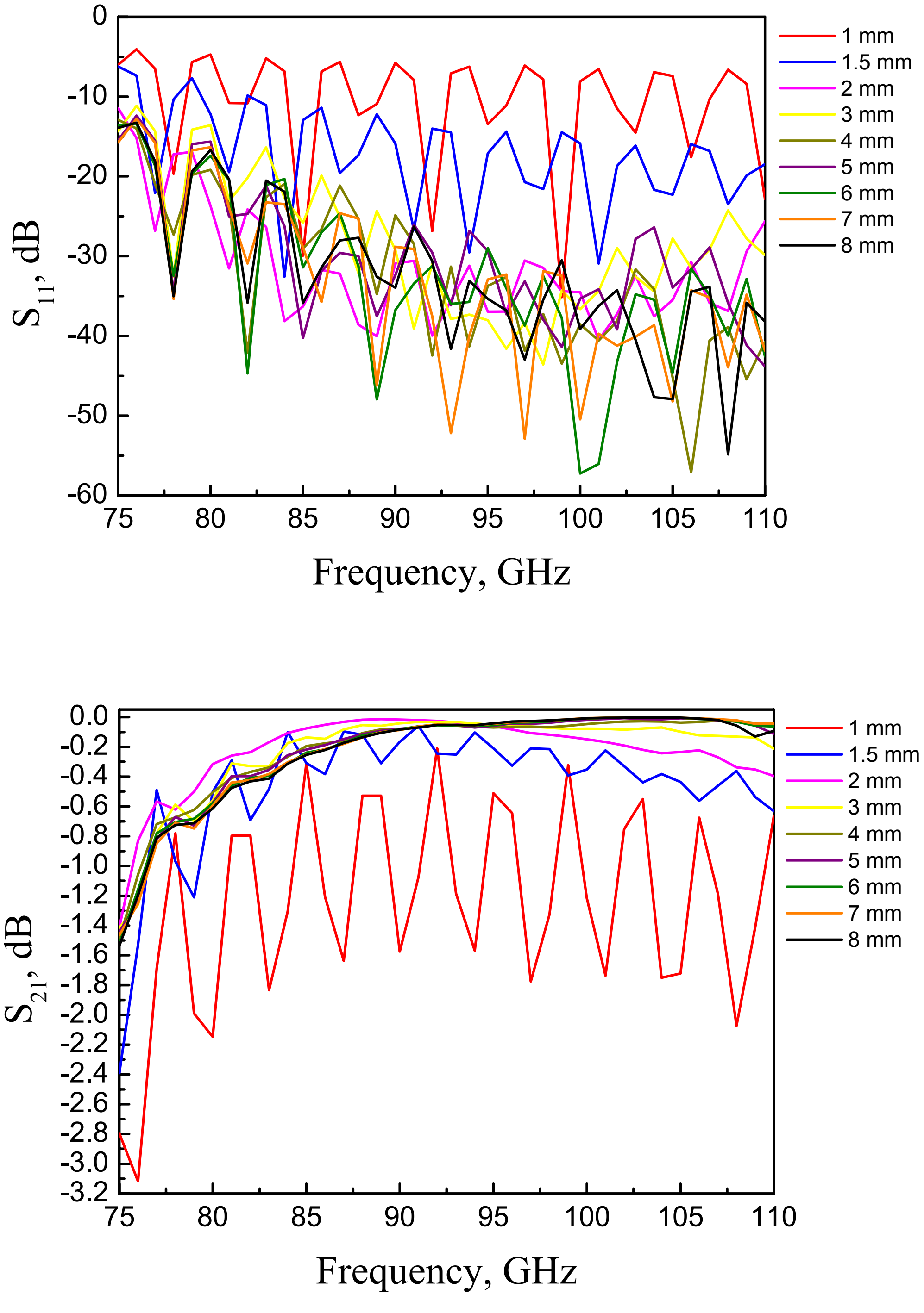

**Figure 5.7.** Simulations of symmetrically tapered DRWs of dimensions 1.0 × 0.5 mm$^2$ with different tapering lengths.

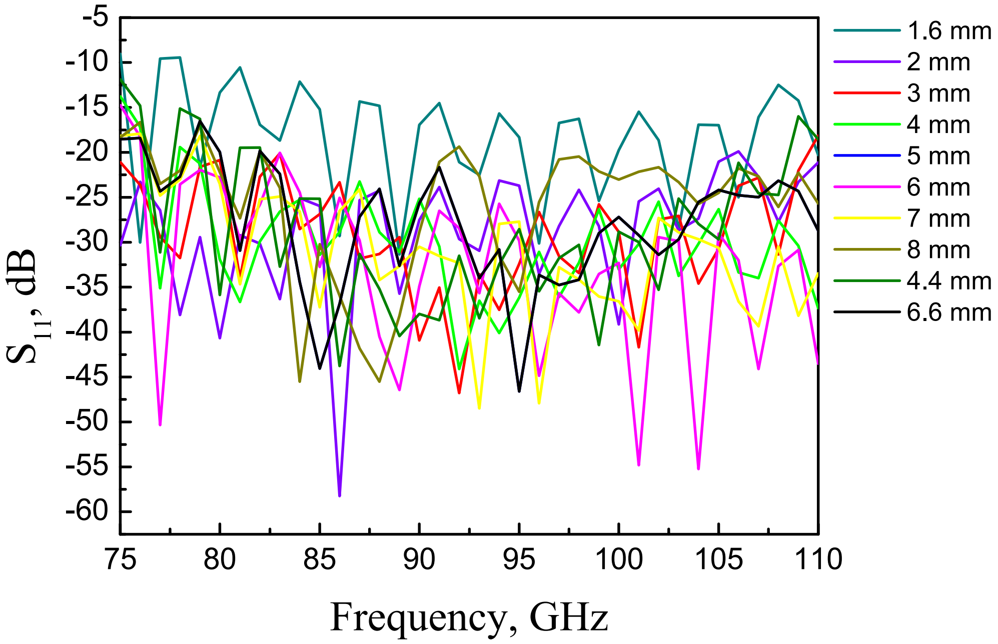

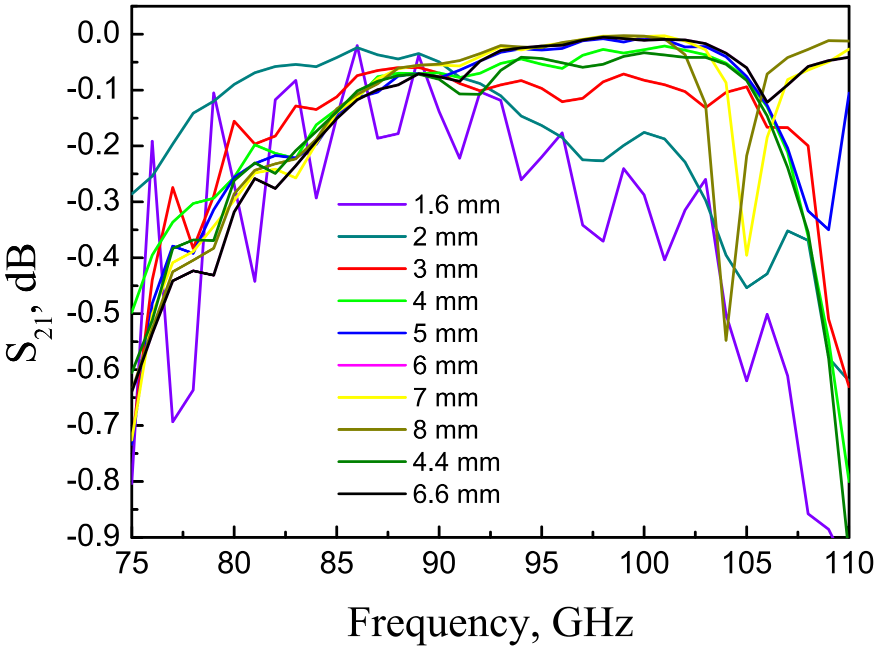

**Figure 5.8.** Simulations of symmetrically tapered DRW of 1.1 × 0.55 $mm^2$ with different tapering lengths.

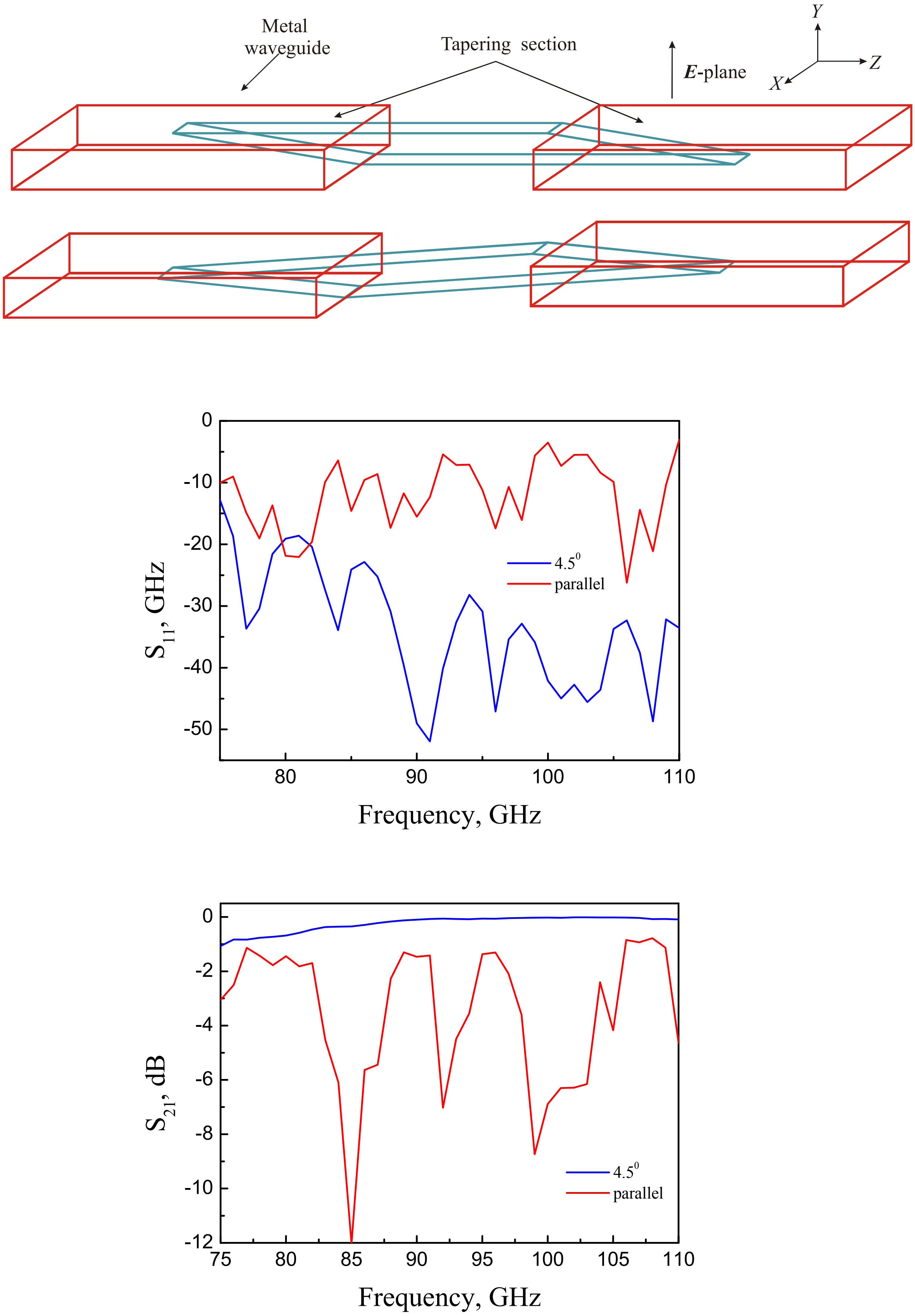

**Figure 5.9.** Simulations of nonsymmetrical tapering of a DRW with dimensions 1.1 × 0.55 $mm^2$, $l = 6$ mm.

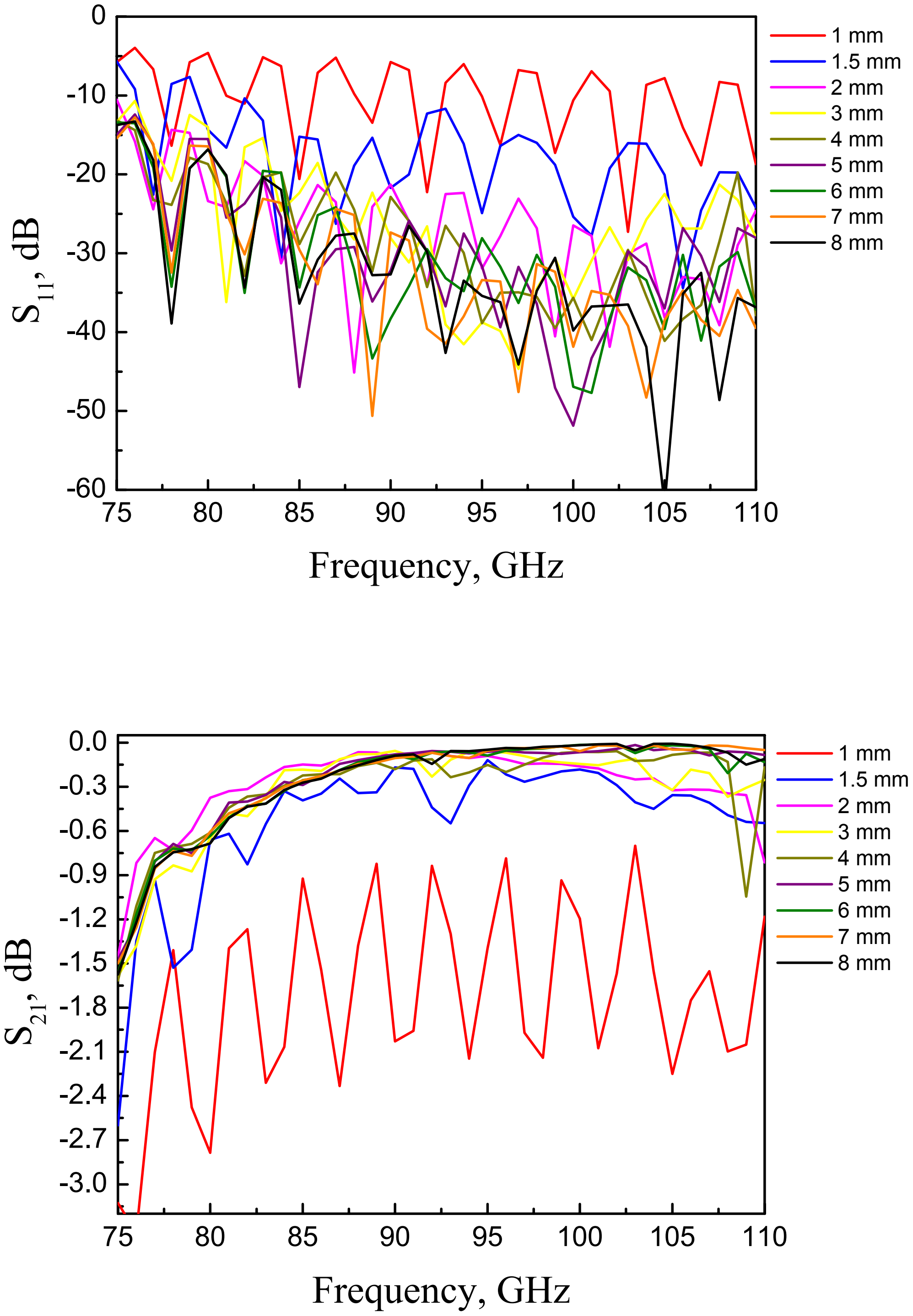

**Figure 5.10.** Simulations of DRWs with $1.0 \times 0.5$ mm$^2$ cross-section tapered nonsymmetrically with different lengths.

## 5.4. Simulation of different displacements of DRW relative to metal waveguides

Different displacement of symmetrically and nonsymmetrically tapered DRWs with cross-sections of $1.0 \times 0.5$ mm$^2$ and $1.1 \times 0.55$ mm$^2$ were simulated in order to understand the optimal position of a DRW inside the metal waveguide in terms of better transmission characteristics. The metal waveguide can have three possible displacements with respect to the DRW: along *x*-, *y*- and *z*- axes (Fig. 5.11).

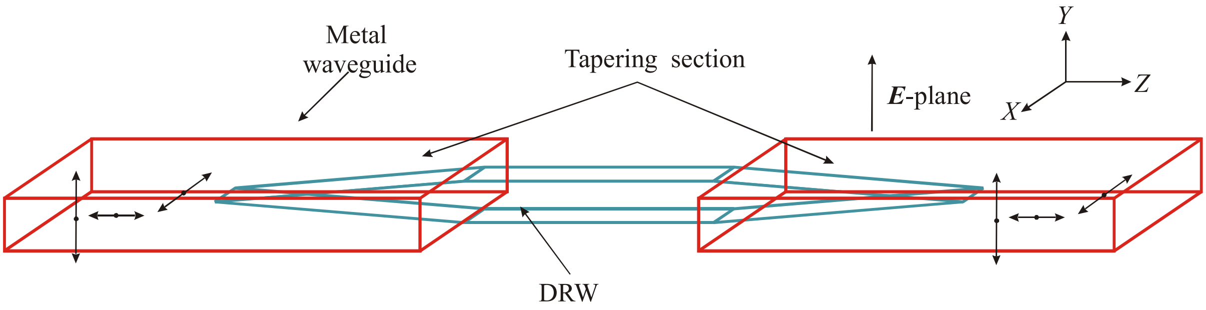

**Figure 5.11.** Displacements of a DRW.

Symmetrically tapered DRW with cross-section of $1.1 \times 0.55$ mm$^2$ was moved with respect to the metal waveguides first along the *x* axis and the results of the simulation are shown in Fig. 5.12. One can see that a small displacement (0.2 mm) can be acceptable, but further displacement drops the $S_{21}$ characteristic at the higher frequency end (Fig. 5.12).

In the case of *y*-displacement one can see that even a small displacement (0.02 mm) can results in the appearance of undesirable drops of $S_{21}$ characteristic at the low frequency end (Fig. 5.13), in contrast to *x*-displacement. Further displacement results in increasing of the drop depth and reflections, however, the reflections do not change much for displacements in either direction, thus, the main effect is an increased radiation loss.

Displacement in the *z*-direction is the most uncritical parameter, as one can see in the results in Fig. 5.14, however, the dips, that are probably due to higher order mode excitation, change their position in the frequency range.

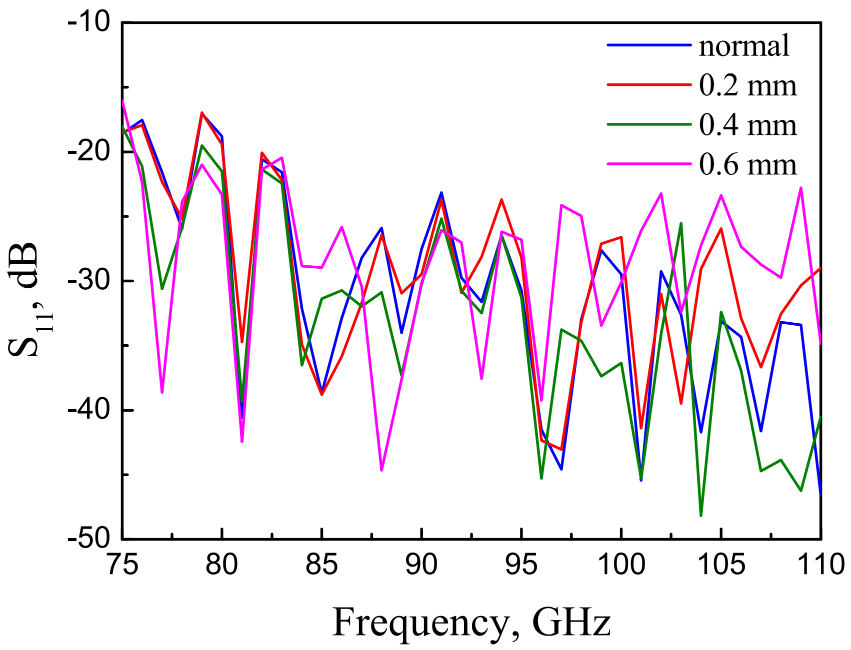

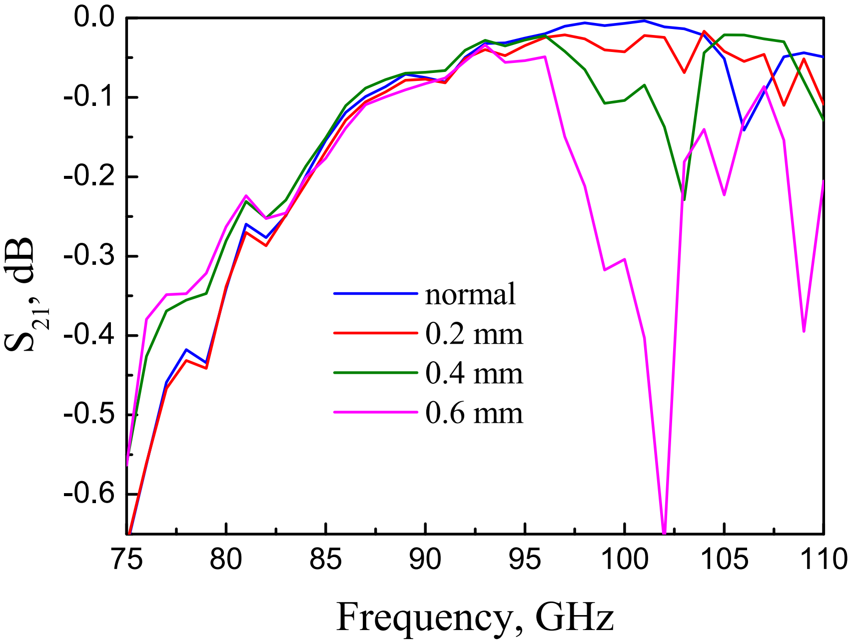

**Figure 5.12.** Simulations of *x*-displacement of a symmetrically tapered DRW with dimensions 1.1 × 0.55 mm$^2$ ($l = 6$ mm).

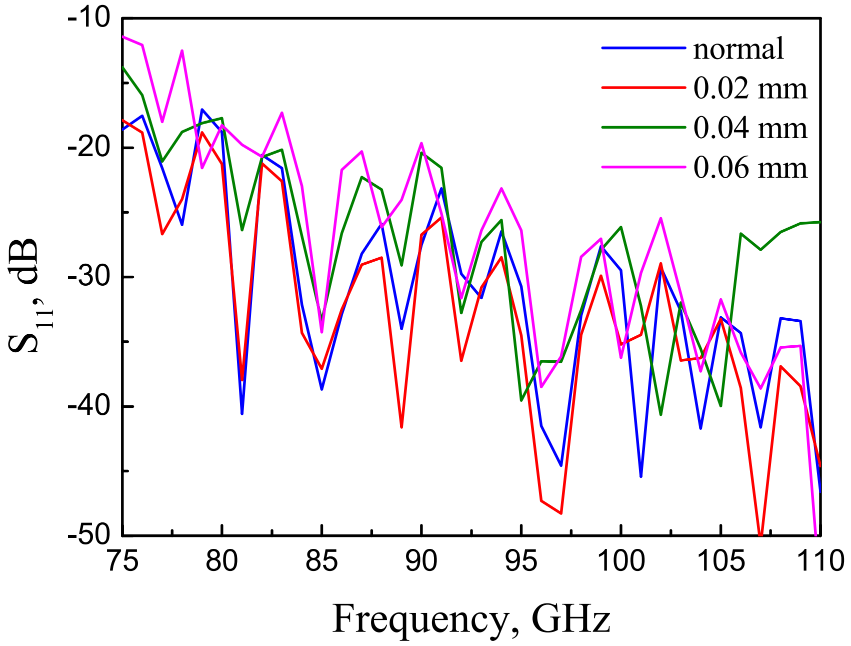

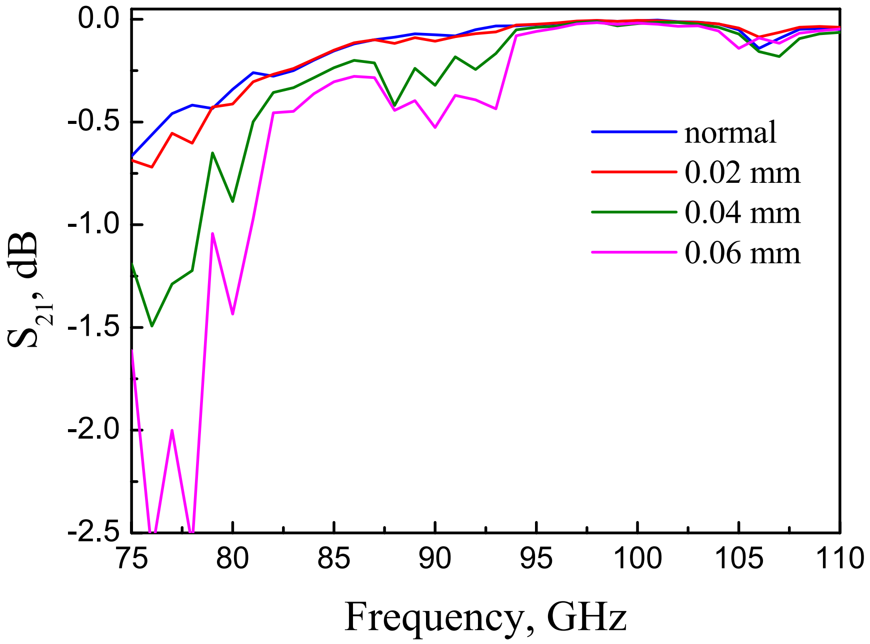

**Figure 5.13.** Simulations of y-displacement of a symmetrically tapered DRW with dimensions 1.1 × 0.55 $mm^2$ ($l$ = 6 mm).

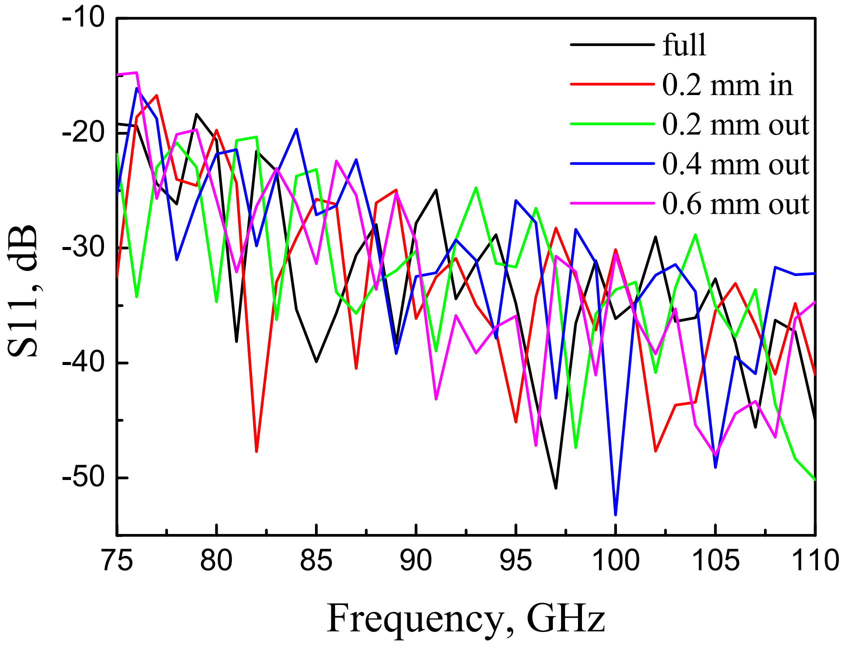

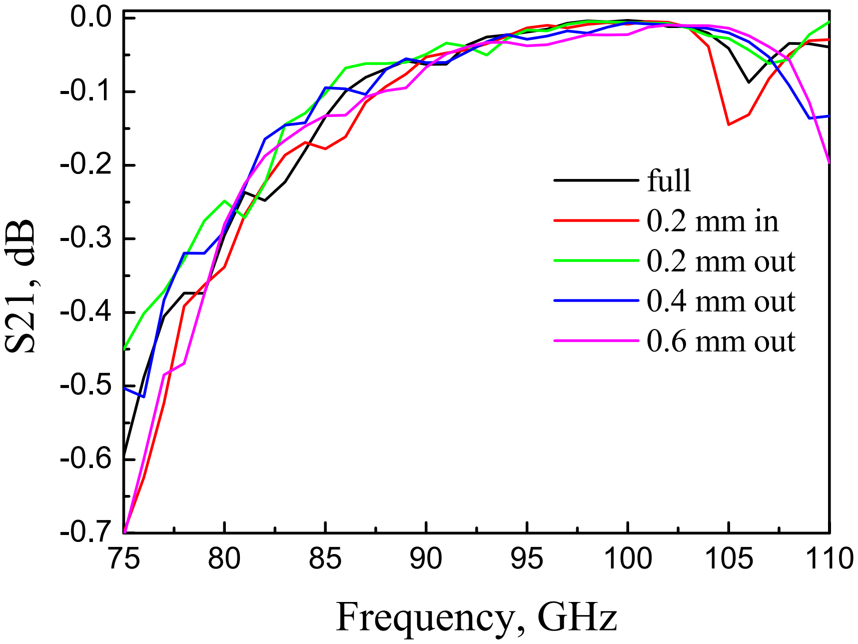

**Figure 5.14.** Simulations of *z*-displacement (longitudinal) of a symmetrically tapered DRW with dimensions 1.1 × 0.55 mm$^2$ ($l = 6$ mm).

## 5.5. Influence of the anisotropy of sapphire on the simulation results

An interesting effect is found when anisotropy of material is introduced in the simulation (Fig. 5.15). In that case a dip approximately at 105 GHz can be found that was observed also at the experiment (Chapter 6). Also, one can see that a nonsymmetrical excitation does not corrupt the characteristics significantly. Therefore we will further investigate the reasons for dips in more details in the symmetrical tapering case.

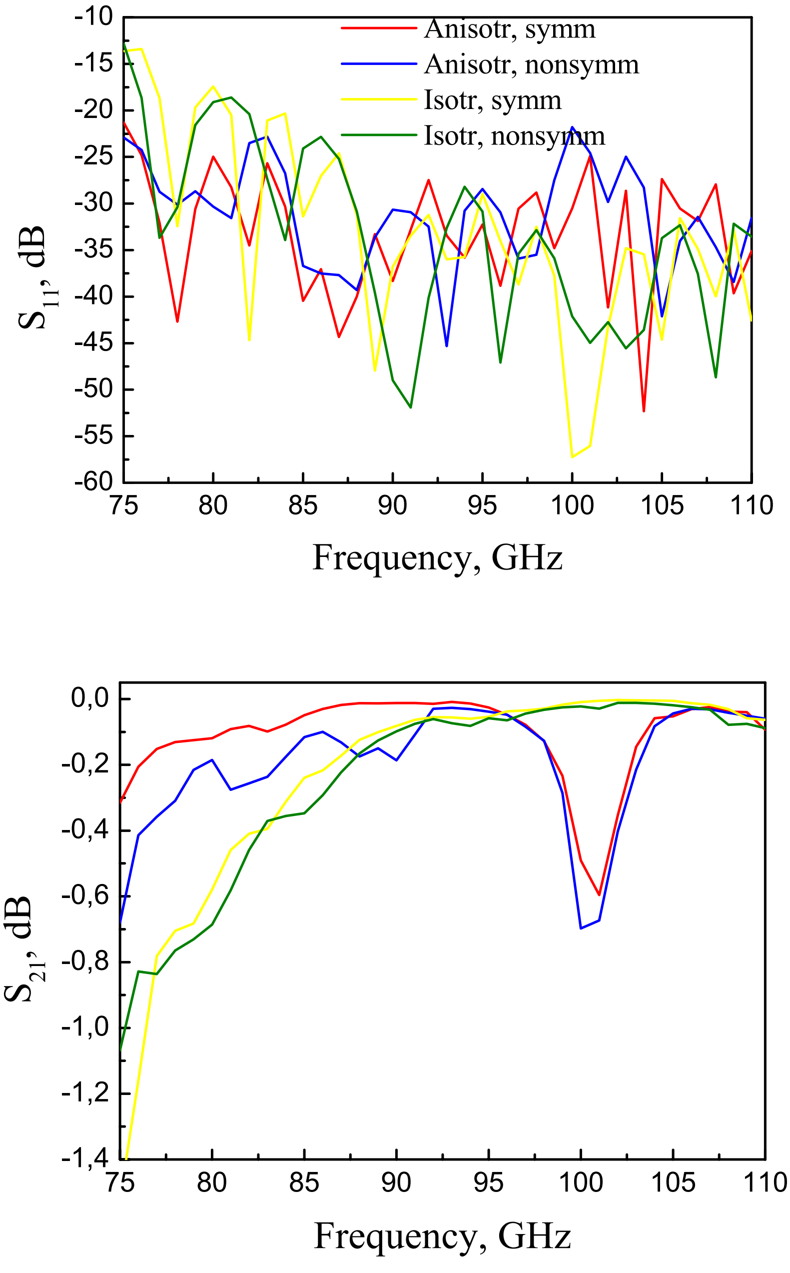

**Figure 5.15.** Influence of the anisotropy on the simulation results (*l* = 6 mm).

### 5.6. What happens in the dielectric wedge?

Let us look in more detail at the field distribution in the dielectric wedge, for example, of the sapphire dielectric waveguide. In Fig. 5.15 dependencies of insertion losses and reflections on frequency are shown for a symmetrically tapered sapphire waveguide with the cross-section of 1.0×0.5 mm$^2$ and the tapering length of 6 mm.

As one can see, there is a decrease of the $S_{21}$ parameter with decreasing frequency and a dip with the center approximately at 101 GHz.

The **E** field distribution at 75 GHz is shown in Figs. 5.16 and 5.17. According to the field distribution in the vertical (**E**) plane one can conclude that in the dielectric wedge two waves are present, “internal” and “external” ones, with different propagation constants (Fig. 5.17). One can also see that the field on the surface grows up due to concentration of the ”external wave”. On the other hand, this wave couples to the “internal wave”, therefore a maximum can be observed, there may be even several maxima, if the coupling between two waves is small. Moreover, at 75 GHz the field is weak in a rather large part of the wedge (Fig. 5.17). Thus, at lower frequencies the “external” wave is not converting to the ”internal” one fast enough.

In Fig. 5.18 one can see that several maxima are present on the surface of the wedge. One of them is at the end of the metal waveguide. That results in additional radiation to the environment.

As one can see in Fig. 5.15 the best characteristics for a sapphire waveguide section are obtained approximately at 90 GHz, therefore let us look at the field distribution at this frequency. In Fig. 5.19 one can see, that the field is concentrated stronger due to the higher frequency. Also one can find a maximum at the surface of the wedge.

In Fig. 5.20 the electrical field distribution at some moment of time is shown.

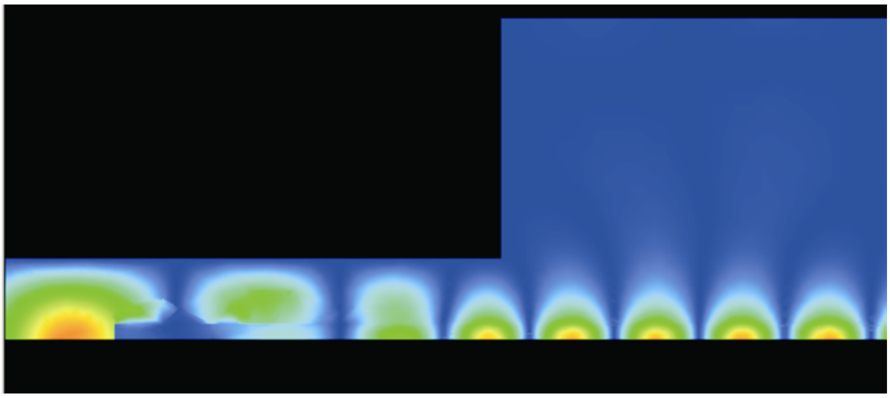

**Figure 5.16.** Electrical field in a sapphire wedge at a particular time instance at 75 GHz. Horizontal (**H**).

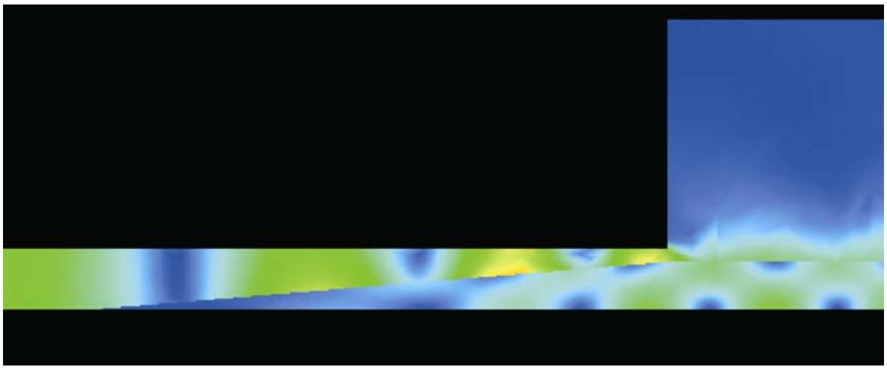

**Figure 5.17.** Electrical field in a sapphire wedge at a particular time instance. Vertical (**E**) plane, frequency 75 GHz.

**Figure 5.18.** Amplitude distribution of the electrical field in a sapphire wedge. Vertical (**E**) plane, frequency 75 GHz.

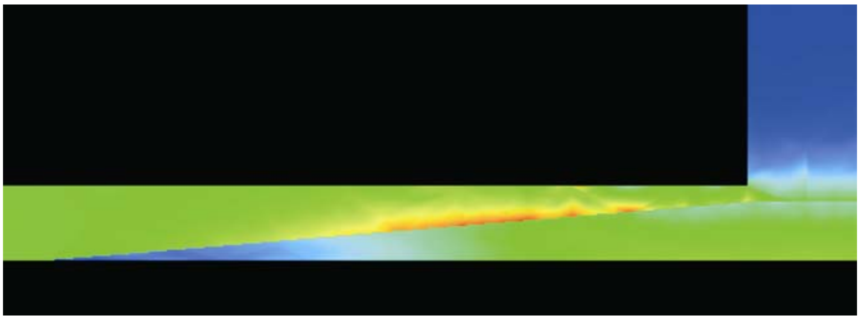

**Figure 5.19.** Amplitude distribution of the electrical field in a sapphire wedge. Vertical (**E**) plane, frequency 90 GHz.

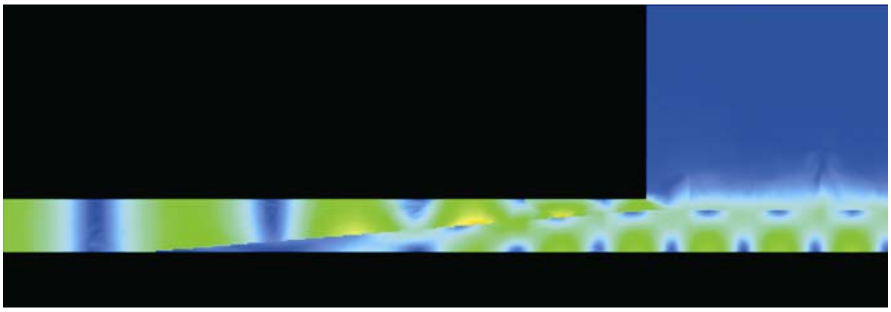

**Figure 5.20.** Electrical field distribution in a sapphire wedge at a particular time instance. Vertical (**E**) plane, frequency 90 GHz.

The case of 101 GHz is more interesting. At 101 GHz (Figs. 5.21-5.23) one can see the following. The “external” wave is gradually converting to the ”internal” one, but the phase difference between these waves increases. As a result at a particular place the converted wave will be in counterphase with the ”internal” wave, that is, the “internal” wave is converting to the “external” one (Fig. 5.21) and radiating to the environment. Thus, at 101 GHz one can see a dip in the $S_{21}$ characteristic.

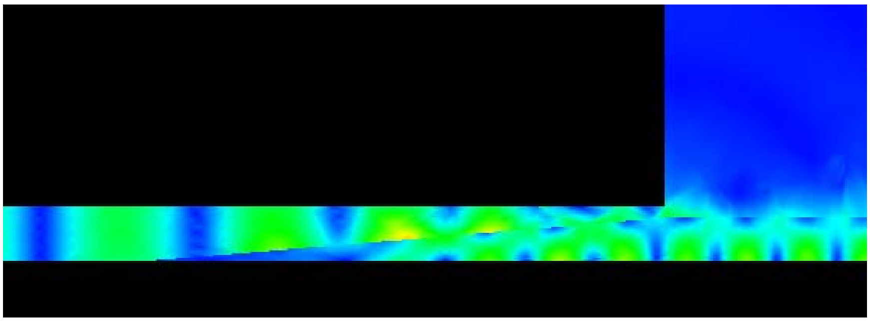

**Figure 5.21.** Electrical field distribution in a sapphire wedge at a particular time instance. Vertical (**E**) plane, frequency 101 GHz.

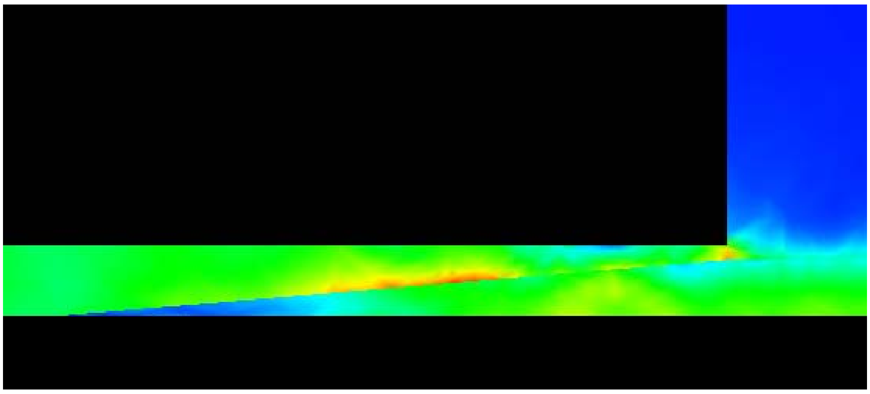

**Figure 5.22.** Amplitude distribution of the electrical field in a sapphire wedge. Vertical (**E**) plane, frequency 101 GHz.

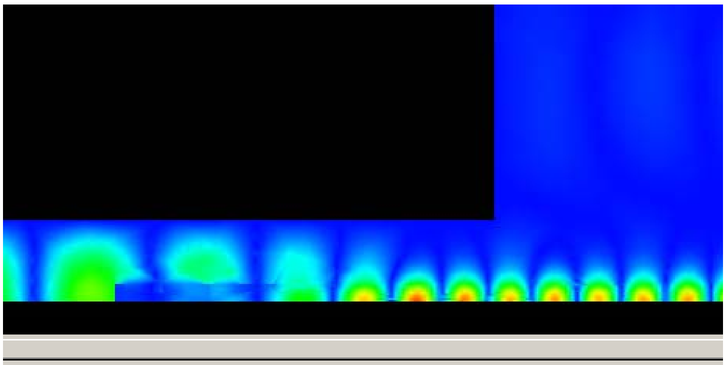

**Figure 5.23.** Electrical field distribution in a sapphire wedge at a particular time instance. Horizontal (**H**) plane, frequency 101 GHz.

Thus, at 101 GHz the main mechanism of losses is the convertion of the ”internal” wave to the ”external” one followed by the radiation to the environment. That is, the phase difference between the ”internal” and ”external” waves should not change very much.

## 5.7. Influence of the quality of the tapering tip

Two sapphire waveguide sections with 6 mm tapers (Fig. 5.24) were simulated and the results are shown in Fig. 5.25.

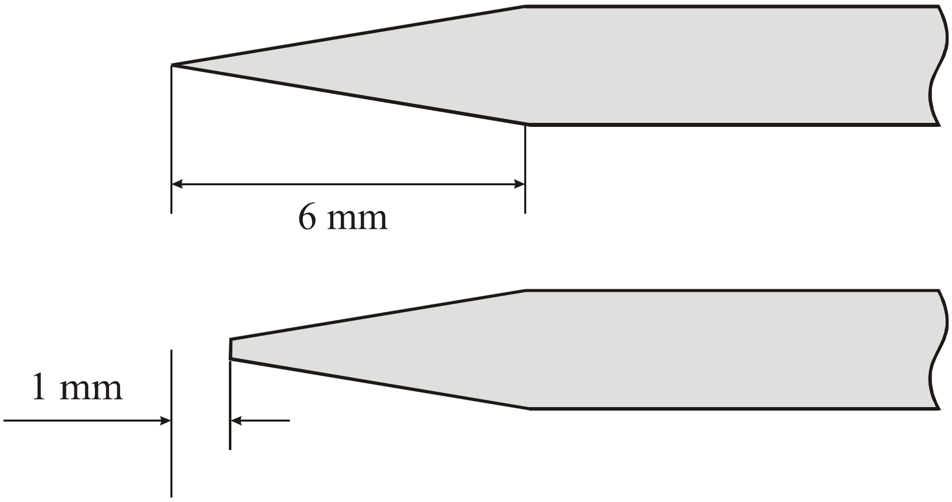

**Figure 5.24.** Two tapers simulated (with and without cleaving).

As one can see, the 1 mm cleaving increases strongly the reflection but does not change considerably the $S_{21}$ characteristic.

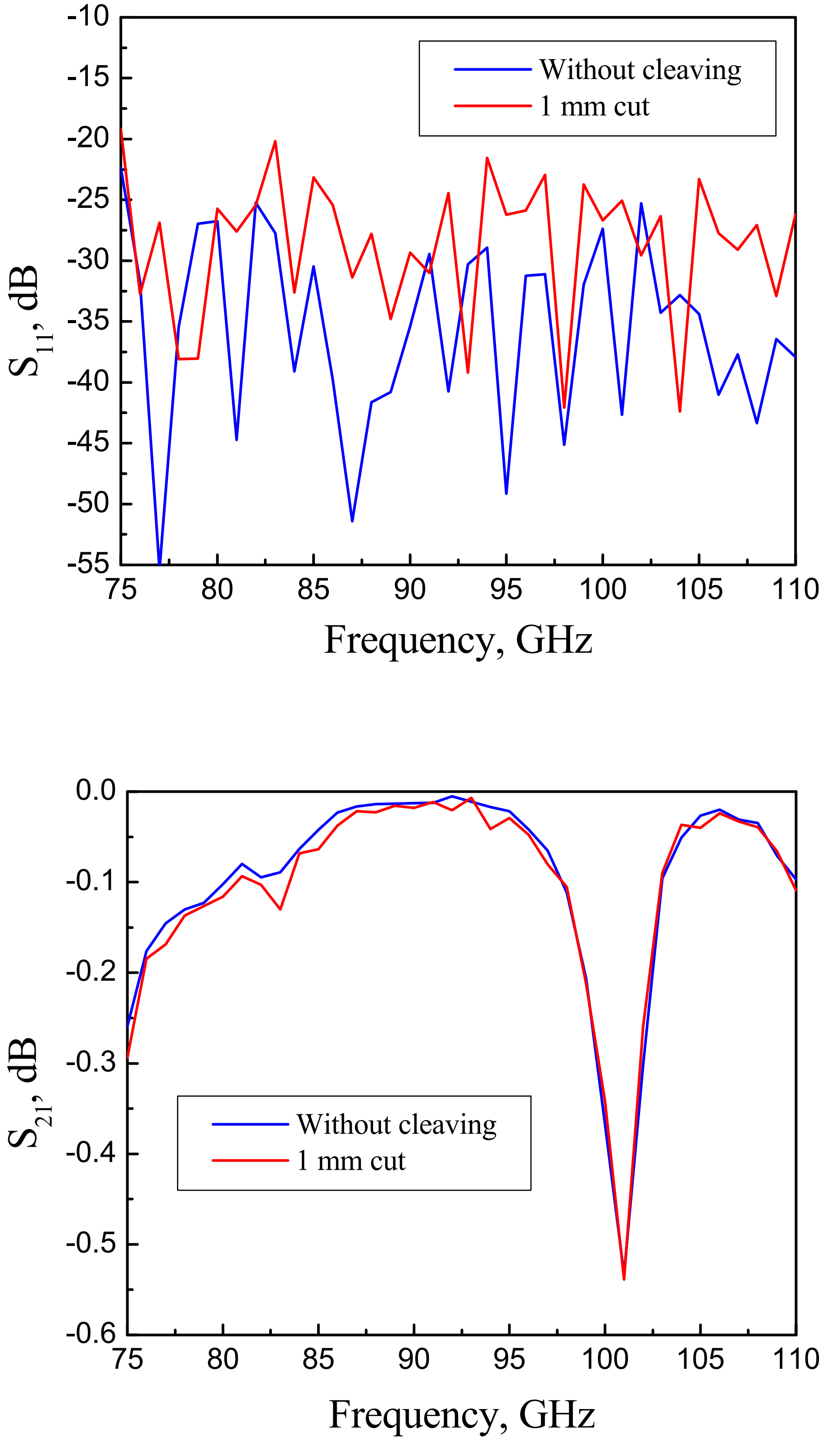

**Figure 5.25.** Simulation results of simulation of a tapered sapphire waveguide with and without 1 mm cleaving.

### 5.8. Conclusions

Different types of transitions from a metal waveguide to DRW and ways of excitation were simulated with HFSS. It was found that:

- The tapering has to be in the **E**- plane.
- The cross-section of DRW determines the frequency range. The most suitable cross-sections for 75-110 GHz, $n = 3.0$ are $1.0 \times 0.5$ mm$^2$, $1.05 \times 0.525$ mm$^2$ and $1.1 \times 0.55$ mm$^2$.
- There is no reason to use the pyramidal tapering as it is much more complicated to manufacture.
- The length of the tapering section has to be longer than 2 mm, but too long taperings are complicated to manufacture and are unnecessary.
- A nonsymmetrical tapered DRW should be excited so that the tip is positioned in the middle of the metal waveguide.
- The optimal position of a symmetrical DRW is where the axes of both the DRW and the metal waveguide coincide.

The DRW is not very sensitive to the position with respect to the metal one, except in the vertical direction.

# 6. Low loss sapphire and GaAs DRW for 75-110 GHz frequency band

## 6.1. Introduction

High resistivity Si (> 10 kΩ), semi-insulated GaAs ($n \sim 10^8$), fused sapphire, BN, ferrites and other materials with $\tan\delta \leq 10^{-4}$ are widely used as materials for DRWs. Rectangular DRWs have lower propagation losses if made of e.g. monocrystalline material with a small loss. They have a broader operation frequency bandwidth in comparison with the standard single mode metal waveguides, but matching of a DRW to a metal waveguide (i.e. transition) is a remaining problem [P5].

## 6.2. Experiment

The sapphire DRWs were made of monocrystalline sapphire cut along the optical axis. Cross-section of $1.0 \times 0.5$ mm$^2$ and 6 mm tapered length were chosen for the frequency range of 75-110 GHz according to the HFSS simulation. The tapering section was chosen to be nonsymmetrical because of easier and less expensive fabrication. The length of the tapered section was 6 mm so that the angle of the tapering was about 9°. Four samples with 47 mm length and four samples with 110 mm length were measured, all with a $1.0 \times 0.5$ mm$^2$ cross-section.

GaAs DRWs oriented along the [110] direction were cut from semi-insulating (100) GaAs wafer with electron concentration $n \sim 10^8$ cm$^{-3}$, $\tan\delta \sim 3\cdot10^{-4}$ and $\varepsilon \sim 13.3$. The DRWs were only cut without polishing, therefore the tapered sections are not perfect and may have small defects in shape. The GaAs DRW samples are described in Table 6.1.

Table 6.1. GaAs DRW sample description

| | **Cross-section** | **Total length of DRW** | **Tapering** |
|---|---|---|---|
| GaAs DRW 1 | $1.04 \times 0.51$ mm$^2$ | 45 mm | 6 mm symmetrical |
| GaAs DRW 2 | $1.01 \times 0.51$ mm$^2$ | 45 mm | 6 mm nonsymmetrical |
| GaAs DRW 3 | $1.43 \times 0.51$ mm$^2$ | 49 mm | 8 mm symmetrical |
| GaAs DRW 4 | $1.43 \times 0.51$ mm$^2$ | 48 mm | 8 mm nonsymmetrical |

The plane of tapering was chosen to be in the *E*-plane of the metal waveguide according to HFSS simulations. The DRW was supported by a styrofoam holder. The transition from the standard metal waveguide to the dielectric one and vice versa is shown in Fig. 6.1. A Vector Network Analyzer HP 8510 was used to measure the *S*-parameter characteristics.

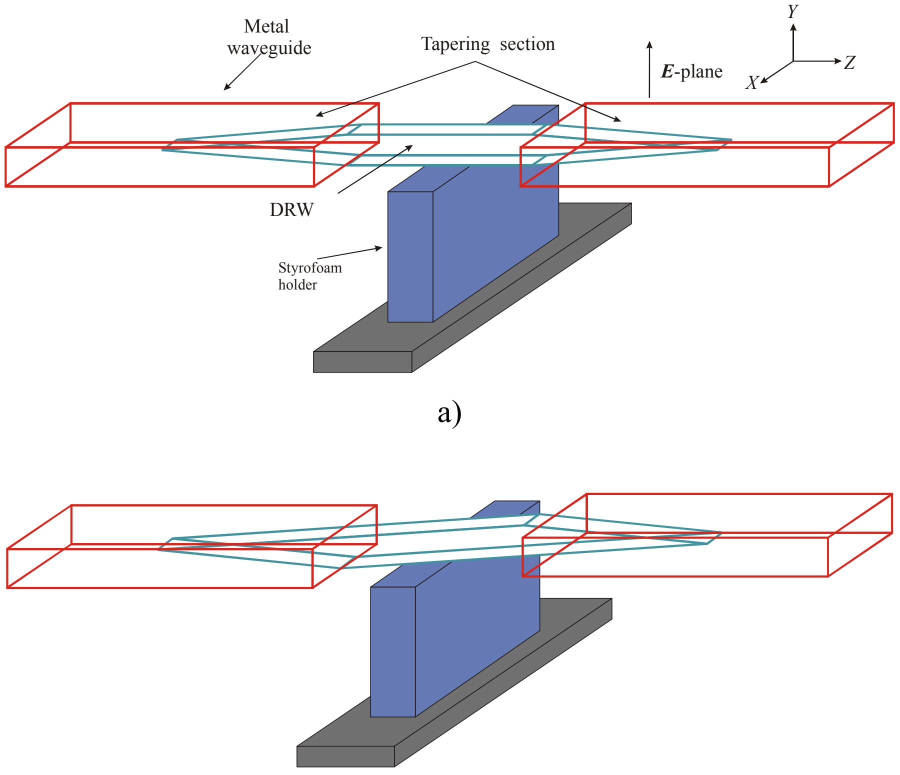

a)

b)

**Figure 6.1.** Experimental set-up of the transition from a metal waveguide to DRW: a) a symmetrical case, b) a nonsymmetrical case. The metal waveguides are connected to VNA.

Sapphire DRW measurements

The insertion losses of four 47 mm and four 110 mm sapphire waveguides (nonsymmetrical tapering in both cases, see Fig. 6.1b) are presented in Figs. 6.2 and 6.3, respectively. It can be seen that the 47 mm sapphire DRW has an insertion loss of 0.1-0.3 dB at frequencies 77-98 GHz (samples 1, 2). One can see that from the frequency 98 GHz upwards the losses increase and reach the maximum at 105 GHz. Such undesirable corruption of the characteristics can be explained by difficulties of the excitation occurring due to nonidealities in the tapering sections and due to a possible excitation of higher order modes. The differences in $S_{21}$ and $S_{11}$ curves (Figs. 6.2 and 6.3) of sapphire DRWs are due to the dissimilarities of the DRWs.

A typical voltage standing wave ratio (VSWR) for 47 mm and 110 mm sapphire DRWs with two transitions is shown in Fig. 6.4. The maximum value of VSWR for two transitions is 1.23 (1.13

for one transition), which corresponds to 0.07 dB loss. At the lower frequency end the insertion losses are higher, and by analyzing Figs. 6.2 and 6.3 one can say that the radiation loss is the dominant factor at the lower frequency end. In the middle band, however, absorption loss is the main factor. The ripple of the VSWR characteristics is caused by the interference between the two ends of the DRW.

An interesting effect was observed when the reflection was measured with one end of the DRW free (Fig. 6.5). Removing the receiving metal waveguide results in an increase of the reflection coefficient approximately by 10 dB. This means that while such a structure results in a well matched dielectric rod antenna, the antenna is not as well matched to free space as DRW is matched to another metal waveguide.

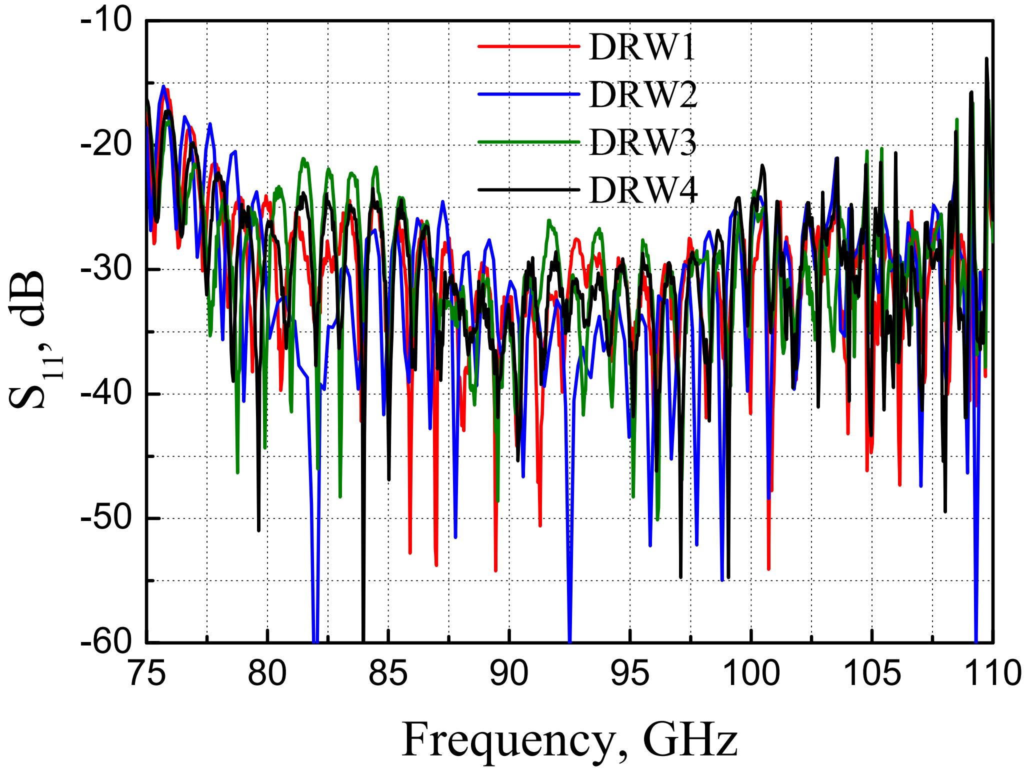

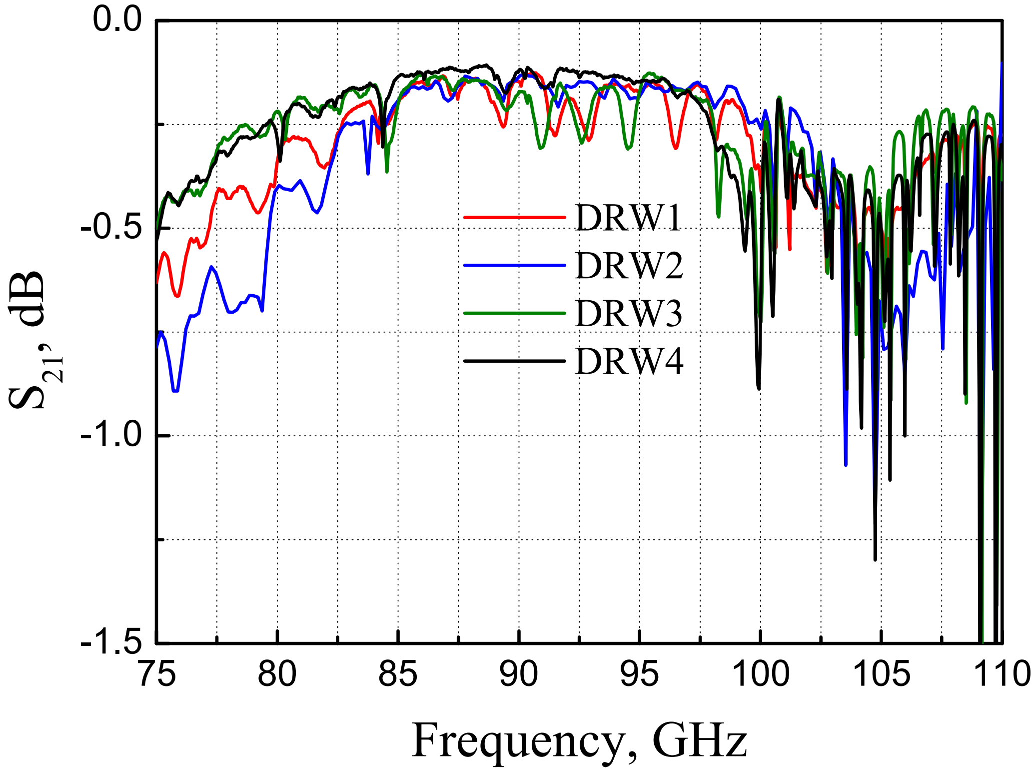

**Figure 6.2.** Measurements of 47 mm sapphire DRWs.

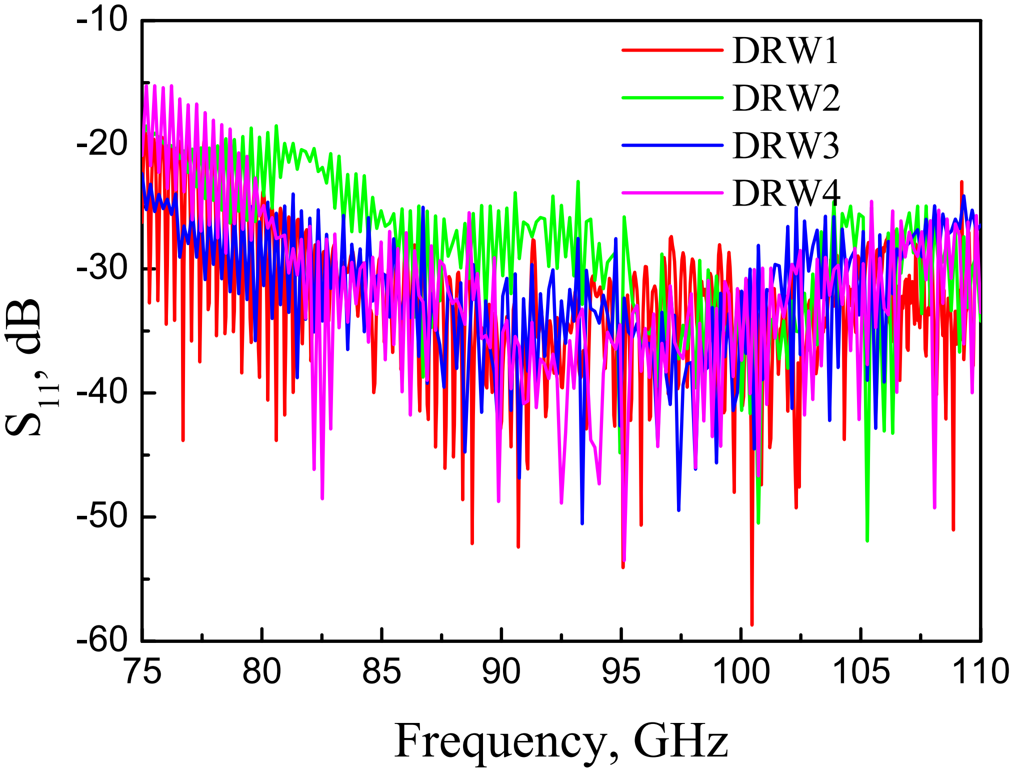

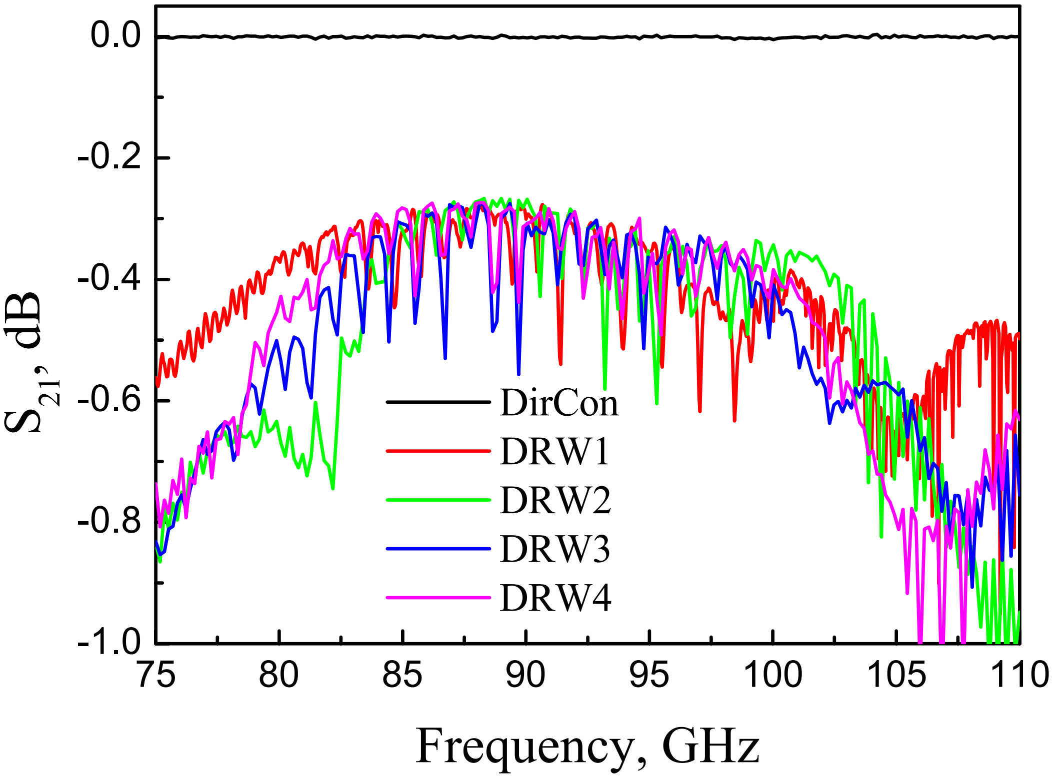

**Figure 6.3.** Measurements of 110 mm sapphire DRW. DirCon means a direct connection between the two metal waveguides.

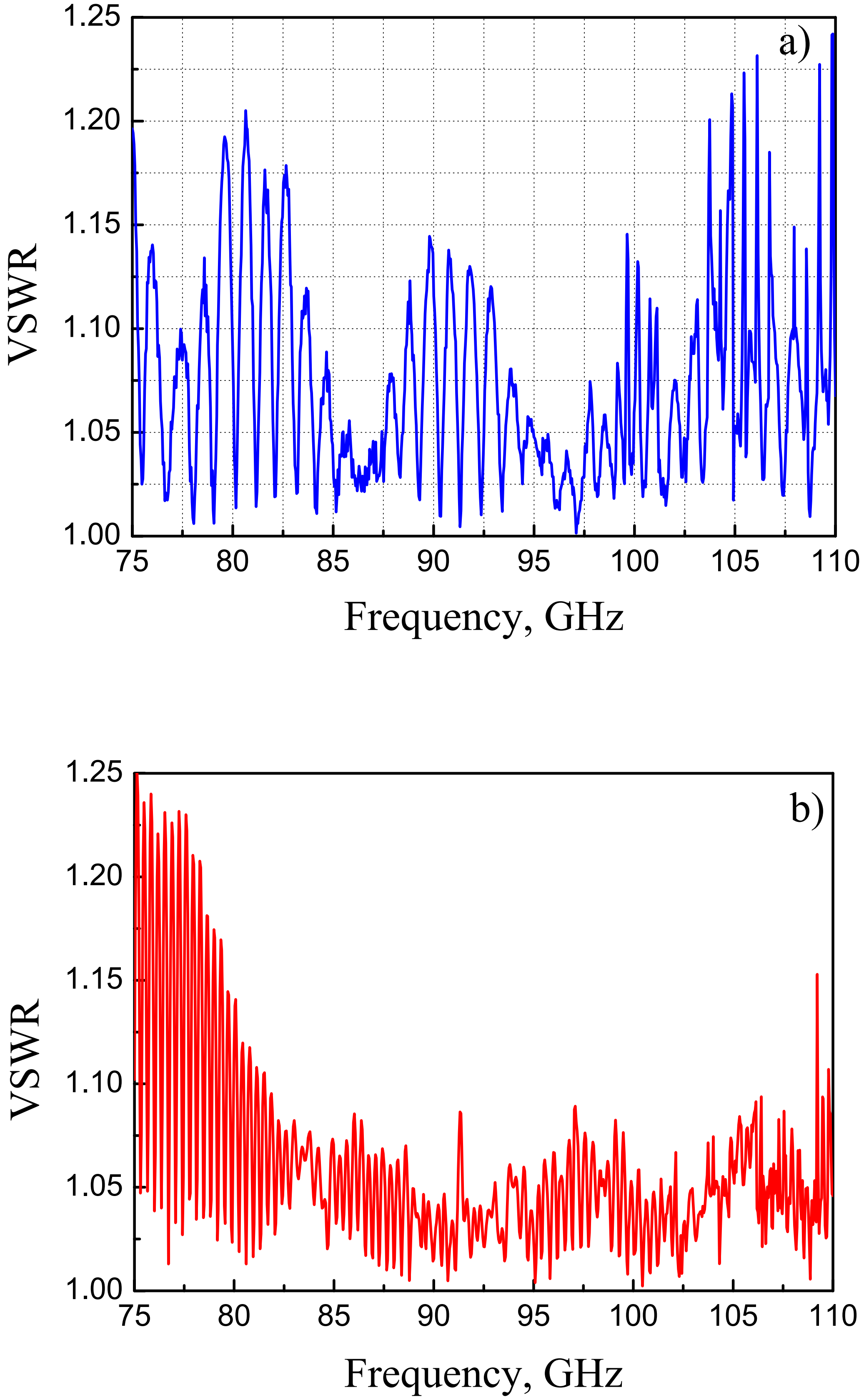

**Figure 6.4.** VSWR of a) a 47 mm and b)a 110 mm sapphire DRW.

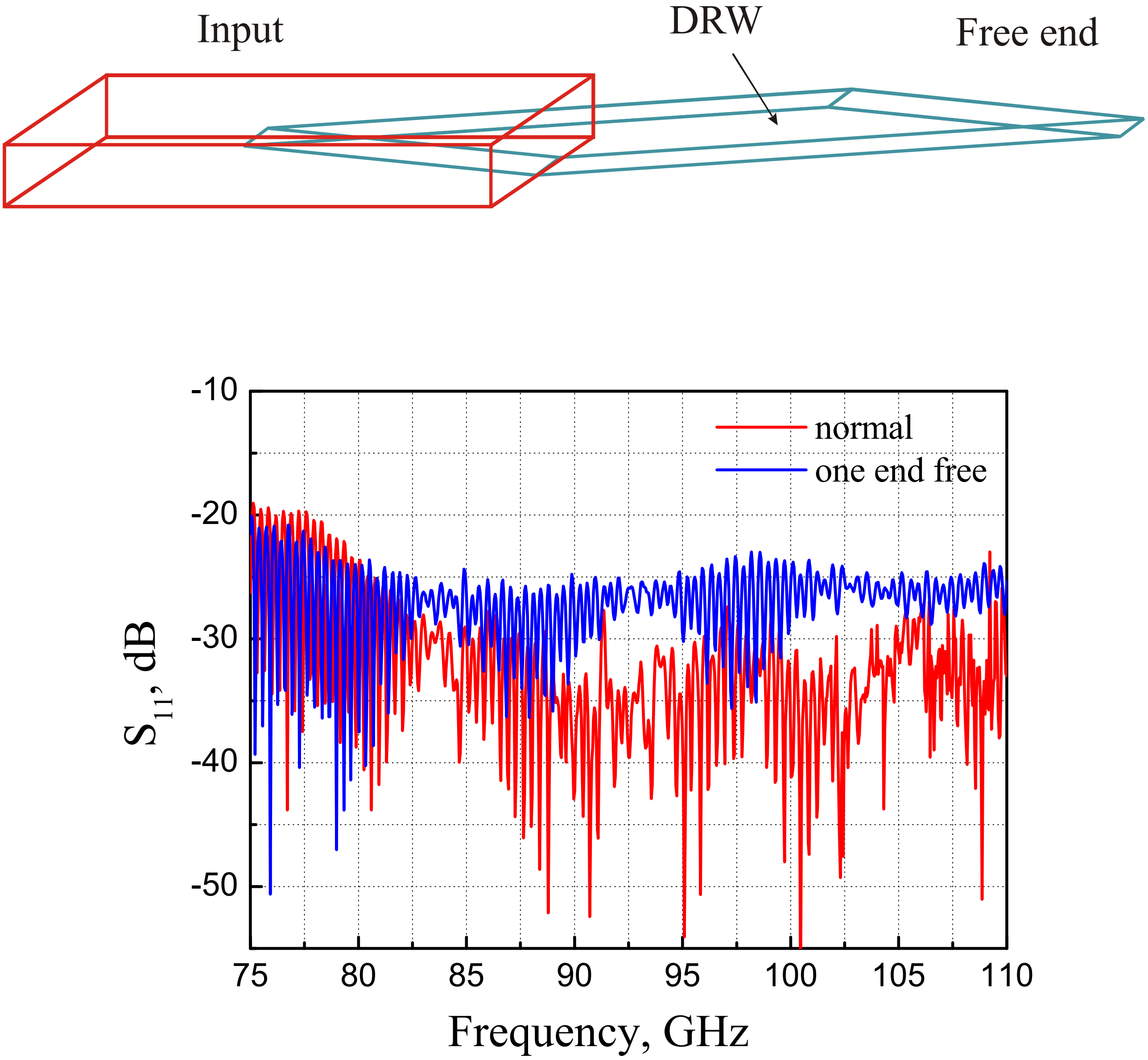

**Figure 6.5**. Measurement of DRW with one end free.

GaAs DRW measurements

Four different GaAs DRW samples of length 45-49 mm were measured (Fig. 6.6). The typical value of $S_{21}$ is approximately 0.4-0.5 dB, while $S_{11}$ is mainly below 30 dB. One can see that nonsymmetrical tapered DRWs have worse characteristics at both ends of the frequency range. DRWs with larger vertical dimensions (~1.5 × 0.5 mm$^2$ and 8 mm tapering) have also suitable characteristics. The reflections are lower than for sapphire DRW. The characteristics at frequencies above 100 GHz are corrupted similarly to those of the sapphire DRW.

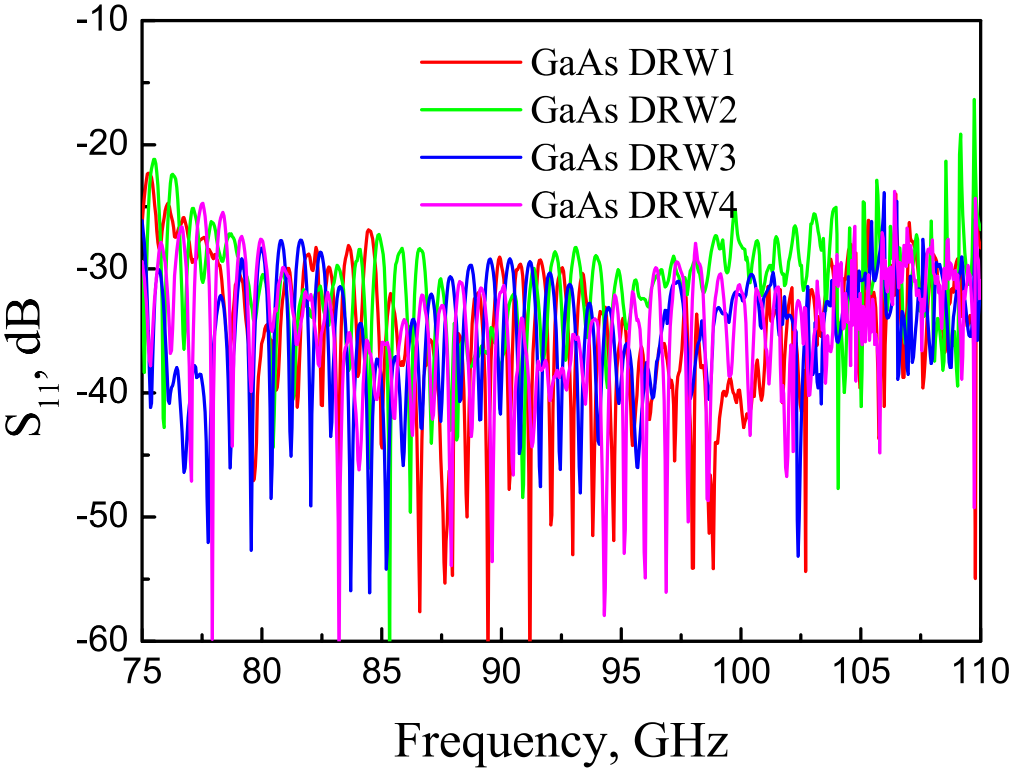

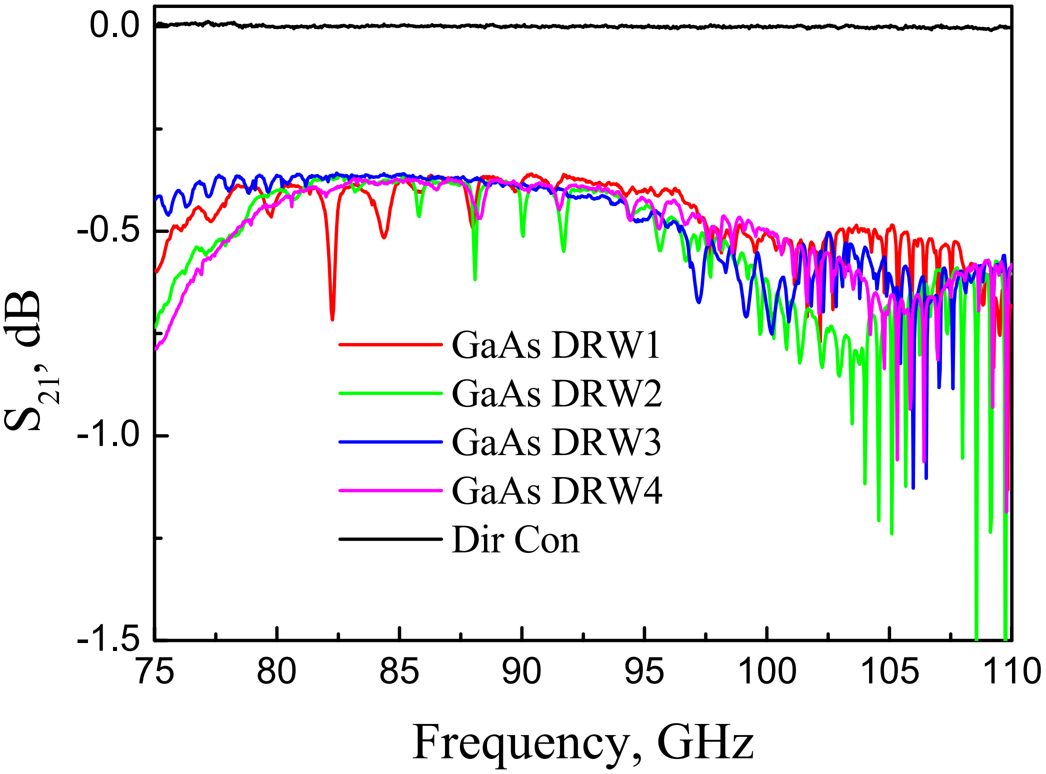

**Figure 6.6.** GaAs DRW measurement results. DirCon means a direct connection between the two metal waveguides.

*x*-displacement of a Sapphire DRW

A nonsymmetrically tapered 110 mm Sapphire DRW was moved along the *x* axis and measured (Fig. 6.7). One can see that the *x*-position is quite uncritical and a 0.5 mm displacement is acceptable (blue and red lines almost coincide). Further movement of the DRW along the *x* axis results in corruption of the transmission characteristics. Furthermore, both $S_{21}$ and $S_{11}$ parameters change more strongly at higher frequencies, while at the lower frequency end they are quite stable (yellow line). This is confirmed by HFSS simulations (Fig. 5.12).

### 6.3. Dielectric waveguide antenna

An interesting effect was found when one end of the DRW was left free [P7]. It caused an increase of the reflection by about 10 dB (Fig. 6.8). That means that while such a structure is still a well matched antenna, the tapering can be better matched with a standard metal waveguide than with the open space.

A sapphire DRW with 47 mm length and 1.0 x 0.5 mm$^2$ cross-section was used as an antenna. Experimental setup is shown in Fig. 6.9. A sapphire waveguide was inserted into a Styrofoam holder that was attached to a standard metal waveguide using the flange pins. Preliminarily some reflection measurements were carried out. The results are shown in Figs. 6.10 and 6.11.

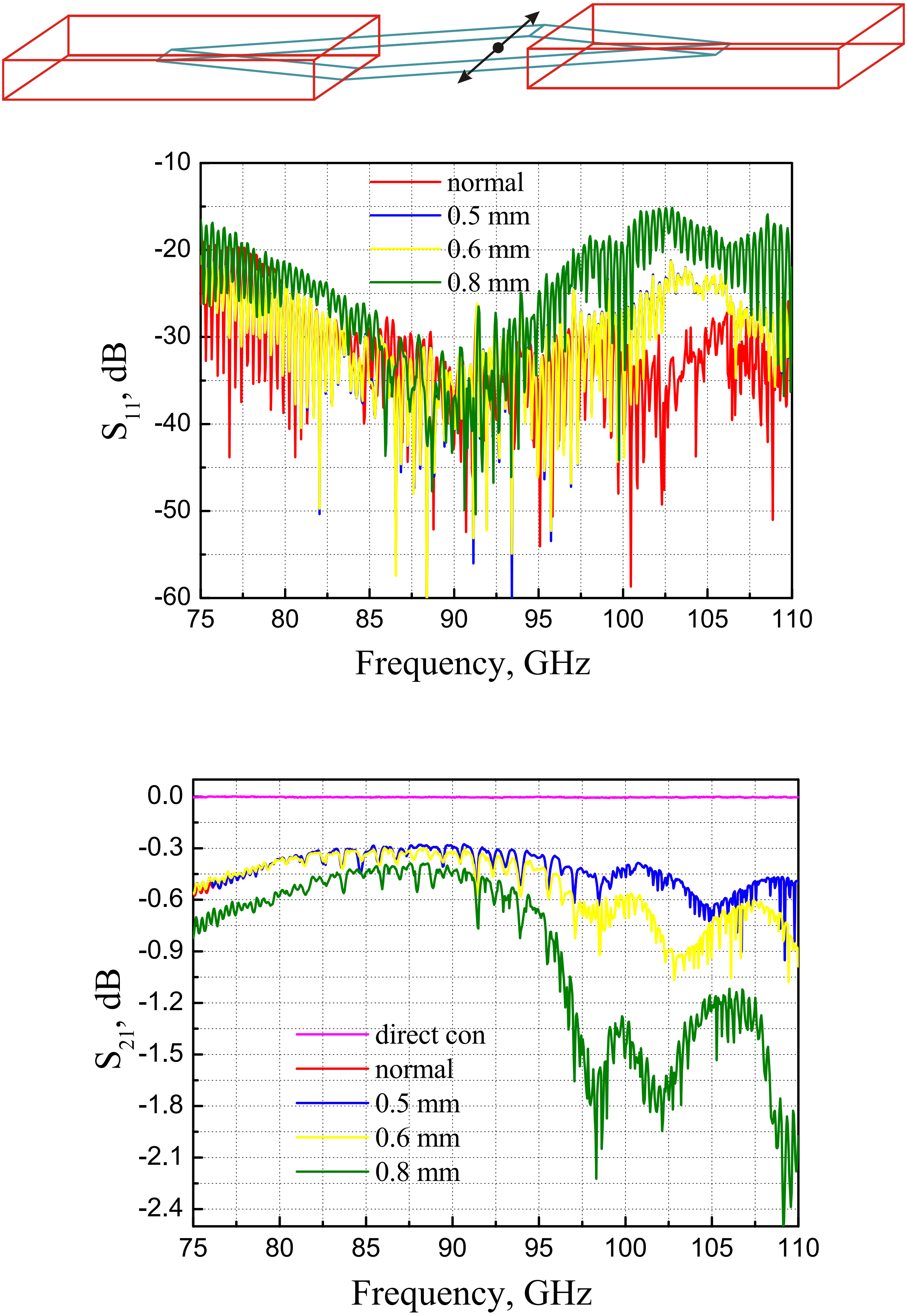

**Figure 6.7.** Measured effects of sapphire DRW displacement.

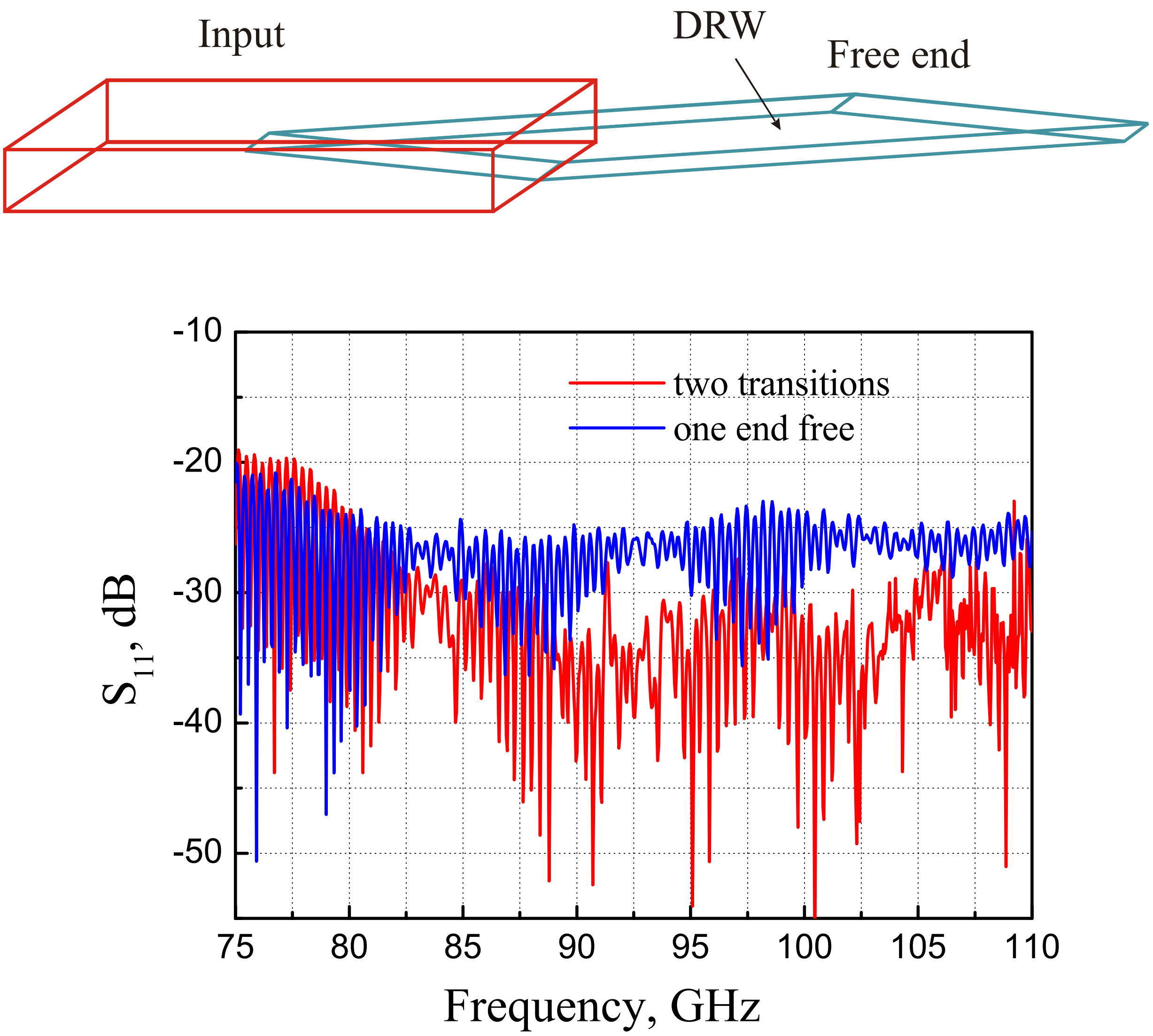

**Figure 6.8.** Measurement results of a DRW with one end free.

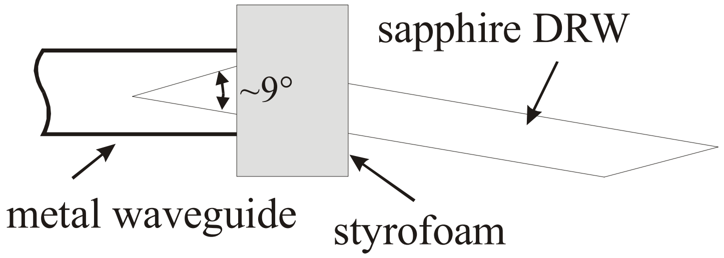

**Figure 6.9.** Schematical structure of a dielectric waveguide antenna.

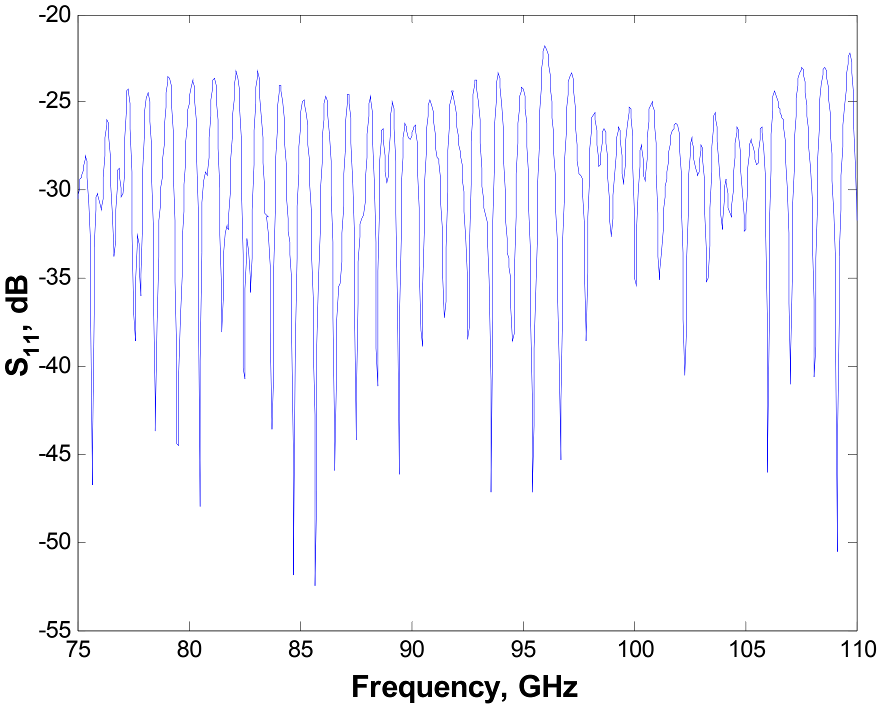

**Figure 6.10.** Reflection vs. frequency of a dielectric waveguide antenna.

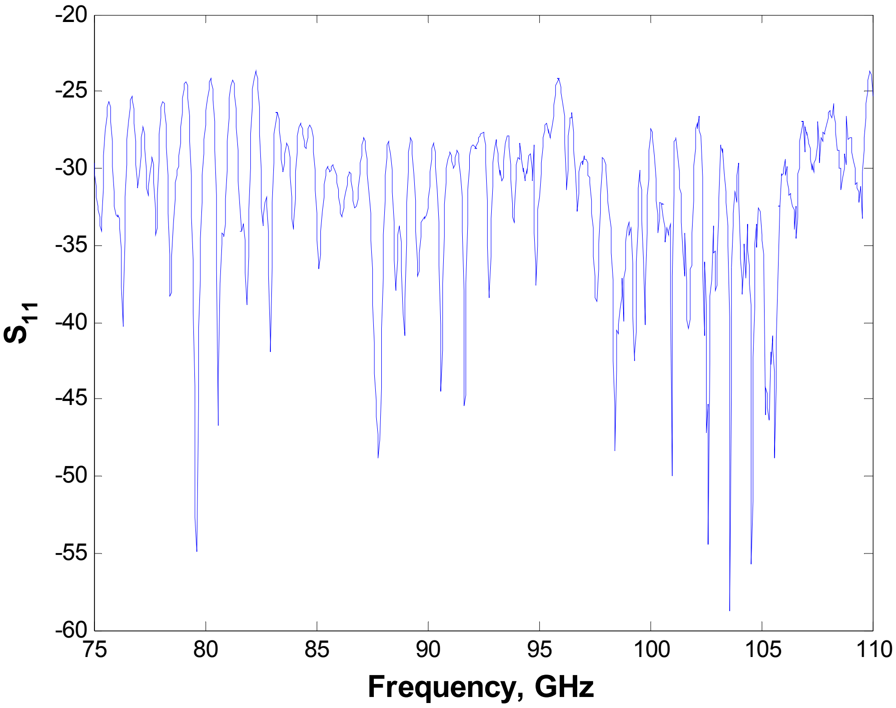

**Figure 6.11.** Reflection vs. frequency of a dielectric waveguide section (both ends are matched).

As one can see the effect of removing the receiving waveguide is weaker compared with the 112 mm DRW case. Perhaps it is because of better quality of the tapering of the 112 mm DRW. Nevertheless, the reflections remain low.

The antenna measurements were carried out with a AB Millimetre 8-350$^{TM}$ Network Analyzer. The radiation pattern in E-plane and H-plane is shown in Fig. 6.12.

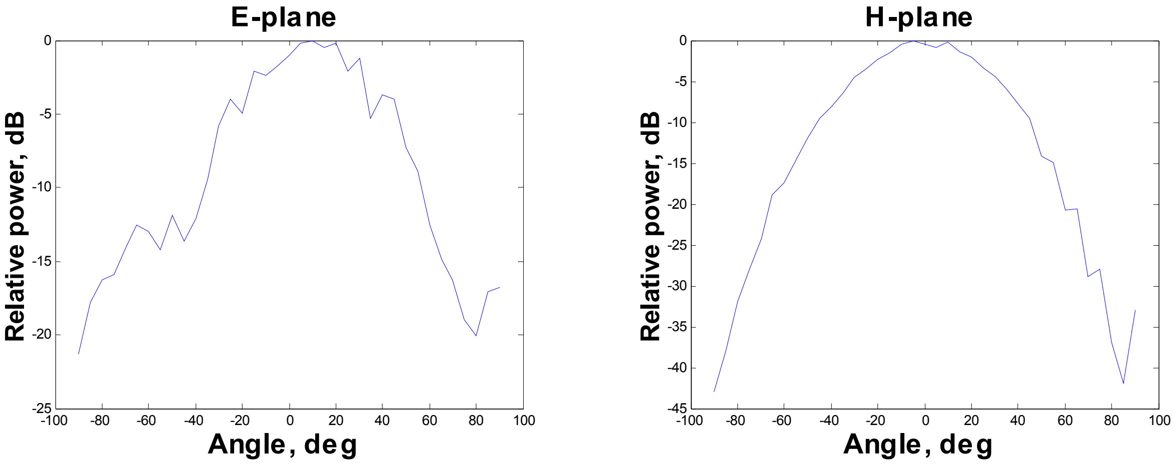

**Figure 6.12.** Radiation pattern of a sapphire waveguide antenna at 95 GHz.

### 6.4. Conclusions

The experimental results indicate that the monocrystalline sapphire and GaAs DRWs can be well matched with a single-mode metal waveguide and have low insertion loss in the 75-110 GHz frequency range. The insertion loss of the sapphire waveguide is very low at frequencies 77-98 GHz.

Excitation of sapphire DRWs with a nonsymmetrical tapering section (nonsymmetrical relative to the optical axis) and excitation of GaAs DRWs with both symmetrical and nonsymmetrical tapering sections were experimentally studied. The taperings were made in the **E**-plane of the metal waveguide. The insertion losses are mainly caused by the transition from metal waveguide to sapphire and vice-versa (radiation) at the lower frequency end and by absorption in the DRW itself in the middle of the frequency range. Thus one can conclude that the materials with relatively high dielectric constant and low loss tangent, like fused sapphire, Si, GaAs etc. may be successfully employed as dielectric waveguides at frequencies above 75 GHz.

## 7. Summary of publications

In [P1] various devices based on rectangular dielectric waveguides were investigated. Such devices as longitudinally magnetized ferrite phase shifter, silicon attenuator and other devices are described. The measurements were carried out using a panoramic analyzer. A panoramic analyzer is a device consisting of the following components: microwave power source (backward wave oscillator) with a metal waveguide output, receiving waveguide with a diode detector, control and indication units. The output frequency of the power source is swept by voltage generated by a control unit and amplitude modulated at 100 kHz. The 100 kHz signal from the diode is then received, amplified, detected and the direct current voltage is displayed on an oscilloscope. Thus one can see the amplitude-frequency characteristics of the device under test on the screen of the oscilloscope. A panoramic analyzer may be also called a scalar network analyzer.

In [P2] a simple and effective structure that allows a good matching between a standard metal waveguide and dielectric waveguide, without any additional element like a horn, etc. A 47 mm sapphire waveguide section was investigated. The ends of that section were tapered nonsymmetrically because of easier fabrication. Simulation data was presented on choosing the plane of tapering of the dielectric waveguide. According to this simulation the dielectric waveguide was tapered in E- plane as it results in lower reflections and excitation loss. As a result a dielectric waveguide section was developed, in which the axes of the dielectric and metal waveguides do not coincide. A low insertion loss (0.05-0.35 dB) and low VSWR (<1.25) were achieved.

In [P3] the authors developed a method of calculating the propagation constant in anisotropic dielectric waveguides with the optical axis coinciding with the axis of the waveguide. This method is based on the well-known Marcatili method, but the equations were derived from the averaging method. A good agreement between simulation and experiment was achieved with a sapphire waveguide section.

In [P4] another method of calculating the propagation constant in anisotropic dielectric waveguides was developed based on the Goell method. Propagation constants of a sapphire waveguide were calculated and measured. The results show better agreement over a wider operating frequency band than those obtained with the previous method.

In [P5] the shape and the dimensions of dielectric waveguide section were optimized using the HFSS simulations. Also, two cases were simulated where the tapering of the dielectric waveguides was not symmetric. It was shown that when the axes of the waveguides coincide, high losses and reflections occur. Therefore, the tip of the tapering should be in the middle of the metal waveguide, even if the axes do not coincide. At last, the influence of displacement of the dielectric waveguide with respect to the metal one was investigated, and it was shown, that the position of it is not very critical except in the $y$-direction.

In [P6] the possibility of matching of a dielectric rod waveguide and a metal waveguide was demonstrated when the relative permittivity of the dielectric is high (about 10). Simulation of a silicon waveguide was shown as a dramatic example. The measurement results of available sapphire waveguides are also shown.

In [P7] the output metal waveguide was removed from the dielectric waveguide section to obtain a sapphire rod waveguide antenna. Reflections and radiation patterns are presented here. A comparison of reflections was made when both ends of the dielectric waveguide were matched or one end was free. It was shown that in the latter case the reflections slightly grow up.

# 8. Summary and conclusion

Simple numerical and approximate methods for calculations of the propagation constant and propagation loss of an anisotropic dielectric waveguide were developed and successfully employed for a sapphire DRW. These methods are based on the methods by Marcatili and Goell originally developed for isotropic dielectric waveguides. Good agreement with experimental measurements was achieved.

In this work three types of DRW tapering sections were studied for electromagnetic wave excitation in the DRW at 75-110 GHz: symmetrical, pyramidal and nonsymmetrical tapering. The rectangular cross section for the frequency range of 75-110 GHz was chosen according to empirical evaluations: $k_0 b = 1.7 - 1.9$, $a/b = 0.5$.

Finite Element Method (FEM) simulations with Agilent HFSS$^{\text{TM}}$ software were carried out in order to investigate the preferable shape and orientation of the tapering sections, optimal cross-sections and positions of the mode launcher. Tapering in the *E*-plane was found to be preferable. HFSS simulations show that there is no significant difference between pyramidal, symmetrical and nonsymmetrical types of tapering, but technically symmetrical and nonsymmetrical type of tapering are easier to manufacture than the pyramidal type, especially if the DRW is made of a fragile material.

Different cross-sections and tapering lengths (1-8 mm) of DRWs were simulated with HFSS as well. The cross sections of $1.0 \times 0.5$ mm$^2$, $1.05 \times 0.525$ mm$^2$ and $1.1 \times 0.55$ mm$^2$ result in suitable $S_{21}$ and $S_{11}$ characteristics. The tapering length less than 2 mm has relatively high reflection and bigger transition losses but tapering of 2 mm is already acceptable. It even gives better transmission coefficient at lower frequencies with the maximum approximately at 88 GHz. Increasing the tapering length only slightly improves the transmission at higher frequencies and with large lengths this improvement is very small. Moreover, at 8 mm an undesirable dip appears. Technically long tapering section is more difficult to realize if the material is fragile.

Two ways of nonsymmetrical excitation were studied: i) when the axes of the DRW and metal waveguide coincide, and ii) when there is an angle (e.g. 4.5° in case of a 9° tapering angle) between them. It turns out that when the DRW axis orientation differs by 4.5° from the *z* axis of the metal waveguide, the transmission coefficient is higher than in the case when the DRW and the metal waveguide axes coincide, because then the mode launcher (edge of the tapering) is too close to the metal wall and results in a nonsymmetrical field distribution that is more difficult to convert to the symmetrical open DRW mode.

Also the effect of the position of the tapered end of DRW in the transition from a metal waveguide to DRW in the symmetrical case was simulated. It was found that DRW is not very sensitive to the *x*, *y*, and *z* positions, but the best results are achieved when the axes of the DRW and the metal waveguide coincide. Most critical is the *y* direction.

S-parameter characteristics of a sapphire DRW with a 6 mm nonsymmetrical tapering and with a cross-section of $1.0 \times 0.5$ mm$^2$ and a GaAs DRW with symmetrical 6 mm and 8 mm taperings and with cross-sections of $1.0 \times 0.5$ mm$^2$ and $1.5 \times 0.5$ mm$^2$ were measured with Hewlett Packard Vector Network Analyzer HP 8510$^{\mathrm{TM}}$.

Transitions from a standard WR-10 metal waveguide to a dielectric waveguide were investigated. A simple and effective structure without a horn structure and/or additional components was designed. Experimental results show good transmission characteristics of the dielectric waveguide section made of monocrystalline sapphire waveguide.

Looking at Figs. 6.2 and 6.3 one can see that additional 60 mm (approximately) of the dielectric waveguide adds extra loss from 0.05 dB at 75 GHz to 0.15 dB at 98 GHz to the total insertion loss. That means that the propagation loss in the sapphire DRW section varies approximately from 1 dB/m at 75 GHz to 3 dB/m at 98 GHz. The theoretical propagation loss in a standard WR-10 copper metal waveguides varies from 3.4 dB/m at 75 GHz to 2.4 dB/m at 110 GHz.

# References

1. V.V. Meriakri, B.A. Murmuzhev, M.P. Parkhomenko, "Millimeter wave devices based on dielectric, ferrite and semiconductor waveguides", *Proc. of the Microwave and Optoelectronics Conference*, 1997, vol. 2, pp. 431-433.
2. V.E.Lioubchenko, G.S.Makeeva, E.I.Nefedov, "Active devices for microwave frequency region with distributed parameters (review*)", Radiotehnika i Elektronika*, September 1982, pp. 1665-1682 (in russian),

   (В.Е. Любченко, Г.С. Макеева, Е.И. Нефедов, "Активные устройства СВЧ-диапазона с распределенными параметрами (обзор)", *Радиотехника и Электроника*, Сентябрь 1982, с. 1665-1682).
3. R. Merendez, R. Mittra, P. Yang, N. Deo, "Effective graded-index guides for millimetre-wave applications", *Microwaves, Optics and Acoustics*, vol. 3, no. 2, March 1979, pp. 51-55.
4. J.A. Paul, Y.W. Chang, "Millimeter-wave image-guide integrated passive devices", *IEEE Transactions on Microwave Theory and Techniques*, vol. MTT-26, no. 10, 1978, pp.751-754.
5. Private talk with V.V. Meriakri.
6. V.V. Meriakri, M.P. Parkhomenko, "Millimeter wave phase shifters based on ferrite dielectric waveguides ", *Proc. of the 12th International Conference on Microwaves and Radar*, 1998, vol. 2, 1998, pp. 514 -517.
7. A.M. Goncharenko, L.N. Deryugin, A.M. Prokhorov, G.P. Shipulo, "Development of integrated optics in the USSR", *Journal of Applied Spectroscopy*, vol. 29, no. 6, December 1978, pp. 987-997.
8. H. Nishihara, "Recent advancement on optical integrated circuits", *Proc. of the IEEE Region Conference on Computer and Communication Systems*, Hong Kong, vol. 1, September 1990, pp. 99-103.
9. W.W. Schlösser, "Der rechttätige dielektrische Draht", *Archiv für Electronik und Übertragungstechnik,* vol. 18, no. 7, 1964, pp. 403-410.
10. J.E. Goell, "A circular-harmonic computer analysis of rectangular dielectric waveguides", *Bell System Technical Journal*, vol. 48, no. 7, September 1969, pp. 2133-2160.
11. В.Ф. Взятышев, *Диэлектрические волноводы*, издательство «Советское радио», 1970.
12. T.N. Trinch, R. Mittra, "Transitions from metal to dielectric waveguide", *Microwave Journal*, November 1980, pp. 71-74.
13. H. Jacobs, M. Chrepta, "Electronic phase shifter for millimeter- wave semiconductor dielectric integrated circuits", *IEEE Transactions on Microwave Theory and Techniques*, vol. MTT-22, no. 4, April 1974.

14. V.V. Meriakri, M.P. Parkhomenko, “Millimeter-wave dielectric strip waveguides made of ferrites and phase shifters based on these waveguides”, *Electromagnetic Waves & Electronic Systems*, vol. 1, no. 1, 1996, pp. 89-96.
15. M.N. Afsar, K.J. Button, "Millimeter-wave dielectric measurement of materials", *Proceedings of the IEEE*, vol.73, no. 1, January 1985, pp. 131-153.
16. M.N. Afsar, H. Chi, X. Li, "Millimeter wave complex refractive index, complex dielectric permittivity and loss tangent of high purity and compensated silicon", *Conference on Precision Electromagnetic Measurements*, 1990, CPEM '90Digest, pp. 238-239.
17. J. Molla, R. Vila, R. Heidinger, A. Ibarra, "Radiation effects on dielectric losses of Au-doped silicon", *Journal of Nuclear Materials*, vol. 258-263, 1998, pp.1884-1888.
18. S.M. Sze, *Physics of Semiconductor Devices*, Wiley, New York, 1981.
19. B. Komiyama, M. Kiyokawa, T.Matsui, "Open resonator for precision measurements in the 100 GHz band", *IEEE Transactions on Microwave Theory and Techniques*, vol. 39, no. 10, October 1991, pp. 1792-1796.
20. P. Wright, L.E. Davis, "The complex permittivity of aluminum nitride substrates", *IEEE MTT-S International Microwave Symposium Digest*, 1993, vol. 1, pp. 269 –272.
21. Y. Kurihara, T. Endoh, K. Yamada, "The influence of moisture on surface properties and insulation characteristics of AlN substrates", *IEEE Transactions on Components, Hybrids, and Manufacturing Technology*, vol. 12, no. 3, September 1989, pp. 330-334.
22. R.C. Weast, editor, *Handbook of Chemistry and Physics*, CRC Press, 57th edition, 1976-1977.
23. R.F. Davis, "III-V nitrides for electronic and optoelectronic applications", *Proceedings of the IEEE*, vol. 79, no. 5, 1991, pp. 702-712.
24. J.E. Jaffe, "Ab initio prediction of GaN $(10\bar{1}0)$ and $(110)$ anomalous surface relaxation", *Physical Review B*, vol. 53, no. 8, 15 February 1996-II, pp. R4209-R4212.
25. M.N. Yoder, "Gallium nitride past, present, and future", *Proc. of the Conference on Advanced Concepts in High Speed Semiconductor Devices and Circuits*, IEEE/Cornell, 1997, pp. 3-12.
26. V.V. Parshin, “Dielectric materials for gyrotron output windows”, *International Journal of Infrared and Millimeter Waves*, vol. 15, no. 2, 1994, pp. 339-348.
27. A.F. Krupnov, V.N. Markov, G.Y. Golubyatnikov, I.I. Leonov, Y.N. Konoplev, V.V. Parshin, “Ultra-low absorption measurement in dielectrics in millimeter- and submillimeter- wave range”, *IEEE Transactions on Microwave Theory and Techniques*, vol. 47, no. 3, March 1999, pp. 284-289.
28. А.П. Бабичев, Н.А. Бабушкин, А.М. Братковский и др., *Физические величины*, справочник, Энергоатомиздат, под редакцией Григорьева, Е.З. Мейликова, Москва, 1991.

29. A. Sudbø, "Why are the accurate computations of mode fields in rectangular dielectric waveguides difficult?", *Journal of Lightwave Technology*, vol. 10, no. 4, April 1992, pp. 418-419.
30. J. Bach Andersen, V.V. Solodukhov, "Field behavior near a dielectric wedge", *IEEE Transactions on Antennas and Propagation*, vol. AP-26, no. 4, 1978, pp. 598-602.
31. T. Itoh, *Numerical Techniques for Microwave and Millimeter-Wave Passive Structures*, New York, Wiley, 1989.
32. E. Schweig, W. Bridges, "Computer analysis of dielectric waveguides: a finite-difference method", *IEEE Transactions on Microwave Theory and Techniques*, vol. MTT-32, no. 5, May 1984, pp. 531-541.
33. S. Garcia, T. Hung-Bao, R. Martin, B. Olmedo, "On the application of finite methods in time domain to anisotropic dielectric waveguides", *IEEE Transactions on Microwave Theory and Techniques*, vol. 44, no. 12, December 1996, pp. 2195-2206.
34. B.M.A. Rahman, J.B. Davies, "Finite-element analysis of optical and microwave waveguide problems", *IEEE Transactions on Microwave Theory and Techniques*, vol. MTT-32, no. 1, January 1984, pp. 20-28.
35. P. Silvester, "A general high-order finite-element waveguide analysis program", *IEEE Transactions on Microwave Theory and Techniques*, vol. MTT-17, no. 4, April 1969, pp. 204-210.
36. B.M. Dillon, J.P. Webb, "A comparison of formulations for the vector finite element analysis of waveguides", *IEEE Transactions on Microwave Theory and Techniques*, vol. 42, no. 2, February 1994, pp. 308-316.
37. T. Rozzi, M. Mongiardo, *Open Electromagnetic Waveguides*, The Institution of Electrical Engineers, London, 1997.
38. R. Mittra, Y. Hou, V. Jamnejad, "Analysis of open dielectric waveguides using mode-matching technique and variational methods", *IEEE Transactions on Microwave Theory and Techniques*, vol. MTT-28, no. 1, January 1980, pp. 36-43.
39. R. Pregla, "A method for the analysis of coupled rectangular dielectric waveguides", *Archiv für Elektronik und Übertragungstechnik (Electronics and Communication)*, Band 28, Heft 9, September 1974, pp. 349-357.
40. S.R. Cvetkovic, J.B. Davies, "Self-adjoint vector variational formulation for lossy anisotropic dielectric waveguide", *IEEE Transactions on Microwave Theory and Techniques*, vol. MTT-34, no. 1, January 1986, pp. 129-134.
41. R.B. Wu, "On the variational reaction theory for dielectric waveguides", *IEEE Transactions on Microwave Theory and Techniques*, vol. MTT-33, no. 6, June 1985, pp. 477-483

42. C.C. Su, “Analysis of unbounded dielectric waveguides using the surface integral equations method”, *IEE Proceedings, part J: Optoelectronics*, vol. 136, no. 3, June 1989, pp. 166-168.
43. C.C. Su, “A surface integral equations method for homogeneous optical fibers and coupled image lines of arbitrary cross sections”, *IEEE Transactions on Microwave Theory and Techniques*, vol. MTT-33, no. 11, November 1985, pp. 129-134.
44. Е.Ф. Алексеенко, Ю.К. Барсуков, «Анализ поля диэлектрического волновода при различной форме сечения стержня», *Радиотехника и Электроника*, том 15, № 12, 1980, с. 2531-2541.

    Translation in E.F. Alekseenko, Yu.K. Barsukov, ”Dielectric waveguide field analysis with various cross section”, *Radio Engineering and Electronic Physics*, vol. 25, no. 12, December 1980, pp. 41-49.
45. K. Solbach, I. Wolff, “The electromagnetic fields and the phase constants of dielectric image lines”, *IEEE Transactions on Microwave Theory and Techniques*, vol. MTT-26, no. 4, April 1978, pp. 266-274.
46. W. Schlösser, H.G. Unger, “Partially filled waveguides and surface waveguides of rectangular cross section”, *in Advances in Microwaves*, edited by Leo Young, vol. 1, Academic Press, 1966, pp. 319-387.
47. H. Diestel, “A method of calculating the guided modes of strip-loaded optical waveguides with arbitrary index profile”, *IEEE Journal of Quantum Electronics*, vol. QE-20, November 1984, pp. 1288-1293.
48. P. Berini, K. Wu, ”Modelling lossy anisotropic dielectric waveguides with the method of lines”, *IEEE Transactions on Microwave Theory and Techniques*, vol. 44, no. 5, May 1996, pp. 749-759.
49. M.P. Mrozowski, “IEEM FFT- a fast and efficient tool for rigorous computations of propagation constants and field distributions in dielectric guides with arbitrary cross section and permittivity profiles”, *IEEE Transactions on Microwave Theory and Techniques*, vol. 39, no. 2, February 1991, pp. 323-329.
50. T.F. Jablonski, M.J. Sovinski, “Analysis of dielectric guiding structures by the iterative eigenfunction expansion method”, *IEEE Transactions on Microwave Theory and Techniques*, vol. 37, no. 1, January 1989, pp. 63-70.
51. C.H. Henry, B.H. Verbeek, “Solution of the scalar wave equation for arbitrary shaped dielectric waveguides by two-dimensional Fourier analysis”, *Journal of Lightwave Technology*, vol. 7, no. 2, February 1989, pp. 308-313.

52. M.A. Forastiere, G.C. Righini, “Scalar analysis of general dielectric waveguides by Fourier decomposition method and Lanczos reduction”, *Journal of Lightwave Technology*, vol. 17, no. 2, February 1999, pp. 362-368.
53. S.J. Hewlett, F. Ladouceur, “Fourier decomposition method applied to mapped infinite domains: scalar analysis of dielectric waveguides down to modal cutoff”, *Journal of Lightwave Technology*, vol. 13, no. 3, March 1995, pp. 375-383.
54. Г.И. Веселов, Г.Г. Воронина, «К рассчету открытого диэлектрического волновода прямоугольного сечения», *Радиофизика*, т. XIV, № 12, 1971, с. 1891-1901.
55. T. Itoh, “Dielectric waveguide-type millimeter-wave integrated circuits”, in *Infrared and Millimeter Waves*, edited by K. Button and J. Wiltse, 1981, Academic Press, vol. 4, chapter 5, pp. 199-273.
56. E.A.J. Marcatili, “Dielectric rectangular waveguide and directional coupler for integrated optics”, *Bell System Technical Journal,* vol. 48, no. 7, 1969, pp. 2071-2102.
57. R.M. Knox, P.P. Toulios, “Integrated circuits for the millimeter through optical frequency range,” *Proceedings of Symposium on Submillimeter Waves,* 1970, Polytechnic Institute of Brooklyn, New York, pp. 497-516.
58. V.J. Menon, S. Bhattacharjee. K.K. Dey, “The rectangular dielectric waveguide revisited”, *Optics Communications*, vol. 85, no. 5,6, 1 October 1991, pp. 393-396.
59. E.A.J. Marcatili, A.A. Hardy, “The azimuthal effective-index method”, *IEEE Journal of Quantum Electronics*, vol. 24, no. 5, May 1988, pp. 766-774.
60. M.I. Oksanen, S.A. Tretyakov, I.V. Lindell, “Vector circuit theory for isotropic and chiral slabs”, *Journal of Electromagnetic Waves Applications*, vol. 4, 1990, pp. 613-643.
61. Y. Kobayashi, T. Tomohiro, “Resonant modes in shielded uniaxial-anisotropic dielectric rod resonators”, *IEEE Transactions on Microwave Theory and Techniques*, vol. 41, Dec. 1993, pp. 2198-2205.